Università degli Studi di Torino
Doctoral School of Sciences and Innovative Technologies
PhD Program in Chemical and Material Sciences XXIX Cycle

In situ and operando characterization of zeolite-based catalysts by means of Raman spectroscopy

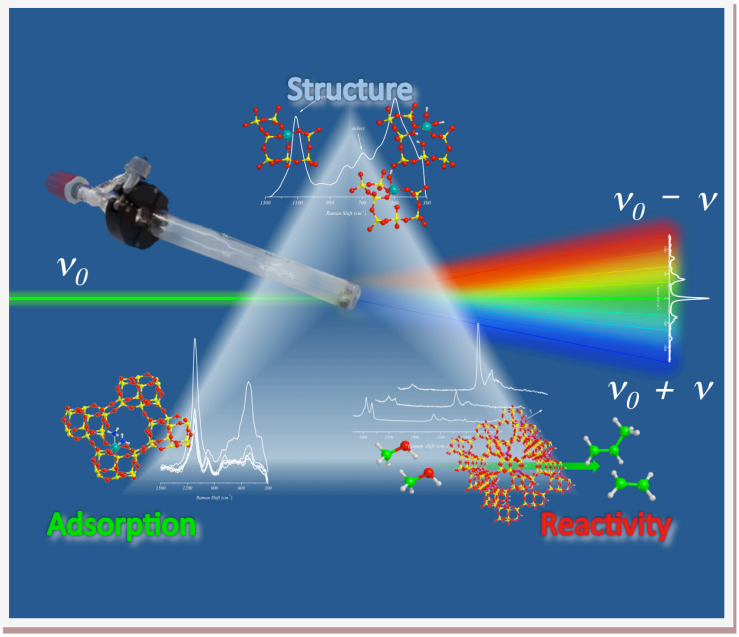

Matteo Signorile

Supervisor:
Dr. Francesca Carla Bonino

Università degli Studi di Torino

Doctoral School of Sciences and Innovative Technologies

PhD Program in Chemical and Material Sciences XXIX cycle

In situ and *operando* characterization of zeolite-based catalysts by means of Raman spectroscopy

Candidate: **Matteo Signorile**

Supervisor: Dr. **Francesca Carla Bonino**

Jury Members:

Dr. **Davide Ferri**
Paul Scherrer Institute
Catalysis for Energy group

Dr. **Andrea Piovano**
Institut Laue-Langevin

Prof. **Bartolomeo Civalleri**
University of Torino
Department of Chemistry

Head of the Doctoral School: Prof. Guido Boffetta
PhD Program Coordinator: Prof. Mario Chiesa

Torino, 2017

Ai miei nonni, che mi hanno introdotto
al meraviglioso mondo della scienza e della tecnica

A Coco

Acknowledgments

Many people have been involved in the development of this thesis work, everyone deserving my best acknowledgments. In particular, I would like to express my unconditional gratitude to Francesca and Alessandro, who helped me to grow up as researcher day by day along my whole PhD project. A sincere thanks also to Silvia, for her precious support and suggestions.

Concerning the MTH topic, my best acknowledgments are due to Enrico Cepparrone (BSc thesis student), Nicolas Loock (MSc thesis student) and Daniel Rojo Gama (PhD student from University of Oslo), for their help with a relevant fraction of the experimental work. I also would like to mention the nice collaboration established with the Catalysis research group of University of Oslo (prof. K.P. Lillerud, prof. U. Olsbye and prof. S. Svelle) and Topsøe A/S (dr. P. Beato), within the framework of the ZeoMorph project.

With regard to the TS-1 topic, I acknowledge my colleague V. Crocellà for sharing the research project involving Evonik Industries AG and our industrial partners dr. F. Schmidt and dr. H. Morell.

Finally, I would mention the collaboration with the Theoretical Chemistry Group of Università di Torino for the helpful discussion and technical support, as well as the NOTUR consortium for granting the HPC research project NN9381K.

Table of Contents

Preface

The main goal of this doctoral project has been the application of Raman spectroscopy to the characterization of zeolites, with particular regard to their behavior in controlled atmosphere and/or under reaction conditions. Even if apparently this may be considered a trivial task (as for many other spectroscopic techniques), the Raman approach to zeolites is rather complex because of the several drawbacks affecting it (*e.g.* fluorescence and laser induced sample damaging).

A key point of this thesis has been to exploit/develop a set of tools able to overcome such limitations: several implementations have been reported in the literature with the same aim, however each one demonstrated some incompatibilities with the purposes of the present work. For such reason, a totally new experimental setup was designed, developed and tested.

Following the good preliminary results achieved, the novel device was then applied to the study of two relevant processes in the zeolite/catalysis field: the Methanol To Hydrocarbon (MTH, based on acid zeolites) and the Hydrogen Peroxide to Propylene Oxide (HPPO, catalyzed by Titanium Silicalite-1, TS-1). The former represented an optimal benchmark for the new setup, since the reaction involves labile organic reactants and products, thus threatened by the photon induced damaging. The latter, instead, thanks to the peculiar features of the TS-1, can be regarded as a more fundamental research work, also involving a multiple technique approach and quantum mechanical simulation (the latter representing a significant fraction of this thesis work).

Chapter 1

Introduction

1.1 The samples: zeolites

Zeolites are a rich class of materials, both from natural and synthetic origin. According to the International Union of Pure and Applied Chemistry (IUPAC), «*Zeolites and zeolite-like materials comprise a broad range of porous crystalline solids. The structures of zeolite-type materials are based essentially on tetrahedral networks which encompass channels and cavities*».[1] The number of known zeolite structures (*i.e.* frameworks) is continuously growing up: being 176 framework types reported in 2007,[2] other 55 new structures have been validated since nowadays, *i.e.* reaching 231 different ones.[3] Considering all the possible compositional variations (the tetrahedra commonly host Si or Al, but other "heteroatoms" such as B, P, Ge, Ga, As and transition metals can be included as well), it is simple to understand that the label "zeolite" describes thousands of different materials, each one with its specific properties. Another source of variability is represented by the extraframework counterions, which are eventually hosted in the porous system in order to balance the electrical charge of the framework. Furthermore, zeolites effectively behave as adsorbent materials, being able to host a large amount of atoms/molecules (in the most common case water) in the empty spaces of channels and cavities: these species can be usually eliminated under proper conditions (*e.g.* through a thermal treatment). Exactly observing the development of steam upon the rapid heating of a Stilbite mineral, the Swedish mineralogist Axel Fredrik Cronstedt coined in the 18th century the term zeolite from the combination of the Greek words ζεο (*zeo*, "to boil") and

λιθος (*lithos*, "stone").[4] The depletion of counterions is instead impossible, because of their role in keeping the material charge nil.

Coming back to the composition, the tetrahedral units are in the simplest case represented by orthosilicate anions (SiO_4^{4-}) connected through the corners (*i.e.* giving rise to a tectosilicate): the resulting structure, terminated on external surfaces by silanol groups, does not require an extraframework charge balance since it is neutral by itself. The existence of natural all-silica zeolites has not been reported, being all of synthetic origin.[5–8] Conversely the substitution of the SiO_4^{4-} by AlO_4^{5-} is very likely also in natural samples, such as zeolites are often (and sometimes improperly) classified as aluminosilicates.[1] Due to the excess of negative charge of the framework accomplishing such substitution, the presence of extraframework cations is now compulsory in order to keep the overall charge neutrality. These are extremely important in determining the zeolite chemical behavior, since they represent the active sites of the material: as an example, since counterions can be easily substituted by other ones, zeolites are widely exploited as ion exchange materials.[9–11] Another application with great relevance nowadays, involving zeolties with alkali and alkali-earth counterions, is the CO_2 capture and separation from other gases: carbon dioxide can interact with the cations as well as the framework oxygen atoms, thereby providing a set of preferential adsorption sites.[12–15] It is also possible to perform transition metal ions exchanges, thus inducing redox properties to the material: giving some examples, Cu- and Fe-zeolites are applied as catalysts for the Selective Catalytic Reduction (SCR) of NO_x in post-combustion exhausts,[16–18] whereas Ni-zeolites are active toward the olefins oligomerization reaction.[19,20] Probably the type of counterion which found the largest industrial application is the proton: the H^+ shows a strong Brønsted acidity, comparable to mineral acids one,[21] with the enormous advantage to handle a solid rather than a liquid. Furthermore, thanks to their microporous structure, zeolites ensure high

selectivity: only the molecules able to diffuse through the channel system can reach the active sites (and thus react) and only the products (as well as the reaction transition states) which are allowed by the framework steric constrains can be formed.[22,23] The marked acid character and the intrinsic selectivity of zeolites brought them to dominate the catalysis market in petroleum refining and petrolchemistry.[24,25] Another possible way to balance the charge, other than counterions, is available: if phosphates PO_4^{3-} are replacing the SiO_4^{4-}, each one is able to counterbalance a AlO_4^{5-} (*i.e.* without the needing of an extraframework cation). This synthetic opportunity brought to produce materials with various Si:Al:P compositions, giving rise to the so called SAPO and ALPO zeotypes families.[26,27]

The substitutions of Si by heterovalent atoms are not the only allowed by the zeolites chemistry. An example is the isovalent substitution of silicon by germanium, possible in a wide range of compositions and sometime giving rise to new structures, unreported for siliceous-only zeolites.[28–32] Probably, the most relevant case of isovalent substitution (also regarding the industrial application) is represented by the insertion of Ti: being obtained for the first time in 1983 by the researcher from ENIChem SPA on Silicalite-1 (*i.e.* obtaining the famous TS-1),[33] it has been successfully to many other framework topologies.[34–37] TS-1 represented for academia an exceptional laboratory, where several characterization techniques could be exploited and developed: a brief description of these successes will be given in Chapter 4. However the interest toward TS-1 was not relegated to the fundamental research only, as a number of industrial processes exploiting it as catalysts were rapidly developed few years after its discovery.[38,39] The main application field of TS-1 is represented by partial oxidation reaction: its catalytic role is to activate the oxidizing medium (*i.e.* hydrogen peroxide in aqueous solution) by forming Ti-peroxo species,[40–42] thus making it capable to oxidize the desired organic substrates in a controlled way. Among all the possible reactions, the

most relevant ones are the epoxidation of olefins (and in particular of propene to propylene oxide)[43] and the ammoxidation of cyclohexanone to cyclohexanone oxime (a precursor for nylon 6 production).[44] With respect to the previous industrial processes the TS-1 based ones represented a big step forward, being safer and showing higher selectivities toward the desired products.[39]

Even if not exhaustively, the previous paragraphs aimed to introduce the world of zeolites, underlining its variety and complexity, as well as the importance of these materials in several industrial processes (but also in the everyday life). Since the spreading of structures, properties, types of active sites and applications typical of zeolites, their complete characterization requires a multitechnique approach. Each specific measurement can in fact put in evidence a different facet of their complex nature: giving few examples, diffraction techniques allow to obtain the structure of these materials, volumetry is helpful in the porosity characterization, microscopies in the assessment of morphology, *etc*.[45] A peculiar class of techniques is represented by spectroscopies: the variety of the information accessible is in fact really wide, ranging from structural to electronic properties, passing through active sites features and reactivity.[46–49] Among them, a rather peculiar case is represented by Raman spectroscopy: beside its potentialities and advantages toward zeolites characterization, its application has been limited by several drawbacks. A detailed picture of the Raman characterization of zeolites will be given in the following. However, before entering this specific topic, in the next section the fundamentals of Raman spectroscopy (useful for the clear understanding of the related issues) are introduced.

1.2 The approach: Raman spectroscopy

Raman spectroscopy is a vibrational technique originating from the inelastic scattering of electromagnetic radiation. Its name derives from the one of discoverer, Sir Chandrasekhara Venkata Raman, that reported together with is coworker Krishnan as «*[…] in every case in which light is scattered by the molecules in dust-free liquids or gases, the diffuse radiation of the ordinary kind, having the same wave-length as the incident beam, is accompanied by a modified scattered radiation of degraded frequency*».[50] Even if Raman was the first scientist to experimentally observe the phenomenon, the inelastic diffusion of light was theoretically predicted by Smekal five years before.[51] Few months after Raman's report, an independent experimental confirmation came from Landsberg and Mandelstam, who verified the same effect on solid samples.[52] Following its discovery, Sir Raman was awarded in 1930 with the Nobel Prize for Physics «*for his work on the scattering of light and for the discovery of the effect named after him*».

As briefly introduced, the inelastic scattering of an electromagnetic radiation is the physical phenomenon determining the occurrence of the Raman effect: the general definition of scattering states that a scattering process occurs when a wave (or a particle) is randomly deflected by its original trajectory consequently to the interaction with another wave/particle (defined as scatterer or scattering center). Such definition is very broad and, still, the intimate mechanism of the phenomenon has not been clarified. In the following, the key steps of the theory of Raman scattering will be delineated, being these adapted from parent literature.[53,54] Three types of scattering phenomena are observed in a Raman experiment: when a photon of energy $\hbar\omega_i$ (being ω_i its angular frequency and $\hbar$ the reduced Plank constant) interacts with a given system sitting in an energy level E_i, the photon is annihilated and the system is promoted to a virtual excited state. The system readily decays from this virtual state to a final state E_f and a new photon of

energy $\hbar\omega_f$ is created. The energy of this photons determines the type of scattering occurring: i) if $\hbar\omega_f = \hbar\omega_i$ (thus $E_f = E_i$) the photon belongs an elastic scattering; ii) if $\hbar\omega_f < \hbar\omega_i$ (thus $E_f > E_i$) the scattering is inelastic and it causes the production of a lower frequency photon; iii) if $\hbar\omega_f > \hbar\omega_i$ (thus $E_f < E_i$) the scattering is still inelastic but the photon is now re-emitted with higher frequency. The difference in energy $E_f - E_i$ observed between the two energy level can be rewritten as reported in Equation 1.1 by exploiting the Plank's law.

$$\left|E_f - E_i\right| = \hbar\omega_m \tag{1.1}$$

Taking into account the conservation of energy for the overall scattering process (Equation 1.2)

$$\left|E_f - E_i\right| = \left|\hbar\omega_f - \hbar\omega_i\right| \tag{1.2}$$

and combining Equation 1.2 with Equation 1.1, Equations 1.3, 1.4 and 1.5 are thus obtained.

$$\left|\hbar\omega_f - \hbar\omega_i\right| = \hbar\omega_m \tag{1.3}$$

$$\begin{cases}\omega_f - \omega_i = 0 \\ \omega_m = 0\end{cases} \cup \begin{cases}\omega_f - \omega_i < 0 \\ \omega_f - \omega_i = -\omega_m\end{cases} \cup \begin{cases}\omega_f - \omega_i > 0 \\ \omega_f - \omega_i = \omega_m\end{cases} \tag{1.4}$$

$$\begin{cases}\omega_f = \omega_i \\ \omega_m = 0\end{cases} \cup \begin{cases}\omega_f < \omega_i \\ \omega_f = \omega_i - \omega_m\end{cases} \cup \begin{cases}\omega_f > \omega_i \\ \omega_f = \omega_i + \omega_m\end{cases} \tag{1.5}$$

Equation 1.5 describes (from left to right) the Rayleigh, Stokes and anti-Stokes scattering processes. This result can be schematized as in Figure 1.1.

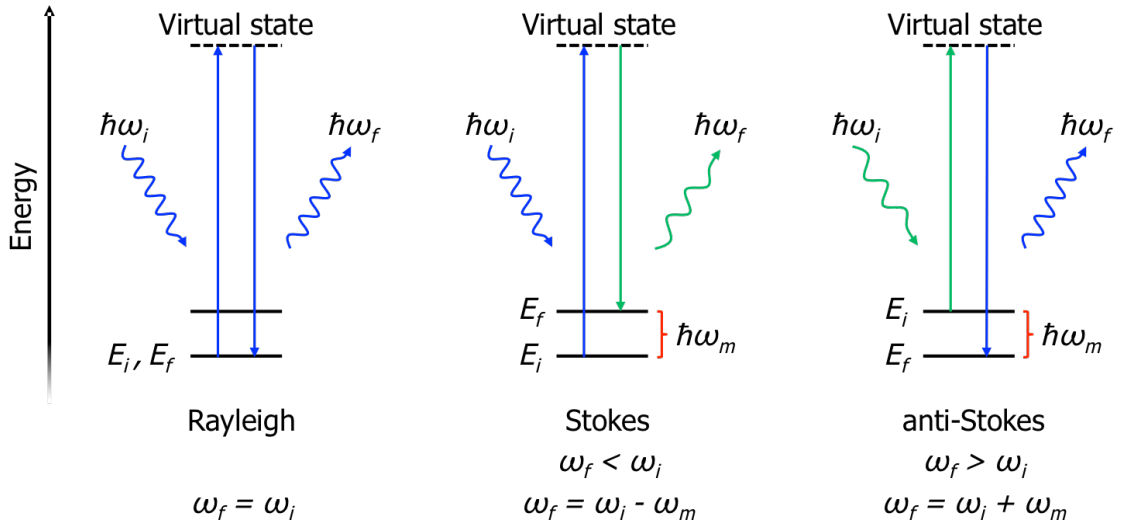

Figure 1.1 Schematic representations of the three possible scattering phenomena occurring in a Raman experiment.

From Equation 1.5, the analytical information provided by Raman spectroscopy can be understood: ω_i is the frequency of the excitation photon, which is known from the experimental setup adopted; ω_f is the observable, the outcoming light which is measured after the interaction with the material; and ω_m, which can be derived from the previous when inelastic scattering occurs, represents (as defined in Equation 1.1) the difference among two energy levels, *i.e.* a material property. To fully get the meaning of ω_m it is determinant to consider its order of magnitude: since this typically falls in the mid/far infrared range of frequencies, it can be ascribed to a vibrational (or rotational) mode of the material.

Another really important point is the intensity of the Raman signal, which has not been yet described. In the simplest case, when the excitation wavelength ω_i is really different from the ones of the electronic transitions of the material, a classical approach is sufficient to properly describe the origin of Raman intensity. The key point is the establishment of a induced dipole moment $\boldsymbol{\mu}$ when the electric field $\boldsymbol{E}$ of an electromagnetic wave with frequency

ω_i interacts with the system because of the polarization of the latter. The polarization extent is determined by the polarizability tensor $\boldsymbol{\alpha}$ of the material. It is important to recall that an oscillating dipole can act as a photon emitter and the intensity of the emitted radiation will be proportional to the square modulus of the dipole moment and to the fourth power of its oscillation frequency, *i.e.* $I \propto \omega^4 |\boldsymbol{\mu}|^2$. The dipole moment can be obtained from the product of the polarizability tensor and the electric field (Equation 1.6).

$$\boldsymbol{\mu} = \boldsymbol{\alpha} \cdot \boldsymbol{E} \tag{1.6}$$

If the scatterer is isotropic, the polarizability tensor is reduced to a scalar α: in the following this simplified approach will be followed. The polarizability is expected to vary when the molecular structure changes upon vibration: thereby, considering a specific vibrational mode m of frequency ω_m, α can be expanded through a Taylor series with respect to the normal coordinate Q_m of the vibrational mode (Equation 1.7).

$$\alpha = \alpha_0 + \left(\frac{\partial \alpha}{\partial Q_m}\right)_0 Q_m + \cdots = \alpha_0 + \beta Q_m + \cdots \tag{1.7}$$

In the tensorial treatment, each tensor component is expressed in this way separately. Since the series is rapidly converging, it can be conveniently truncated to the first order. Then explicitly describing the time dependence of Q_m (Equation 1.8) and $\boldsymbol{E}$ (Equation 1.9)

$$Q_m = Q_{m0} \cos(\omega_m t) \tag{1.8}$$

$$\boldsymbol{E} = \boldsymbol{E}_0 \cos(\omega_i t) \tag{1.9}$$

and thus substituting in Equation 1.6, Equation 1.10 is obtained.

$$\begin{aligned}\boldsymbol{\mu} &= [\alpha_0 + \beta Q_{m0}\cos(\omega_m t)] \cdot \boldsymbol{E}_0 \cos(\omega_i t) \\ &= \alpha_0 \boldsymbol{E}_0 \cos(\omega_i t) + \beta \boldsymbol{E}_0 Q_{m0} \cos(\omega_m t)\cos(\omega_i t)\end{aligned} \tag{1.10}$$

Finally applying the prosthaphaeresis trigonometric relations, Equation 1.10 can be rewritten as:

$$\begin{aligned}\boldsymbol{\mu} = \alpha_0 \boldsymbol{E}_0 \cos(\omega_i t) + \beta \boldsymbol{E}_0 Q_{m0} \big[&\cos\big((\omega_i - \omega_m)t\big) \\ &+ \cos\big((\omega_i + \omega_m)t\big)\big]\end{aligned} \tag{1.11}$$

Equation 1.11 gives the description of three distinct sources of radiation: the first term $\alpha_0 \boldsymbol{E}_0 \cos(\omega_i t)$ describes the emission of a light with the same frequency ω_i of the incident one, *i.e.* the Rayleigh scattering; the second term $\beta \boldsymbol{E}_0 Q_{m0} \cos\big((\omega_i - \omega_m)t\big)$ represents the production of an electromagnetic wave with lower frequency $\omega_i - \omega_m$ compared to the incident one, *i.e.* the Stokes scattering; the third term $\beta \boldsymbol{E}_0 Q_{m0} \cos\big((\omega_i + \omega_m)t\big)$ finally explains the anti-Stokes scattering, being the outcoming frequency $\omega_i + \omega_m$ larger than the incoming. Equation 1.11 further depicts the fundamental condition allowing Raman scattering to occur: the variation of the polarizability due to the vibrational mode of interest should be non-zero, thus $\beta \neq 0$.

Being appropriate for the description of "standard" Raman scattering, Equation 1.11 is not able instead to explain other effects, including the very important resonant Raman one. Resonant Raman is phenomenologically observed when the measurements are performed with an excitation wavelength falling close to one of an electronic transition of the material: as a consequence, some of the Raman signals of the sample show a notably increased intensity (sometime of orders of magnitude), whereas other vibrations are basically unaffected. In order to give an appropriate description

of this effect a quantum mechanical approach is required: since its full mathematical treatment is really complex and out of the scope of this thesis, just the key concepts will be reported and discussed. The basic for this theory is the Kramers-Heisenberg equation of 1925, originally developed to describe the cross section for the scattering of a photon by an atomic electron:[55] the same was re-derived some years later by Dirac with a fully quantum mechanical approach.[56] The Kramer-Heisenberg-Dirac results were subsequently modified by Behringer, employing the Franck-Condon principle,[57] and finally by Albrecht, who further introduced the Herzberg-Teller treatment for vibronic transitions in the former theory.[58] The Herzberg-Teller effect describes the dependence of an electronic Hamiltonian $\widehat{H}$ on the normal coordinate Q of a given vibration.[59] The dependence is expressed as a series expansion of $\widehat{H}$ with respect to Q around the equilibrium position Q_0: the vibrational perturbation to $\widehat{H}$ allows thus the mixing of electronic states. Applying the Herzberg-Teller expansion in the derivation of polarizabilities, the Albrecht theory is derived. The latter gives a satisfactory description of the resonant Raman effect: the key concept is to keep in mind that an electronic transition is always coupled with a change in the vibrational state of the absorber. This means that an electronic transition form a ground state $|\psi_g\rangle$ to an excited state $|\psi_e\rangle$ is actually a vibronic transition from a ground vibronic state $|i\rangle = |\psi_g\rangle|v_{g,1}\rangle$ to an excited vibronic state $|e\rangle = |\psi_e\rangle|v_e\rangle$. Then the Raman process further requires a decay from the $|e\rangle$ vibronic state to the final $|f\rangle = |\psi_g\rangle|v_{g,2}\rangle$ vibronic state owning to the electronic ground state. If $|v_{g,1}\rangle = |v_{g,2}\rangle$ Rayleigh scattering occurs, whereas Raman scattering is observed for $|v_{g,1}\rangle \neq |v_{g,2}\rangle$. The elements of the polarizability tensor $\alpha_{\rho\sigma}$ are defined in the Albrecht theory by a sum of terms (Equation 1.12).

$$(\alpha_{\rho\sigma})_{if} = A + B \tag{1.12}$$

The A addend in Equation 1.12 represents the zero order term of the Herzberg-Teller series, while the B term contains the first order dependence by Q. Explicitly, the A term is:

$$A = \frac{1}{\hbar}\langle\psi_g|\mu_\rho|\psi_e\rangle\langle\psi_e|\mu_\sigma|\psi_g\rangle \sum_{v_e} \frac{\langle v_{g,2}|v_e\rangle\langle v_e|v_{g,1}\rangle}{\omega_{\psi_e v_e,\psi_g v_{g,1}} - \omega_0 + i\Gamma_{\psi_e v_e}} \qquad (1.13)$$

Equation 1.13 is rather complex but its physical meaning can be easily understood by considering its components separately. The term external to the summation sign, $\langle\psi_g|\mu_\rho|\psi_e\rangle\langle\psi_e|\mu_\sigma|\psi_g\rangle$, is the product of the ρ and σ Cartesian components (*i.e.* being ρ and $\sigma = x, y, z$) of the dipole moments for the $|\psi_e\rangle \rightarrow |\psi_g\rangle$ and $|\psi_g\rangle \rightarrow |\psi_e\rangle$ electronic transitions. Inside the summation, the numerator $\langle v_{g,2}|v_e\rangle\langle v_e|v_{g,1}\rangle$ is the product of the Franck-Condon factors associated to the vibronic transitions $|i\rangle \rightarrow |e\rangle$ and $|e\rangle \rightarrow |f\rangle$; the denominator $\omega_{\psi_e v_e,\psi_g v_{g,1}} - \omega_0 + i\Gamma_{\psi_e v_e}$ contains the frequency of the vibronic transition $\omega_{\psi_e v_e,\psi_g v_{g,1}}$, the frequency of the incident light ω_0 and a damping factor $i\Gamma_{\psi_e v_e}$, related to the width of the state $|e\rangle$ (thus responsible of the Raman signal bandwidth). In order to achieve the resonance enhancement of the Raman signal from the A term two conditions must be satisfied: i) the dipole moments for the electronic transitions must be non-zero; ii) the Franck-Condon factors must be non-zero for at least a $|v_e\rangle$. The former condition is satisfied if the electronic transition are dipole permitted; further the contribution to the term increases together with the magnitude of the dipole, thus resonance Raman is favored if the excitation falls in the contour of a intense adsorption band (*e.g.* due to charge transfer or $\pi - \pi^*$ transitions). In order to satisfy the latter condition, the vibrational wavefunctions $|v_{g,1}\rangle$ and $|v_{g,2}\rangle$ must be non-orthogonal to $|v_e\rangle$ in order to obtain non-zero overlap integrals. Non-orthogonal wavefunctions are obtained in two ways: the shape

of the potential energy surface for $|\psi_g\rangle$ and $|\psi_e\rangle$ is different between the two electronic states (thus leading to different vibrational frequencies for the same mode) or the potential energy minimum for the $|\psi_e\rangle$ is displaced of a certain ΔQ with respect to $|\psi_g\rangle$ one along the normal coordinate Q of the considered vibrational mode. The latter case can occur only for totally symmetric modes (*i.e.* just modifying bond lengths and angles which won't bring to a change in the symmetry), then leading to a potential energy minimum displacement along the normal coordinate. The last consideration also infers that commonly the totally symmetric modes are the enhanced ones. The enhancement of the non-totally symmetric modes is possible as well and can become relevant for some specific systems (*e.g.* polycyclic aromatic hydrocarbons):[60] this part of the Raman information is contained in the B term of Equation 1.12 (reported in Equation 1.14).

$$B = \frac{1}{\hbar^2}\sum_{s\neq e}\langle\psi_g|\mu_\rho|\psi_s\rangle\langle\psi_e|\mu_\sigma|\psi_g\rangle \frac{h_{se}^k}{\omega_{\psi_e}-\omega_{\psi_s}}\sum_{\nu_e}\frac{\langle v_{g,2}|Q_k|v_e\rangle\langle v_e|v_{g,1}\rangle}{\omega_{\psi_e\nu_e,\psi_g\nu_{g,1}}-\omega_0+i\Gamma_{\psi_e\nu_e}} + \frac{1}{\hbar^2}\sum_{s\neq e}\langle\psi_g|\mu_\rho|\psi_e\rangle\langle\psi_s|\mu_\sigma|\psi_g\rangle \frac{h_{se}^k}{\omega_{\psi_e}-\omega_{\psi_s}}\sum_{\nu_e}\frac{\langle v_{g,2}|v_e\rangle\langle v_e|Q_k|v_{g,1}\rangle}{\omega_{\psi_e\nu_e,\psi_g\nu_{g,1}}-\omega_0+i\Gamma_{\psi_e\nu_e}} \quad (1.14)$$

The Herzberg-Teller vibronic coupling mechanism makes accessible a new excited state s through the normal coordinate Q_k, which is involved in determining the polarizability tensor. As for the A term, the electronic transitions involving the states $|\psi_e\rangle$, $|\psi_g\rangle$ and $|\psi_s\rangle$ must be dipole allowed to have a non-zero B. A new term h_{se}^k takes into account the vibronic coupling of the $|\psi_e\rangle$ and $|\psi_s\rangle$ states through the normal coordinate Q_k, given by:

$$h_{se}^k = \langle\psi_s|\,\delta\hat{H}/\delta Q_k\,|\psi_e\rangle \quad (1.15)$$

It is important to underline that Equation 1.15 can be non-zero independently from the symmetry of the vibration of normal coordinate Q_k, thus allowing the resonant enhancement of non-totally symmetric modes as well. Concerning the vibrational integrals $\langle v_{g,2}|Q_k|v_e\rangle\langle v_e|v_{g,1}\rangle$ and $\langle v_{g,2}|v_e\rangle\langle v_e|Q_k|v_{g,1}\rangle$ these differ from zero if $v_{g,2} = v_e \pm 1$ and $v_e = v_{g,1} \pm 1$ respectively (in the harmonic approximation). It is important to underline that Herzberg-Teller coupling can occur both during the photon absorption process as well as during is re-emission: this fact justifies the splitting of the B term in two additive contributions.

A summary of the theoretical description of resonant Raman is graphically given in Figure 1.2. In the schematic representation is shown as, in the case of the A term, the electronic transitions can occur only vertically, thus requiring a displacement of the potential minima for the states $|\psi_g\rangle$ and $|\psi_e\rangle$ to allow a transition between non-orthogonal vibrational states.

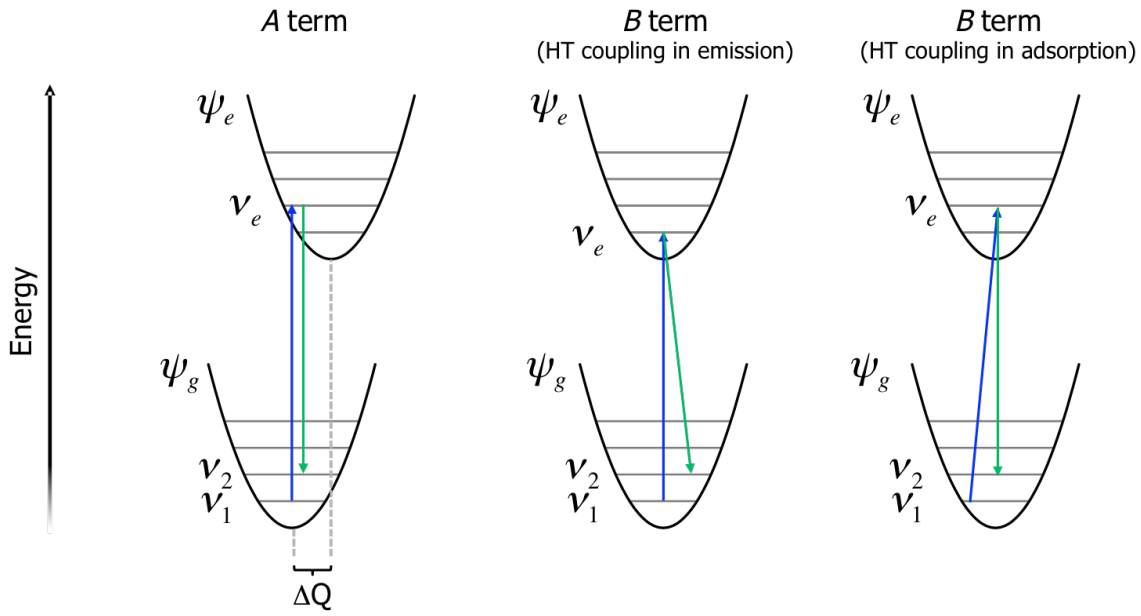

Figure 1.2 Schematic representation of the vibronic transitions originating resonant Raman. Only the case of Stokes scattering is reported.

Instead, when Herzberg-Teller vibronic coupling occurs, non-orthogonal vibrational state can be involved in the transitions just by non-vertical transitions: as a consequence, also non-totally symmetric vibrational modes can be resonantly enhanced.

As final remark to this section, the intensity of the Raman scattering is considered in an absolute way: it is in fact important to realize the extent of the probability that a photon is scattered according to this mechanism rather than being involved in other type of phenomena. The most convenient way to express this quantity is a cross section, *i.e.* as the number of photons (usually expressed as integrated area of the full Raman spectrum) belonging inelastic scattering per scattering center, per unit solid angle. In general Raman scattering is a very low probability event: in off-resonance conditions, in fact, the measured cross sections for some representative compounds/materials fall in the 10^{-28} - 10^{-30} $cm^2sr^{-1}molecule^{-1}$ range.[61,62] Raman cross sections can improve significantly by exploiting resonance conditions, thus increasing the cross section up to 5-7 orders of magnitude.[63–65] However, these value are still really small when compared with the cross section for other phenomena possibly competing with Raman: that is the unlucky case of fluorescence, which cross section values span in the 10^{-23} - 10^{-25} $cm^2sr^{-1}molecule^{-1}$ range. This means that the collection of the Raman signal is often affected by contributions from other phenomena (and particularly by fluorescence): in some specific cases the Raman spectra can be completely buried by a fluorescence profile, thus making the technique inapplicable. Such a problem is of particular relevance for zeolites: the strategies adopted toward its solution will be commented in detail in the following section.

1.3 The challenge: Raman of zeolites

In the field of zeolites, Raman is a useful and straightforward method to study the vibrational properties of the zeolitic framework: the easier way to understand this ability is to compare the Raman spectrum of a zeolite with its corresponding infrared spectrum (Figure 1.3).

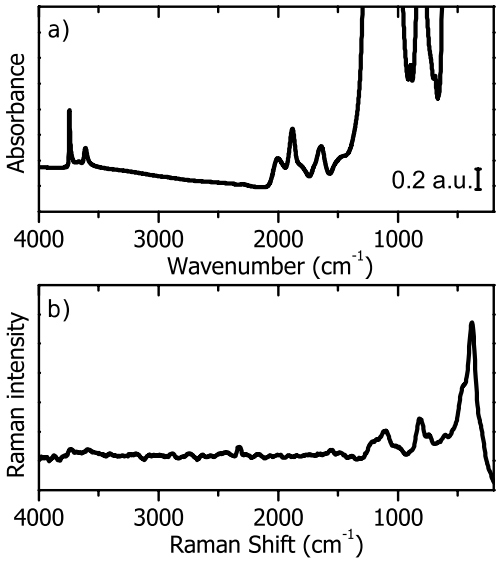

Figure 1.3 Comparison of the a) FTIR (transmission mode) and b) Raman (λ = 244 nm) spectra of a H-ZSM-5 zeolite (Sud Chemie, Si/Al = 45).

The differences in term of relative intensities are remarkable: without entering in detail with the assignment of all the spectral features (see Chapter 3 for a deeper comment), both the spectra can be divided in a high (ν > 2000 cm^{-1}) and a low (ν < 2000 cm^{-1}) frequency regions. The former is interested for zeolites by the presence of the typical stretching vibrations of OH groups (both terminal/defective silanols and Brønsted sites): in the case of FTIR spectroscopy these signals (collected in transmission mode) are intense and well defined, whereas with Raman only weak (sometime nil) features can be collected. The latter, instead, is characteristic for framework vibrational modes: concerning FTIR all the features (with the exception of the overtones

around 1600-2000 cm^{-1}) are too intense, resulting in an out-of-scale signal where most of the information is lost; conversely Raman shows an optimal signal intensity in this region, being all the main spectral features easily recognized. Furthermore Raman (thanks to its instrumental building) is able to reach lower frequency values, whereas special setups are required to do the same by FTIR. Thus Raman is useful in zeolites characterization since it is capable to properly give the vibrational picture of the so-called framework modes, where FTIR instead typically fails. However, as for every technique, also Raman spectroscopy shows some limitations: the first, important drawback is that the Raman effect is characterized by a very small cross section (see the previous section), thus a high brilliance of the excitation source is required in order to obtain spectra with a good S/N ratio in a reasonable time framework. Because of this reason, the sources for Raman spectrometers are typically lasers, since these are able to produce a high photon flux, coherent light beam. To further increase the number of the inelastic scattering events, the excitation laser is usually converged on the sample through lenses and even by microscopes: concentrating the photons flux on a smaller scattering volumes the intensity of the signal can be further increased. These precautions are really useful in increasing the collected Raman intensity at equal collection times, or to shorten the time lapse required to collect a spectrum of same quality. However some drawbacks are introduced as well: since the incoming radiation is really intense, the overheating induced by the high photon flux can damage some type of materials. This is true especially for organic species, which can belong a burning-like process thus converting them in carbonaceous residuals. When the excitation source owns particularly high photons energy (*e.g.* as in the case of UV lasers), further photochemical damage could be observed, coming to similar outcomes. The most feasible way to avoid (or at least to limit) such damages is to reduce the incident laser power: in this way more reliable data

are collected, paying the price of a lower signal-to-noise ratio *i.e.* longer acquisition time. Even if this procedure is the best compromise, it becomes seriously limiting for the applicability of Raman spectroscopy anytime time-resolved experiments would be performed. A possible way to exploit higher excitation powers but avoiding the sample damaging is to spread the measurement hot-spot on the larger fraction of sample possible: in other words, if the sample is continuously moved under the laser beam, each point on its surface is enlightened by the high photons flux for a brief time, possibly too short to cause a photoinduced damage. Several technical solutions have been developed along the last 40 years to exploit this concept:[66–70] the milestones of this process will be discussed in Chapter 2, together with an in-depth discussion on the device specifically developed during this doctorate.

If the laser power *vs* photoinduced damage issue can be addressed adopting appropriate technical solutions, fluorescence often represents an unavoidable side effect, which could make the collection of the Raman signal impossible. As commented in the previous section of this chapter, the usual cross sections for fluorescence emission are at least comparable with those of resonant Raman, whereas they can overcame off-resonance Raman ones by orders of magnitude. Practically this means that if fluorescence occurs the Raman signal is "buried" by the emission profile, even if strong resonance can be achieved. Concerning zeolites, the problem is even worse since: i) the Raman cross-section for silicates is intrinsically low; ii) the microporous structure favors adsorption processes, including ones of organic molecules expected to be the main source of fluorescence. The ways to limit the fluorescence to a reasonable extent are mainly two: the simpler approach is to drastically eliminate the sources of emission, thus by opportunely treat the sample in order to remove them. In the case of adsorbed organic species, the easier procedure is to "burn them out" through an oxidative treatment: the simplest approach is the calcination at high temperature in an oxygen rich gas

mixture (*e.g.* air). Such treatments show variable efficiency depending on the calcination conditions (*e.g.* tempterature, static atmosphere *vs* flow, air *vs* pure O_2, etc.) as well as toward different materials. This means that a general treatment scheme (*i.e.* effective for every zeolite) is not feasible and the right conditions for each material have to be determined by dedicated experiments. However calcination is often not sufficient to completely deplete the sources of fluorescence and also traces of these residuals can produce sufficient emission to totally lose the Raman signal. An example comparing the outcomes of different calcinations is given in Figure 1.4.

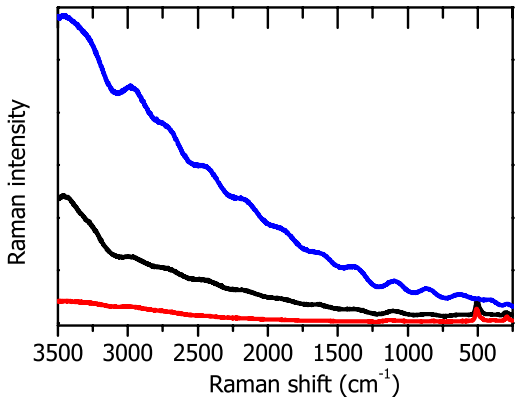

Figure 1.4 Raman spectra (λ = 442 nm) of a Na-Y zeolite obtained upon different activation treatments: not activated (black line), calcined in pure O_2 flow at 450°C (red line) and calcined in vacuum at 450°C (blue line).

Already in the case of the bare sample measured in air, even if the typical framework modes of Y zeolite are recognized at ~ 500 cm^{-1} and ~ 300 cm^{-1},[71,72] a significant fluorescence profile is observed. The choice of the activation strategy is then determining: the classical vacuum activation as frequently performed for FTIR experiments leads to a failing result, since it only causes the uncontrolled increase of fluorescence now totally overwhelming the Raman signal. The only way to obtain an improvement of the Raman spectrum is to move toward flow calcination in pure O_2 stream: in such case it is possible to reduce the fluorescence in an effective way, but the "cost" of the operation is

high. In fact, the treatment time required to achieve this result is extremely long, since a slow temperature ramp has to be followed to guarantee a correct dehydration of the sample (thus avoiding undesired dealumination, *e.g.* see Chapter 3). Furthermore the calcination at high temperature should be as long as possible in order to obtain the best results: in the reported spectrum, the sample was kept at 450 °C for 6 h, with an overall activation time of more than 10 h. An alternative to harsh and time consuming activation procedures is offered by the physics of luminescence: fluorescence is observed when a photon is absorbed by a chromophore and thus re-emitted with a lower energy, being the spectral region of interest the visible one for most of the emissive moieties. Thus, if excitation wavelengths sufficiently far from visible are exploited in the Raman measurement, the emission occurs in a different spectral region with respect to the one where Raman scattering is occurring. In practice, such condition can be achieved using ultra-violet or infrared lasers.[73] An alternative way to avoid fluorescence can be represented by the collection of the anti-Stokes branch of the Raman spectrum, *i.e.* falling above the excitation energy thus far from the emission spectral region (even if this is not certain, as photon upconversion phenomena could occur). This peculiar modality was not exploited in this thesis since the available instrumentation does not allow it. The former possibility is thus more interesting, in particular UV-Raman because: i) the intrinsically higher intensity associated to high frequency excitations ($I \propto \omega^4$); ii) the possibility to exploit the resonance for the numerous moieties owning absorption bands in the UV region; and iii) the lower extent of black-body emission in the UV region, thus allowing to easier perform experiments at high temperature. The UV-Raman technique was indeed one of the most successful in zeolites characterization, as demonstrated by the high quality of the related literature.[40,69,73–81] Despite these advantages, the photoinduced damage becomes a severe drawback in UV-Raman, being in most of the cases photochemical processes involved: the

exploitation of sample movement becomes of outmost importance for this specific approach.

In the next chapters of this thesis the application of UV-Raman to two case studies will be shown: i) the activation and reactivity toward methanol of H-ZSM-5; and ii) the characterization of TS-1 samples with different Ti speciations. The former topic strictly followed the development of the setup as described in Chapter 2, representing an optimal testing and optimization opportunity for the same. The latter study instead was carried on with more fundamental purposes: exploiting the new possibilities opened by the setup, a fine characterization of TS-1 was performed, complemented by a multi-technique approach. A parallel quantum mechanical modeling has been established in order to increase the understanding on the basic physics of the previous experimental evidences.

References

(1) Meier, W. M. Zeolites and Zeolite-like Materials. *Pure Appl. Chem.* **1986**, *58* (10), 1323—1328.

(2) Baerlocher, C.; McCusker, L. B.; Olson, D. H. *Atlas of Zeolite Framework Types*, 6th ed.; Elsevier, **2007**.

(3) From the International Zeolites Association Structure Commission website: http://www.iza-structure.org/.

(4) Cronstedt, A. F. Om En Obekant Bårg Art, Som Kallas Zeolites. *K. Sven. vetensk.akad. handl.* **1756**, 120–123.

(5) Flanigen, E. M.; Bennett, J. M.; Grose, R. W.; Cohen, J. P.; Patton, R. L.; Kirchner, R. M.; Smith, J. V. Silicalite, a New Hydrophobic Crystalline Silica Molecular Sieve. *Nature* **1978**, *271* (5645), 512–516.

(6) Bibby, D. M.; Milestone, N. B.; Aldridge, L. P. Silicalite-2, a Silica Analogue of the Aluminosilicate Zeolite ZSM-11. *Nature* **1979**, *280* (5724), 664–665.

(7) Camblor, M. A.; Corma, A.; Valencia, S. Spontaneous Nucleation and Growth of Pure Silica Zeolite-Beta Free of Connectivity Defects. *Chem. Commun.* **1996**, No. 20, 2365-2366.

(8) Díaz-Cabañas, M.-J.; Barrett, P. A. Synthesis and Structure of Pure SiO_2 Chabazite: the SiO_2 Polymorph with the Lowest Framework Density. *Chem. Commun.* **1998**, No. 17, 1881–1882.

(9) Boyd, G. E.; Adamson, W.; Myers, L. S. The Exchange Adsorption of Ions from Aqueous Solutions by Organic Zeolites; Kinetics. *J. Am. Chem. Soc.* **1947**, *69* (11), 2836–2848.

(10) Erdem, E.; Karapinar, N.; Donat, R. The Removal of Heavy Metal Cations by Natural Zeolites. *J. Colloid Interface Sci.* **2004**, *280* (2), 309–314.

(11) Wang, S.; Peng, Y. Natural Zeolites as Effective Adsorbents in Water and Wastewater Treatment. *Chem. Eng. J.* **2010**, *156* (1), 11–24.

(12) Walton, K. S.; Abney, M. B.; Douglas LeVan, M. CO_2 Adsorption in Y and X Zeolites Modified by Alkali Metal Cation Exchange. *Microporous Mesoporous Mater.* **2006**, *91* (1), 78–84.

(13) Montanari, T.; Busca, G. On the Mechanism of Adsorption and Separation of CO_2 on LTA Zeolites: An IR Investigation. *Vib. Spectrosc.* **2008**, *46* (1), 45–51.

(14) Yang, S.-T.; Kim, J.; Ahn, W.-S. CO_2 Adsorption over Ion-Exchanged Zeolite Beta with Alkali and Alkaline Earth Metal Ions. *Microporous Mesoporous Mater.* **2010**, *135* (1–3), 90–94.

(15) Palomino, M.; Corma, A.; Rey, F.; Valencia, S. New Insights on CO_2-Methane Separation Using LTA Zeolites with Different Si/Al Ratios and a First Comparison with MOFs. *Langmuir* **2010**, *26* (3), 1910–1917.

(16) Brandenberger, S.; Kröcher, O.; Tissler, A.; Althoff, R.; Kroecher, O.; Tissler, A.; Althoff, R. The State of the Art in Selective Catalytic Reduction of NO_x by Ammonia Using Metal-Exchanged Zeolite Catalysts.

Catal. Rev. **2008**, *50* (4), 492–531.

(17) Kwak, J. H.; Tonkyn, R. G.; Kim, D. H.; Szanyi, J.; Peden, C. H. F. Excellent Activity and Selectivity of Cu-SSZ-13 in the Selective Catalytic Reduction of NO_x with NH_3. *J. Catal.* **2010**, *275* (2), 187–190.

(18) Fickel, D. W.; D'Addio, E.; Lauterbach, J. A.; Lobo, R. F. The Ammonia Selective Catalytic Reduction Activity of Copper-Exchanged Small-Pore Zeolites. *Appl. Catal. B Environ.* **2011**, *102* (3–4), 441–448.

(19) Lallemand, M.; Finiels, A.; Fajula, F.; Hulea, V. Catalytic Oligomerization of Ethylene over Ni-Containing Dealuminated Y Zeolites. *Appl. Catal. A Gen.* **2006**, *301* (2), 196–201.

(20) Mlinar, A. N.; Baur, G. B.; Bong, G. G.; Getsoian, A.; Bell, A. T. Propene Oligomerization over Ni-Exchanged Na-X Zeolites. *J. Catal.* **2012**, *296*, 156–164.

(21) Haw, J. F.; Nicholas, J. B.; Xu, T.; Beck, L. W.; Ferguson, D. B. Physical Organic Chemistry of Solid Acids: Lessons From in Situ NMR and Theoretical Chemistry. *Acc. Chem. Res.* **1996**, *29* (6), 259–267.

(22) Marcilly, C. Where and How Shape Selectivity of Molecular Sieves Operates in Refining and Petrochemistry Catalytic Processes. *Top. Catal.* **2000**, *13* (4), 357–366.

(23) Smit, B.; Maesen, T. L. M. Towards a Molecular Understanding of Shape Selectivity. *Nature* **2008**, *451* (7179), 671–678.

(24) Degnan, Jr., T. F. Applications of Zeolites in Petroleum Refing. *Top. Catal.* **2000**, *13* (4), 349–356.

(25) Corma, A.; Martínez, A. Zeolites in Refining and Petrochemistry. In *Studies in Surface Science and Catalysis*; **2005**; Vol. 157, pp 337–366.

(26) Lok, B. M.; Messina, C. A.; Patton, R. L.; Gajek, R. T.; Cannan, T. R.; Flanigen, E. M. Silicoaluminiphosphate Molecular Sieves: Another New Class of Microporus Crysalline Inorganic Solids. *J. Am. Chem. Soc.* **1984**, *106* (8), 6092–6093.

(27) Wilson, S. T.; Lok, B. M.; Messina, C. A.; Cannan, T. R.; Flanigen, E. M. Aluminophosphate Molecular Sieves: A New Class of Microporous Crystalline Inorganic Solids. *J. Am. Chem. Soc.* **1982**, *104* (4), 1146–1147.

(28) Gabelica, Z.; Guth, J. L. Germanium-Rich MFI Zeolites : The First Example of An Extended Framework Substitution of Silicon By Another Tetravalent Element. In *Studies in Surface Science and Catalysis*; **1989**; Vol. 49, pp 421–430.

(29) Bu, X.; Feng, P.; Gier, T. E.; Zhao, D.; Stucky, G. D. Hydrothermal Synthesis and Structural Characterization of Zeolite-like Structures Based on Gallium and Aluminum Germanates. *J. Am. Chem. Soc.* **1998**, *120* (51), 13389–13397.

(30) Su, J.; Wang, Y.; Wang, Z.; Lin, J. PKU-9: An Aluminogermanate with a New Three-Dimensional Zeolite Framework Constructed from CGS Layers and *Spiro* -5 Units. *J. Am. Chem. Soc.* **2009**, *131* (17), 6080–6081.

(31) Hua, W.; Chen, H.; Yu, Z.-B.; Zou, X.; Lin, J.; Sun, J. A Germanosilicate Structure with 11×11×12-Ring Channels Solved by Electron Crystallography. *Angew. Chemie Int. Ed.* **2014**, *53* (23), 5868–5871.

(32) Jiang, J.; Yun, Y.; Zou, X.; Jorda, J. L.; Corma, A. ITQ-54: A Multi-Dimensional Extra-Large Pore Zeolite with 20×14×12-Ring Channels. *Chem. Sci.* **2015**, *6* (1), 480–485.

(33) Notari, B.; Perego, G.; Taramasso, M. Preparation of Porous Crystalline Synthetic Material Comprised of Silicon and Titanium Oxides. *US4410501 A*, **1983**.

(34) Bellussi, G.; Carati, A.; Clerici, M. G.; Esposito, A.; Millini, R.; Buonomo, F. Procede Pour La Preparation de Materiaux Synthetiques Cristallins Poreux Constitues d'Oxydes de Silicium et de Titane. *BE1001038 (A7)*, **1989**.

(35) Camblor, M. A.; Corma, A.; Pérez-Pariente, J. Synthesis of Titanoaluminosilicates Isomorphous to Zeolite Beta, Active as Oxidation Catalysts. *Zeolites* **1993**, *13* (2), 82–87.

(36) Eilertsen, E. A.; Giordanino, F.; Lamberti, C.; Bordiga, S.; Damin, A.; Bonino, F.; Olsbye, U.; Lillerud, K. P. Ti-STT: A New Zeotype Shape Selective Oxidation Catalyst. *Chem. Commun.* **2011**, *47* (43), 11867–11869.

(37) Eilertsen, E. A.; Bordiga, S.; Lamberti, C.; Damin, A.; Bonino, F.; Arstad, B.; Svelle, S.; Olsbye, U.; Lillerud, K. P. Synthesis of Titanium Chabazite: A New Shape Selective Oxidation Catalyst with Small Pore Openings and Application in the Production of Methyl Formate from Methanol. *ChemCatChem* **2011**, *3* (12), 1869–1871.

(38) Notari, B. Microporous Crystalline Titanium Silicates. In *Advances in Catalysis*; Eley, D. D., Haag, W. O., Gates, B., Eds.; Elsevier Academic Press Inc: San Diego, **1996**; Vol. 41, pp 253–334.

(39) Romano, U.; Ricci, M. Industrial Applications. In *Liquid Phase Oxidation via Heterogeneous Catalysis*; Clerici, M. G., Kholdeeva, O. A., Eds.; John Wiley & Sons, Inc.: Hoboken, New Jersey, **2013**; pp 451–506.

(40) Bordiga, S.; Damin, A.; Bonino, F.; Ricchiardi, G.; Lamberti, C.; Zecchina, A. The Structure of the Peroxo Species in the TS-1 Catalyst as Investigated by Resonant Raman Spectroscopy. *Angew. Chemie-International Ed.* **2002**, *41* (24), 4734–4737.

(41) Prestipino, C.; Bonino, F.; Usseglio, S.; Damin, A.; Tasso, A.; Clerici, M. G.; Bordiga, S.; D'Acapito, F.; Zecchina, A.; Lamberti, C. Equilibria between Peroxo and Hydroperoxo Species in the Titanosilicates: An in Situ High-Resolution XANES Investigation. *ChemPhysChem* **2004**, *5* (11), 1799–1804.

(42) Bordiga, S.; Bonino, F.; Damin, A.; Lamberti, C. Reactivity of Ti(iv) Species Hosted in TS-1 towards H_2O_2–H_2O Solutions Investigated by Ab

Initio Cluster and Periodic Approaches Combined with Experimental XANES and EXAFS Data: A Review and New Highlights. *Phys. Chem. Chem. Phys.* **2007**, *9* (35), 4854–4878.

(43) Neri, C.; Anfossi, B.; Esposito, A.; Buonomo, F. Process for the Epoxidation of Olefinic Compounds. *US4833260 (A)*, **1984**.

(44) Roffia, P.; Padovan, M.; Moretti, E.; De Alberti, G. Catalytic Process for Preparing Cyclohexanone-Oxime. *US 4745221 (A)*, **1988**.

(45) Chester, A. W.; Derouane, E. G. *Zeolite Chemistry and Catalysis*; Springer Netherlands: Dordrecht, **2009**.

(46) Lercher, J. A.; Gründling, C.; Eder-Mirth, G. Infrared Studies of the Surface Acidity of Oxides and Zeolites Using Adsorbed Probe Molecules. *Catal. Today* **1996**, *27* (3–4), 353–376.

(47) Zecchina, A.; Spoto, G.; Bordiga, S. Probing the Acid Sites in Confined Spaces of Microporous Materials by Vibrational Spectroscopy. *Phys. Chem. Chem. Phys.* **2005**, *7* (8), 1627.

(48) van Bokhoven, J. A.; Lamberti, C. Structure of Aluminum, Iron, and Other Heteroatoms in Zeolites by X-Ray Absorption Spectroscopy. *Coord. Chem. Rev.* **2014**, *277*, 275–290.

(49) Bordiga, S.; Lamberti, C.; Bonino, F.; Travert, A.; Thibault-Starzyk, F. Probing Zeolites by Vibrational Spectroscopies. *Chem. Soc. Rev.* **2015**, *44* (20), 7262–7341.

(50) Raman, C. V.; Krishnan, K. S. A New Type of Secondary Radiation. *Nature* **1928**, *121*, 501–502.

(51) Smekal, A. Zur Quantentheorie Der Dispersion. *Naturwissenschaften* **1923**, *11* (43), 873–875.

(52) Landsberg, G.; Mandelstam, L. Eine Neue Erscheinung Bei Der Lichtzerstreuung in Krystallen. *Naturwissenschaften* **1928**, *16* (28), 557–558.

(53) Long, D. A. *The Raman Effect*; John Wiley & Sons, Ltd: Chichester, UK,

2002.

(54) Browne, W. R.; McGarvey, J. J. The Raman Effect and Its Application to Electronic Spectroscopies in Metal-Centered Species: Techniques and Investigations in Ground and Excited States. *Coord. Chem. Rev.* **2007**, *251* (3), 454–473.

(55) Kramers, H. A.; Heisenberg, W. Über Die Streuung von Strahlung Durch Atome. *Zeitschrift für Phys.* **1925**, *31* (1), 681–708.

(56) Dirac, P. A. M. The Quantum Theory of Dispersion. *Proc. R. Soc. A Math. Phys. Eng. Sci.* **1927**, *114* (769), 710–728.

(57) Behringer, J. Zur Theorie Des Resonanz-Raman-Effektes. *Zev. F. Elektrochemie Ber. der Bunsen Ges. für Phys.* **1958**, *62* (8), 906–914.

(58) Albrecht, A. C. On the Theory of Raman Intensities. *J. Chem. Phys.* **1961**, *34* (5), 1476-1484.

(59) Herzberg, G.; Teller, E. Schwingungsstruktur Der Elektronenübergange Bei Mehratomigen Moleklen. *Zeitschrift für Phys. Chemie B* **1933**, *21*, 410.

(60) Avila Ferrer, F. J.; Barone, V.; Cappelli, C.; Santoro, F. Duschinsky, Herzberg–Teller, and Multiple Electronic Resonance Interferential Effects in Resonance Raman Spectra and Excitation Profiles. The Case of Pyrene. *J. Chem. Theory Comput.* **2013**, *9* (8), 3597–3611.

(61) McCreery, R. L. Photometric Standards for Raman Spectroscopy. In *Handbook of Vibrational Spectroscopy*; Griffiths, P. R., Ed.; John Wiley & Sons, Ltd: Chichester, UK, **2006**; pp 920–932.

(62) Aggarwal, R. L.; Farrar, L. W.; Saikin, S. K.; Aspuru-Guzik, A.; Stopa, M.; Polla, D. L. Measurement of the Absolute Raman Cross Section of the Optical Phonon in Silicon. *Solid State Commun.* **2011**, *151* (7), 553–556.

(63) Shim, S.; Stuart, C. M.; Mathies, R. A. Resonance Raman Cross-Sections and Vibronic Analysis of Rhodamine 6G from Broadband Stimulated

Raman Spectroscopy. *ChemPhysChem* **2008**, *9* (5), 697–699.

(64) Le Ru, E. C.; Schroeter, L. C.; Etchegoin, P. G. Direct Measurement of Resonance Raman Spectra and Cross Sections by a Polarization Difference Technique. *Anal. Chem.* **2012**, *84* (11), 5074–5079.

(65) Silva, W. R.; Keller, E. L.; Frontiera, R. R. Determination of Resonance Raman Cross-Sections for Use in Biological SERS Sensing with Femtosecond Stimulated Raman Spectroscopy. *Anal. Chem.* **2014**, *86* (15), 7782–7787.

(66) Kiefer, W.; Bernstein, H. J. Rotating Raman Sample Technique for Colored Crystal Powders; Resonance Raman Effect in Solid $KMnO_4$. *Appl. Spectrosc.* **1971**, *25* (6), 609–613.

(67) Cheng, C. P.; Ludowise, J. D.; Schrader, G. L. Controlled-Atmosphere Rotating Cell for in Situ Studies of Catalysts Using Laser Raman Spectroscopy. *Appl. Spectrosc.* **1980**, *34* (2), 146–150.

(68) Müller, A.; Weber, T. In Situ Raman Investigation of Hydrodesulphurization Catalysts. *Appl. Catal.* **1991**, *77* (2), 243–250.

(69) Chua, Y.; Stair, P. C. A Novel Fluidized Bed Technique for Measuring UV Raman Spectra of Catalysts and Adsorbates. *J. Catal.* **2000**, *196* (1), 66–72.

(70) Beato, P.; Schachtl, E.; Barbera, K.; Bonino, F.; Bordiga, S. Operando Raman Spectroscopy Applying Novel Fluidized Bed Micro-Reactor Technology. *Catal. Today* **2013**, *205*, 128–133.

(71) Dutta, P. K.; Twu, J. Influence of Framework Silicon/aluminum Ratio on the Raman Spectra of Faujasitic Zeolites. *J. Phys. Chem.* **1991**, *95* (6), 2498–2501.

(72) Bremard, C.; Le Maire, M. Low-Frequency Raman Spectra of Dehydrated Faujasitic Zeolites. *J. Phys. Chem.* **1993**, *97* (38), 9695–9702.

(73) Fan, F.; Feng, Z.; Li, C. UV Raman Spectroscopic Studies on Active Sites and Synthesis Mechanisms of Transition Metal-Containing Microporous

and Mesoporous Materials. *Acc. Chem. Res.* **2010**, *43* (3), 378–387.

(74) Bordiga, S.; Damin, A.; Bonino, F.; Ricchiardi, G.; Zecchina, A.; Tagliapietra, R.; Lamberti, C. Resonance Raman Effects in TS-1: The Structure of Ti(IV) Species and Reactivity towards H_2O, NH_3 and H_2O_2: An in Situ Study. *Phys. Chem. Chem. Phys.* **2003**, *5* (20), 4390–4393.

(75) Chua, Y. T.; Stair, P. C. An Ultraviolet Raman Spectroscopic Study of Coke Formation in Methanol to Hydrocarbons Conversion over Zeolite H-MFI. *J. Catal.* **2003**, *213* (1), 39–46.

(76) Li, C.; Stair, P. C. Ultraviolet Raman Spectroscopy Characterization of Coke Formation in Zeolites. *Catal. Today* **1997**, *33* (1–3), 353–360.

(77) Li, C. Identifying the Isolated Transition Metal Ions/oxides in Molecular Sieves and on Oxide Supports by UV Resonance Raman Spectroscopy. *J. Catal.* **2003**, *216* (1–2), 203–212.

(78) Li, C.; Xiong, G.; Liu, J.; Ying, P.; Xin, Q.; Feng, Z. Identifying Framework Titanium in TS-1 Zeolite by UV Resonance Raman Spectroscopy. *J. Phys. Chem. B* **2001**, *105* (15), 2993–2997.

(79) Stair, P. C. The Application of UV Raman Spectroscopy for the Characterization of Catalysts and Catalytic Reactions. *Advances in Catalysis*. **2007**, pp 75–98.

(80) Bonino, F.; Damin, A.; Piovano, A.; Lamberti, C.; Bordiga, S.; Zecchina, A. Direct Evidence of Highly Dispersed Iron in Fe-Silicalite: A Raman Spectroscopic Study. *ChemCatChem* **2011**, *3* (1), 139–142.

(81) Guo, Q.; Feng, Z.; Li, G.; Fan, F.; Li, C. Finding The "missing Components" during the Synthesis of TS-1 Zeolite by UV Resonance Raman Spectroscopy. *J. Phys. Chem. C* **2013**, *117* (6), 2844–2848.

Chapter 2

The development of a new setup: toward in situ and operando Raman of zeolites

As already discussed in Chapter 1, the Raman approach to zeolites characterization is often a complex task. Recalling the main reasons, the sample damaging induced by the intense excitation lasers and the strong fluorescence from these samples are the most critical drawbacks. The latter can be solved by choosing excitation wavelengths far from the typical emission region (*i.e.* UV or IR),[1] whereas the former can be avoided by continuously changing the spot on the sample exposed to the laser beam. In order to exploit such solution the sample must be kept moving during the whole measurement. Of course it is necessary to avoid as much as possible the reduction of the spectral quality caused by the movement, thus the design of a dedicated setup requires a careful consideration of all the possible sources of interference to the Raman signal. A number of examples of setups are available in the literature, everyone with its strengths and weaknesses: before to introduce the solution specifically developed for this thesis work, an in depth review of the previous milestone in this field will be given. Emphasis will be in particular on setups devoted to solids and solid-gas interaction studies, *i.e.* closely related to the kind of experimental approach exploited along this thesis.

2.1 Raman and sample movement: state of art

The first example of a Raman measurement performed with a moving sample reported in the literature is probably represented by the rotating sample holder developed by Kiefer and Bernstein in 1971.[2] The concept of the device, as schematized in Figure 2.1, is really simple: the powder is pressed in

a circular groove of the sample holder (forming a ring-shaped, self-supported pellet) and the analysis is performed sampling the material while it is rotated.

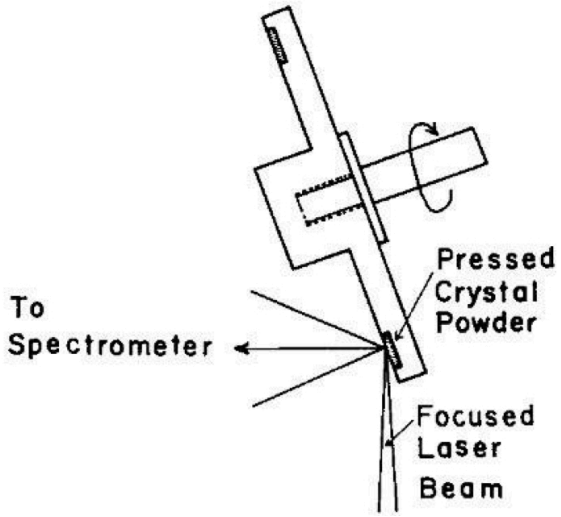

Figure 2.1 Scheme of the rotating sample holder by Kiefer and Bernstein. Reproduced from Ref. 2.

This solution allowed its inventors to measure a highly absorbing material such as potassium permanganate without destroying it, thus demonstrating the positive effect of the sample rotation.

Cheng and coworkers exploited again the same concept 9 years later, according to the construction outlined in Figure 2.2.[3]

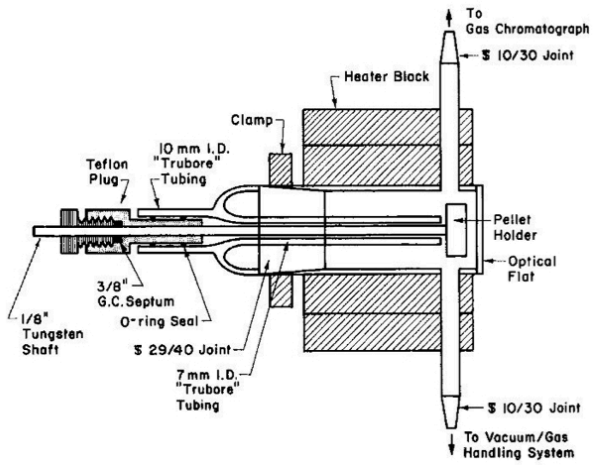

Figure 2.2 Scheme of the controlled atmosphere cell with rotating sample by Cheng and coworkers. Reproduced from Ref. 3.

The proposed cell introduces several evolutions with respect to the previous one: now the rotating sample holder is enveloped in a sealed chamber, allowing to expose the sample to a desired pressure/flow of a gas or to vacuum. Further temperature control is made possible by an external furnace and/or by flowing gases at a given temperature. The rotation is transmitted to the sample holder by an external motor and the coupling of the two parts is probably the most complex feature of the cell (and also its Achilles' heel): because of the complicated driving system, the cell «*presents technical problems in minimizing the mechanical distortions […] and in the sealing of the cell*» as commented by Müller and Weber.[4] The latter proposed an alternative solution, as depicted in Figure 2.3.

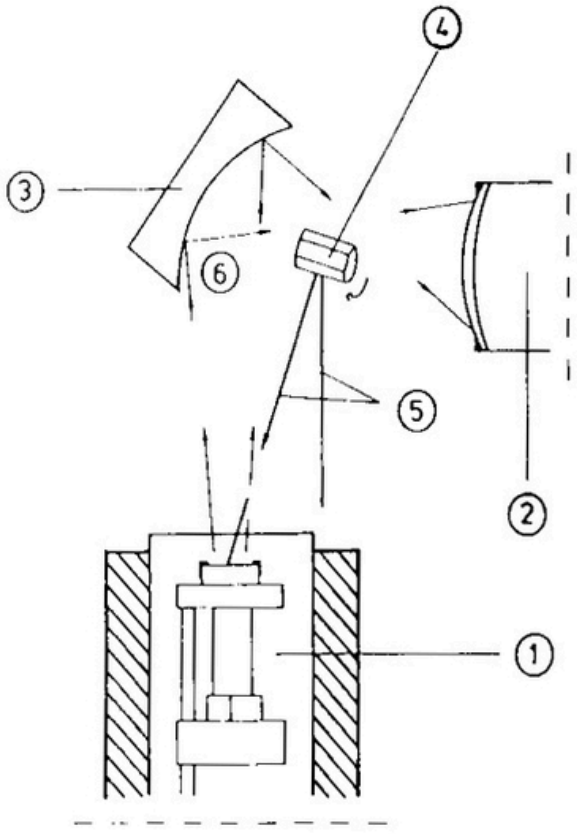

Figure 2.3 Scheme of the controlled atmosphere cell with scanning excitation laser by Müller and Weber. Reproduced from Ref. 3.

The novelty of such device is to avoid any mechanical part in the controlled atmosphere region of the cell, ascribing to the complex system of transmission of motion the weakness of the previous setup. Thus, instead of moving the sample itself, it is scanned by a movable laser beam: the incoming light is reflected by a rotating prismatic mirror (n. 4 in Figure 2.3), changing time by time the position of the measurement spot on the material. The scattered light is then recollected by a concave mirror and directed to the collection optics. Even if the present solution simplifies the problem of the cell sealing, it introduces new sources of aberration: it is possible to infer that the optimal collection of the Raman signal requires a high quality alignment of the optical elements, so each experiment is necessarily preceded by a time consuming optimization of the Raman instrumentation.

Reaching the 2000's the development of new Raman setups was progressively oriented to the study of reactions while occurring, *i.e.* carrying out the measurements in the so called *operando* conditions.[5] Anticipating the definition by Bañares, Chua and Stair developed in 2000 a new type of cell, more precisely definable as a reactor:[6] The sketch of the reactor-cell is reported in Figure 2.4.

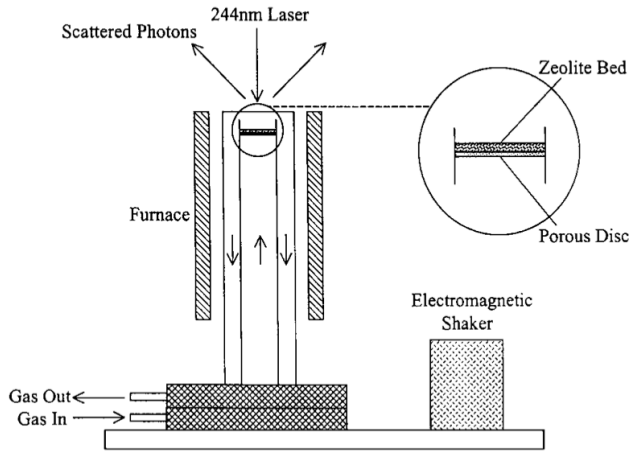

Figure 2.4 Scheme of the fluidized bed reactor-cell by Chua and Stair. Reproduced from Ref. 6.

Even if the reactions were not followed by online products analysis, the reactor was constructed in order to allow the spectroscopic study in realistic reaction conditions: in particular the authors focused on the formation of coke upon conversion of methanol to olefines on zeolites, thus the use of a UV-Raman setup was compulsory to avoid the strong emission of the coke species.[7] Since the risk of laser-induced damage is highly probable in these conditions, the sample was moved during the measurement by exploiting bed fluidization: the continuous exchange of the catalyst particles under the beam avoids their decomposition due to the laser. The fluidization is achieved in this device by a combination of fast gas flow through the catalytic bed and electromagnetic shaking of the whole reactor. The results achieved with this setup were really satisfactory, since also strong UV absorber like Polycyclic Aromatic Hydrocarbons (PAHs) can be effectively measured avoiding any type of damage.[7] This point is really important in the study of coke formation of zeolites, since the sample preservation makes sure that the carbonaceous species observed originate from the reaction and not from spurious, laser induced sample damaging.

The more recent example of Raman setup with movable sample is due to Beato and coworkers, realized by modifying a commercial Linkam CCR1000 reactor-cell as shown in Figure 2.5a.[8] This device again exploits the catalytic bed fluidization, but it was realized with a fully fluid-dynamic concept as Figure 2.5b illustrates: the powder is fluidized by backflow pulses with regular frequency, produced by a dedicated device. The versatility of this tool has been demonstrated by application involving several heterogeneous catalysts.[8,9] Despite its excellent capability to preserve the sample from laser-degradation, fluidization is also a possible source of drawbacks: i) unavoidably the sample is partially lost during the experiment, limiting the time framework available to perform it; ii) the continuous friction among the particles leads to their progressive morphological modification, so that occasionally the fluidization

conditions (strongly connected to the particles shape and size) are no longer achievable iii) in presence of condensable vapors, the wetting of the catalyst can prevent the fluidization to occur; and iv) since a gas flow is required to fluidize the powder, the reactor-cell is not suitable for working in batch (*i.e.* static conditions) or in vacuum.

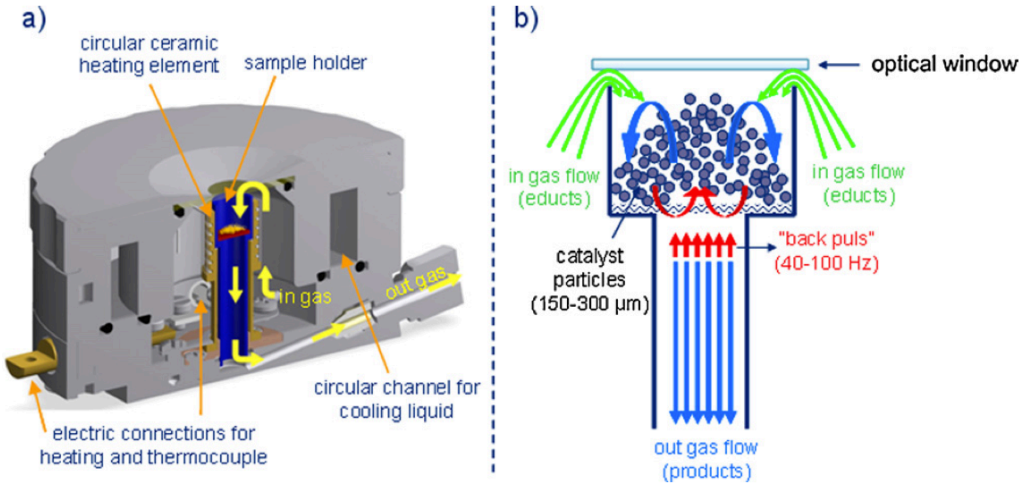

Figure 2.5 a) Scheme of the modified Linkam CCR1000 fluidized bed reactor-cell by Beato and coworkers; b) detail of the fluidization mechanism. Reproduced from Ref. 8.

2.2 Development of a new Raman setup

Analyzing the outcomes from the literature analysis presented in the previous section, it is clear that the development of a Raman setup allowing the sample motion is not a straightforward path. As for every technological implementation, the starting point is to clearly define the requirements for the final object: concerning the goals of this thesis, the cell must allow to perform Raman measurement in controlled atmosphere (vacuum, static and/or flowing gas), to perform thermal treatments and to exploit the maximum laser power thus reducing the measuring time (but avoiding at the same time any sample damage induced by the excitation source). Being the two former requirements easily satisfied by a simple quartz cell coupled with an oven and a gas/vacuum manifold, the latter represent the real technological challenge. According to

the literature, three possible implementations have been attempted to solve this problem: i) the mechanical rotation of the sample in pellet form; ii) the displacement of the measurement spot over the sample; and iii) the exploitation of fluidized bed conditions over powder samples. Because of the blocked construction of the available Raman instrumentation, the second possibility has been immediately neglected. Comparing the remaining two, the mechanical implementation is preferable because technically easier and suitable for every kind of controlled atmosphere, whereas the fluidized bed solution can work only in flow conditions in combination with special devices producing the fluidization. However the sealing drawback becomes limiting for the former, since the driving elements for the sample holder require a connection with the external environment, thus a possible leaking point. The solution to this problem was found by implementing a contactless transmission of the mechanical force: as in a common magnetic stirrer, a rotary movement of the sample holder induced by a rotating magnetic field. The sample holder is the core of the setup, as it contains a permanent magnet which is forced to align to the applied field, thus producing the sample movement. In this way all the mechanical components are placed outside the controlled atmosphere region, which can be now completely separated from the external environment.

At the present implementation the sample holder is realized by a stainless steel hollow cylinder of 6 mm diameter and ~5 mm height. The magnetic element is an AlNiCo-5 cylindrical bar, mounted along the stainless steel cylinder through two holes drilled in its walls: the choice of this magnetic alloy is due to its high Curie temperature (above 800 °C, allowing to perform high temperature activation treatment without losing the magnetization) and to its reasonable magnetic coercivity (about 50 kA m^{-1}). By comparison, a neodymium based magnet can reach 15-20 times higher coercivity values, but it will never be suitable for high temperature applications because of the lower

Curie point (300 °C).[10] On the upper part of the stainless cylinder, a square gold envelop of about 6 mm side is mounted: the envelop is blocked to the cylinder by a gold strip and it is intended to host the sample in form of self-supported pellet. The sample is kept in place by four foldable winglets integrated within the gold envelope. Being the sample integrated in the sample holder, the former rotates together with the latter as the external field is applied. Thanks to its small dimensions, the sample holder can be introduced in different types of cells, however a specific design was developed: the cell and the sample holder are shown in Figure 2.6.

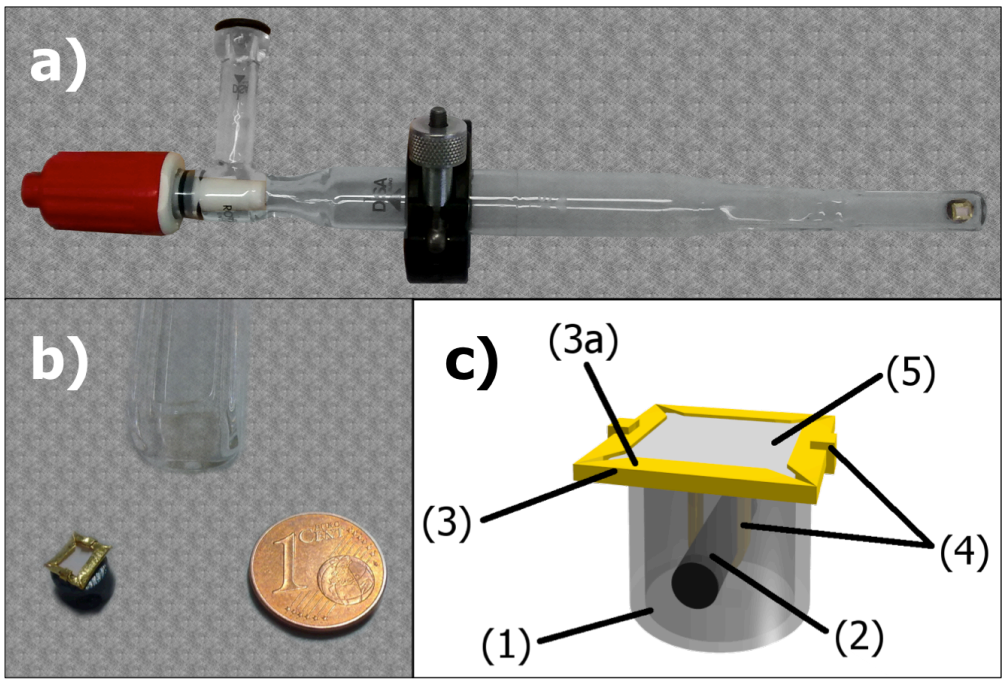

Figure 2.6 Design of the newly developed Raman cell. a) The full mounted cell with the sample positioned in the optical part. b) Detail of the rotating sample holder. c) Construction scheme of rotor: (1) hollow stainless steel cylinder; (2) AlNiCo-5 magnetic element; (3) gold envelope; (3a) foldable winglet of the gold envelope; (4) gold strip fixing the gold envelope, and (5) sample in pellet form.

The cell is actually simple and it can be described as two different blocks: the "body" (containing the optical part) and the "head" (allowing the connection of the cell to a gas manifold. Starting from the description of the body, the

optical part is constituted by a standard 10 mm cuvette of Suprasil quartz, in order to guarantee a good transparency and the absence of fluorescent emission also in the UV spectral region. Such cuvette is welded to a cylindrical tube, realized in quartz glass and thus intended to resist the high temperature the sample should reach during activation. The body is connected to the head through a glass-flanges system, sealed by a Viton O-ring and mechanically kept in place by a clamp. Dismounting the clamp, the cell can be divided in the two parts allowing the introduction of the sample, as well as an accurate cleaning of the device. The head part is terminated by a PTFE tap, separating the glass-flange from a Rotulex type, grease-free connection. The use of a completely grease free setup is of great importance with regard to zeolite samples: zeolites are exceptional adsorbents, so that any possible contaminant coming from the setup should be avoided (specially hydrocarbons as it will be shown in the next chapters). The possible sources of contamination have been reduced to the minimum extent building up a dedicated gas/vacuum manifold as presented in Figure 2.7. The leitmotiv of the construction has been to completely avoid any type of vacuum grease, using instead glass-flange or Rotulex for connections and PTFE-only taps. Also metal parts have been reduced to the minimum extent, preferring the use of glass whenever possible. To further reduce the risk of external contaminations, the volume of the manifold was reduced as much as possible, also facilitating the cleaning of the entire line if necessary. Additionally the whole glass body of the manifold is constantly kept at 150°C to reduce the adsorption of pollutants on the line walls. Finally the vacuum is produced by a turbo pump coupled with a membrane pump, so again not needing any oil or lubricant in the vacuum part.

Upon the construction of the setup, a careful testing of its real functioning has been performed. Among the various test-cases analyzed, the most significant two will be reported here: the characterization of molybdenum

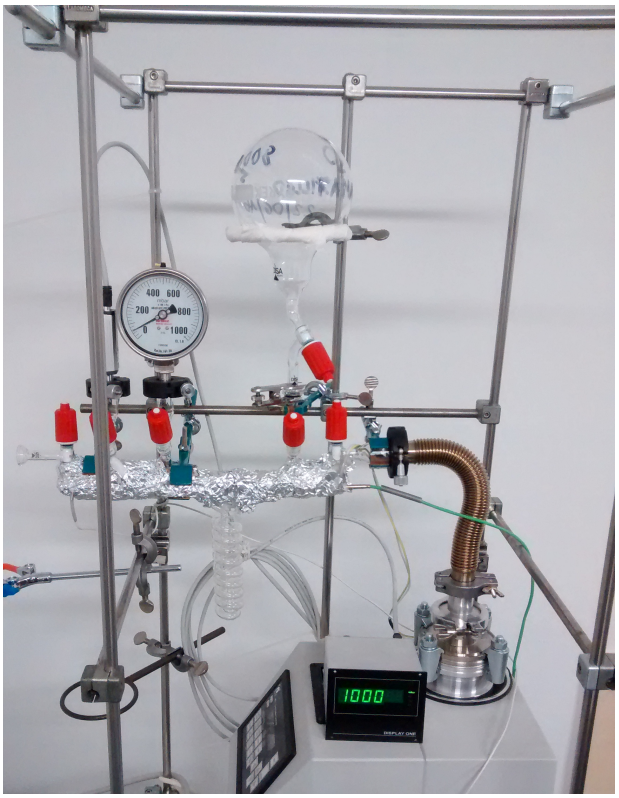

Figure 2.7 Design of the gas manifold dedicated to the Raman setup.

sulfide by visible Raman (Figure 2.8) and the study of methanol adsorption on H-ZSM-5 by UV-Raman (Figure 2.9).

Molybdenum sulfide was chosen as test-case because of its well defined Raman fingerprints: the A_{1g} and the E^1_{2g} vibrational modes give rise to the characteristic doublet of bands observed around 400 cm^{-1}. These signal are sensitive to the material properties and the maxima positions of the two modes have been univocally related to the number of layers constituting the MoS_2 crystal.[9,11,12] Furthermore the strong effect of the temperature on the peaks positions has been quantitatively proven.[13,14] Molybdenum sulfide is then an optimal system to verify the reliability of the new rotating sample setup, since local heating due to the laser should be avoided. The results reported in Figure 2.8 support this statement.

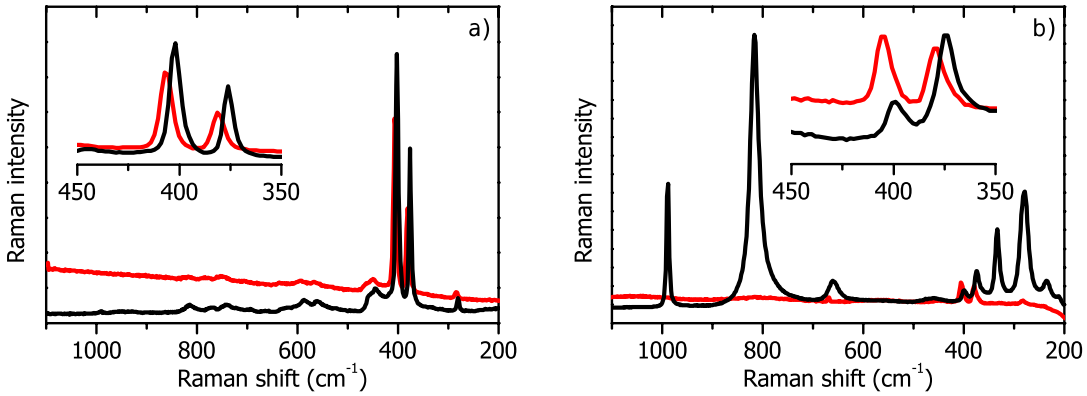

Figure 2.8 Bulk molybdenum sulfide analyzed by Raman spectroscopy while rotating (red lines) or not (black lines) the sample while exploiting full excitation power. Excitation wavelengths: a) 514.5 nm; and b) 442 nm.

The experiment was conducted on a bulk MoS_2 pellet (Fluka): a single spectrum, performed exploiting the maximum laser power, was collected on the sample while rotating or kept in static position. Each collection required ~30 s of exposure to be completed. Two different excitation laser were used, with λ = 514.5 nm (Ar^+ laser) and λ = 442 nm (He-Cd laser), to verify the different behaviors upon the change of wavelength. In the case of 514.5 nm excitation, the collection performed with the sample under rotation gave a spectrum completely in line with the one expected for a bulk MoS_2 at room temperature, showing the A_{1g} and the E^1_{2g} peaks maxima at 407 cm^{-1} and 382 cm^{-1}.[12] Performing the measurement on the static sample, a red-shift of about 5 cm^{-1} is observed: according to the model of Najmaei and coworkers,[13,14] such displacement can be ascribed to a local heating induced by the laser of the order of 300 °C. Even more impressive are the outcomes of the measurement performed with the 442 nm laser: in this case, the suspension of the rotation allows the promotion of a chemical reaction between MoS_2 and atmospheric oxygen to give a molybdenum (VI) oxide (MoO_3) phase, as testified by the growth of its characteristic signals: the intense and sharp bands at 990 cm^{-1} and 820 cm^{-1}, related to ν(Mo=O) and ν(Mo-O-Mo) stretching modes respectively, are the classical fingerprints for the formation of an oxidic Mo phase.[15]

The second example demonstrating the importance (and the reliability) of the sample rotation is presented in Figure 2.9: the study of methanol adsorbed on an acid zeolite (in the example a H-ZSM-5, provided by Süd Chemie, Si/Al = 45). This test case is relevant in the framework of this thesis, since the capability to perform methanol adsorption on zeolites without observing laser induced decomposition represents the starting point for the study of the Methanol-To-Hydrocarbons process (MTH) by Raman spectroscopy. Since the reaction is expected to produce highly fluorescent deactivation products, the use of UV-Raman is compulsory, thus also the preliminary tests were performed exploiting such configuration. In detail, a frequency doubled Ar^+ laser emitting at 244 nm was the excitation source for the experiment.

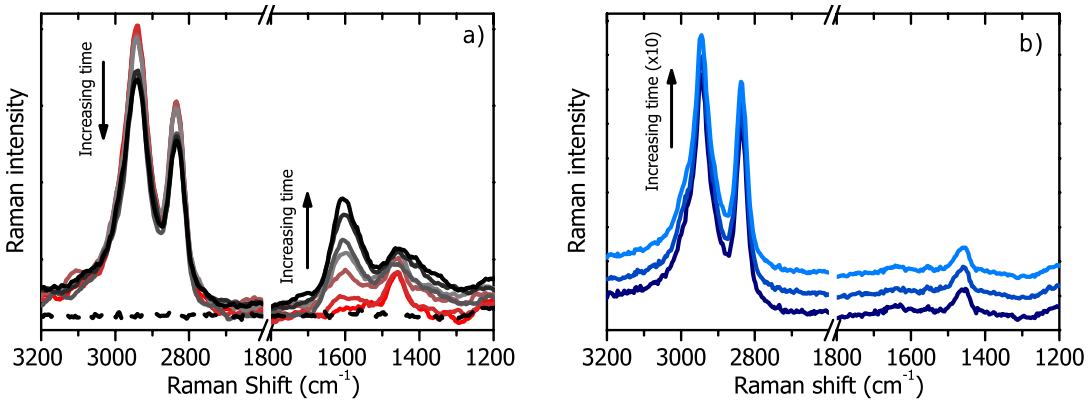

Figure 2.9 UV-Raman (λ =244 nm) of methanol adsorbed on an activated H-ZSM-5 measured: a) with static sample; b) rotating the sample. The accumulation time for each spectrum in panel b) is 10 times longer than for spectra in panel a). Spectra in panel b) have been vertically shifted for sake of clarity.

The experiment was conducted by activating the zeolite (evacuation at 500 °C for 60 min, followed by further 60 min under 100 mbar of pure O_2) and then contacting it with the vapor pressure of methanol (about 130 mbar at room temperature). As the sample was measured in static conditions the signal of methanol progressively decreased along consecutive spectra (accumulation

time ~90 s each), while a new feature grown at 1600 cm^{-1}: the latter is the classical fingerprint of carbonaceous species, indeed ascribable to the methanol decomposition induced by the UV laser. Conversely the rotation is effective in preventing such kind of damage: the spectra shown in Figure 2.9b testify the stability of the adsorbed methanol over a time lapse much longer (about 18 min per spectrum) than the one explored in Figure 2.9a.

The presented setup represents the first working prototype of a new cell for applications in Raman spectroscopy. However its possibilities are still limited with respect to some of the solutions shown in the literature:[3,6,8] in particular the measurements can be conducted only at room temperature and in batch/vacuum conditions, limiting its field of applicability. The cell was then further developed following two separate paths: i) the construction of an *in situ* heating system which can be lodged inside the instrument while measuring; and ii) the realization of a new cell for flow experiments, including its specific heating system. The two setups are displayed in Figure 2.10.

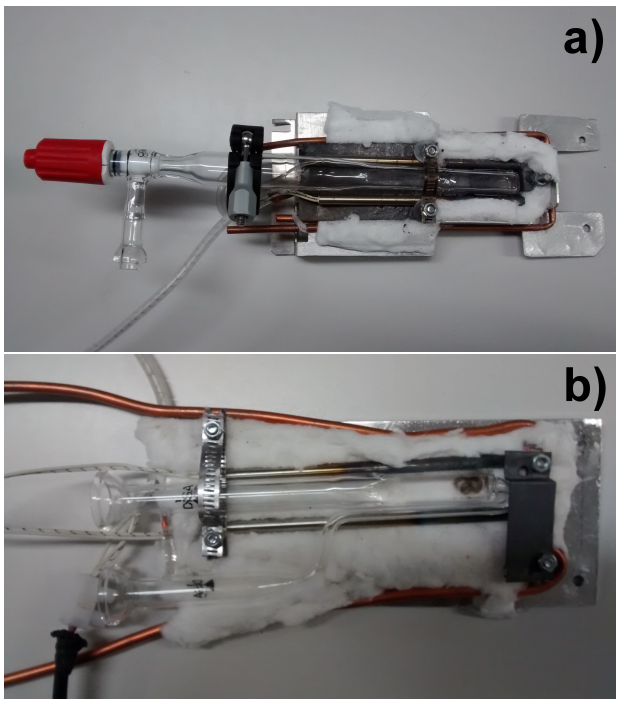

Figure 2.10 In the a) part, the *in situ* heated setup. In the b) part, the flow cell setup with its heating system. In both cases, the top insulation was removed to show the design of devices.

These last developments open to the possibility to perform more complex studies by Raman spectroscopy: they were in particular exploited in the study of the MTH reaction as it will be shown in Chapter 3. However, also for simpler and/or routine experiments sample rotation is now always exploited, guaranteeing the reliability of the Raman results while reducing the time cost to obtain them.Because of the promising results obtained through the setup and taking into account its relatively low cost, a patent request was presented to the Italian Patent Office:[16] at present time, the request is under review and its international extension is under evaluation.

References

(1) Fan, F.; Feng, Z.; Li, C. UV Raman Spectroscopic Studies on Active Sites and Synthesis Mechanisms of Transition Metal-Containing Microporous and Mesoporous Materials. *Acc. Chem. Res.* **2010**, *43* (3), 378–387.

(2) Kiefer, W.; Bernstein, H. J. Rotating Raman Sample Technique for Colored Crystal Powders; Resonance Raman Effect in Solid $KMnO_4$. *Appl. Spectrosc.* **1971**, *25* (6), 609–613.

(3) Cheng, C. P.; Ludowise, J. D.; Schrader, G. L. Controlled-Atmosphere Rotating Cell for in Situ Studies of Catalysts Using Laser Raman Spectroscopy. *Appl. Spectrosc.* **1980**, *34* (2), 146–150.

(4) Müller, A.; Weber, T. In Situ Raman Investigation of Hydrodesulphurization Catalysts. *Appl. Catal.* **1991**, *77* (2), 243–250.

(5) Bañares, M. A. Operando Methodology: Combination of in Situ Spectroscopy and Simultaneous Activity Measurements under Catalytic Reaction Conditions. *Catal. Today* **2005**, *100* (1–2), 71–77.

(6) Chua, Y.; Stair, P. C. A Novel Fluidized Bed Technique for Measuring UV Raman Spectra of Catalysts and Adsorbates. *J. Catal.* **2000**, *196* (1), 66–72.

(7) Chua, Y. T.; Stair, P. C. An Ultraviolet Raman Spectroscopic Study of

Coke Formation in Methanol to Hydrocarbons Conversion over Zeolite H-MFI. *J. Catal.* **2003**, *213* (1), 39–46.

(8) Beato, P.; Schachtl, E.; Barbera, K.; Bonino, F.; Bordiga, S. Operando Raman Spectroscopy Applying Novel Fluidized Bed Micro-Reactor Technology. *Catal. Today* **2013**, *205* (0), 128–133.

(9) Signorile, M.; Damin, A.; Budnyk, A.; Lamberti, C.; Puig-Molina, A.; Beato, P.; Bordiga, S. MoS_2 Supported on P25 Titania: A Model System for the Activation of a HDS Catalyst. *J. Catal.* **2015**, *328*, 225–235.

(10) Cullity, B. D.; Graham, C. D. Hard Magnetic Materials. In *Introduction to Magnetic Materials*; John Wiley & Sons, Inc.: Hoboken, NJ, USA, **2008**; pp 477–504.

(11) Lee, C.; Yan, H.; Brus, L. E.; Heinz, T. F.; Hone, J.; Ryu, S. Anomalous Lattice Vibrations of Single- and Few-Layer MoS_2. *ACS Nano* **2010**, *4* (5), 2695–2700.

(12) Li, H.; Zhang, Q.; Yap, C. C. R.; Tay, B. K.; Edwin, T. H. T.; Olivier, A.; Baillargeat, D. From Bulk to Monolayer MoS_2: Evolution of Raman Scattering. *Adv. Funct. Mater.* **2012**, *22* (7), 1385–1390.

(13) Najmaei, S.; Liu, Z.; Ajayan, P. M.; Lou, J. Thermal Effects on the Characteristic Raman Spectrum of Molybdenum Disulfide (MoS_2) of Varying Thicknesses. *Appl. Phys. Lett.* **2012**, *100* (1).

(14) Najmaei, S.; Ajayan, P. M.; Lou, J. Quantitative Analysis of the Temperature Dependency in Raman Active Vibrational Modes of Molybdenum Disulfide Atomic Layers. *Nanoscale* **2013**, *5* (20), 9758–9763.

(15) Dieterle, M.; Mestl, G. Raman Spectroscopy of Molybdenum Oxides. *Phys. Chem. Chem. Phys.* **2002**, *4* (5), 822–826.

(16) Damin, A.; Signorile, M.; Bonino, F.; Bordiga, S.; Disa, R. Cella per Analisi Mediante Spettroscopia Raman. *102015000069819*, **2015**.

Chapter 3

Conversion of methanol over acid zeolites: deactivation paths of the Methanol To Hydrocarbons reaction

The increasingly request of renewable energy sources is one of the most serious challenges humanity should face in the next decades: in particular, new ways toward liquid hydrocarbon production have to be found, since these represents the most versatile/easily transportable energy sources available nowadays.[1] Furthermore, simple hydrocarbons (such as low olefins) represent some of the most demanded chemical goods, being the fundamental building blocks for a variety of chemical processes.[2] A possible preparation route for hydrocarbon (and in particular light olefins) from potentially renewable sources is represented by the Methanol To Hydrocarbons (MTH) process: methanol is converted at relatively high temperatures (usually in the 300-500 °C range) on an acid heterogeneous catalyst (a zeolite in its protonic form) yielding mainly hydrocarbons in the C_1-C_{11} composition range.[3–6] Zeolites are really convenient catalysts in this reaction because of their intrinsic shape selectivity and optimal acidity: playing on the type of porosity, morphology and the strength of acid sites the MTH reaction can be finely tuned toward the production of the desired chemicals.[7–17] Apart from these positive features, zeolites can be regarded simultaneously as the bottleneck for a wide implementation of such process and, again, their exceptional shape selectivity is the main reason: if bulk species are produced in the zeolite pores/channels, their diffusion outside the porous system can be extremely difficult or even impossible by steric hindrance (the so called "ship-in-a-bottle" effect). Another drawback related to the porosity is the external blocking of pores due to accumulation of bulk molecules on the outer surface of the zeolite particle. The combination of

these processes, generally referred as coking, is the typical deactivation path for zeolite catalysts in the MTH reaction. The extent of the coke formation is regulated by several factors, being the most important among them: i) the diffusive properties of the catalyst, strictly related to the topology of the zeolitic framework and to the morphology of the particles;[9,11,18–21] ii) the density of active sites, related to aluminum content of the zeolite;[22–24] iii) the strength of the acid sites;[7,10,25] and iv) the reaction conditions (temperature, pressure, reactant supply).[26,27] Without entering in deep details for each point, it is clear that coking in MTH catalysts is a complex topic driven by many variables, which effects should be considered separately in order to univocally understand the deactivation process.

Traditionally the study of deactivation of zeolites in the MTH process is based on the *a posteriori* study of the coke: parameters such as coke amount, composition and location with respect to the catalyst are the most relevant in this kind of approach. Usually a combination of techniques is requested to obtain a complete picture on the nature of coke: thermogravimetry can easily give the total amount of coke, volumetry could be helpful in locating the coke formation, coke dissolution followed by GC analysis will give a compositional picture of the lightest fractions, *etc*. A rich example of this kind of analysis is represented by the submitted paper attached to this thesis as Appendix C. An alternative pathway, which application is still limited with respect to the previous, is represented by the spectroscopic characterization of coke; though this kind of approach is generally more complex than the previous, it also owns a number of advantages: it is not destructive, depending on the selected technique a different piece of information can be obtained, with proper experimental design it can be applied directly *in situ* thus giving a more realistic picture. In this panorama, Raman spectroscopy is an excellent tool for the characterization of deactivation products of MTH, exploiting its positive features toward the characterization of carbonaceous materials.[28,29] However

the application of Raman is somehow limited by the presence of fluorescent compounds found as common components of the molecular fraction of coke: this fact immediately excludes the possibility to characterize a coked zeolite by conventional visible Raman. As already commented in Chapter 1, the most suitable solution to this drawback is to exploit UV-Raman (since most of the molecules are not emissive in this spectral region): this is one of the most effective approaches, as also testified by the (few) pioneering studies of MTH reaction by Raman.[30–32]

Being the MTH a complex process, before to begin the study of the reaction, a set of data was collected on its separated actors, in detail: i) a set of supposed deactivation products, belonging to the class of Polycyclic Aromatic Hydrocarbons (PAHs), was characterized with the aim to measure them in conditions similar to ones experienced by a real coke species; ii) the activation procedure of the catalyst (specifically H-ZSM-5) was deeply investigated, since a complete depletion of pre-existing coke-like species is needed in order to properly characterize the reaction coke.

3.1 Experimental

As introduced in Chapter 1, the study of zeolites is strongly affected by the emission signals of adsorbed species. These contributions turn to be dominant in the case of acid zeolites, since their superior capability to interact with hydrocarbons. Furthermore, upon reaction with methanol, many strongly fluorescent species are formed: as an example PAHs (which are the main components of molecular-type coke) exhibit peculiar emission feature, in fact they are exploited as reference compounds in fluorescence spectroscopy. Thereby the collection of Raman is complex in such samples: the most suitable solution is to "move out" of the typical emission region (*i.e.* the visible), *e.g.* by exploiting UV excitation sources. NIR excitation was exploited only within preliminarly studies: even if fluorescence can be (often) avoided, only

concentrated species can be effectively analyzed (see *e.g.* the application on pure PAHs reported in the paper attached as Appendix A to this thesis), since it doesn't allow to exploit resonance conditions. Because of this, all the Raman reported in this chapter were collected with an UV-Raman setup. In detail, measurements were collected with a Renishaw inVia Raman Microscope spectrometer, equipped with 3600 line/mm grating and UV enhanced CCD detector. The excitation source was a Coherent MotoFred 300C frequency doubled Ar^+ laser, emitting at 244 nm. This wavelength, falling in the mid-UV, is sufficiently far from the typical emission region for most materials and molecules, indeed suitable for a Raman investigation on highly fluorescent samples.

A critical point in the data analysis from this study is represented by the correct evaluation of intensities: since the refractive index of the optics is a function of the wavelength, the focal point of the lenses for visible light (used for focusing) and the UV light (exploited in the measurements) is completely different. This means that a certain vertical displacement must be imposed to the sample in order to obtain the correct magnification. This displacement has to be optimized on the basis of the UV-Raman signal, in order to find out the best working conditions: such procedure is rather easy in the case of a "static" sample, whereas it turns to be challenging in the case of a sample in movement. Furthermore, even if the position has been originally optimized, because of the continuous variation of the sample position under the beam it is possible that the focus position is lost along the measurement time. This means that, in principle, the focusing procedure should be repeated quite often. This is not possible every time, especially when monitoring *in situ* a process, as the time lost for improving the focusing could lead to miss important events of the system evolution. A quick and dirty solution to this problem, suitable until reasonable signal-to-noise ratios can be achieved, is represented by spectra normalization. Basically two types of approaches were

adopted in the following: i) a signal, expected to be constant in intensity along the experiment, is chosen as reference; ii) the spectrum is normalized to the most intense band of the spectrum. The former strategy was followed in the case of "clean" samples, where the zeolite features are clearly visible: in particular, the 800 cm^{-1} band (assigned to framework Si-O-Si symmetric stretching modes) was exploited as internal reference. In this way, the change in intensity of independent signals (*e.g.* adsorbed species) keeps absolute value, indeed can be related to their concentration. The latter method was instead compulsory in the case of coked materials: since the first coke species are formed, the signals from the zeolitic framework are overridden, thus impeding the previous normalization strategy. Normalizing to the most intense signal the spectral comparison remains possible in terms of relative intensities, whereas the absolute quantitative information is unluckily lost. An alternative way to solve the normalization problem is the mixing of a known amount of an external component to the sample: if the mixture is sufficiently homogeneous, the Raman signals of this reference material can be exploited for the normalization. The difficult point is the selection of the right reference: such material should present an intense (and simple) Raman spectrum, it must be chemically inert with respect to both the sample and the surrounding chemical environment. The optimal choice for UV-Raman is diamond but, for obvious reasons, this is not routinely suitable. Other materials (*e.g.* silicon) have been tested without bringing to satisfactory results.

3.2 PAHs as coke references for the MTH reaction

Polycyclic aromatic hydrocarbons (PAHs) are a class of molecules mostly originating from the incomplete combustion of organic matter at high temperature, usually regarded as dangerous pollutant because of their mutagenic/carcinogenic activity and their environmental persistence. Concerning heterogeneous catalysis, PAHs originate as byproducts of

petrolchemical processes (*e.g.* MTH), where they lead to a progressive reduction of the catalytic activity: i) by accumulation in the porous system of the zeolite catalyst (indeed lowering the accessibility of active sites to fresh reactants); and ii) being the building blocks for the growth of extended coke species (*i.e.* carbon). The role of such molecules as deactivating agents was first inferred through chromatographic methods: according to the well established Guisnet method, the zeolitic framework is first dissolved in hydrofluoric acid, then the dichloromethane soluble residuals are characterized by GC.[33]

Raman spectroscopy is an optimal alternative tool for PAHs characterization, since these molecules show peculiar vibrational spectra allowing discriminating each other.[34] Furthermore Raman is a non-destructive technique: coked samples can be characterized "as they are", without the needing of any sample pretreatment. In this regard, Raman can be efficiently applied also *in situ*. Because of their strong fluorescence, UV-Raman (or alternatively IR-Raman) is strictly required in PAHs characterization. UV-Raman in particular is convenient, as the electronic transitions of these molecules fall in the 200-400 nm range and resonance conditions can be thus achieved: indeed the sensitivity of Raman spectroscopy toward PAHs increases by orders of magnitude.[34] This means that even in a real catalytic system, where the coke species are highly dispersed (*i.e.* diluted) in the zeolite porous system, PAHs can be characterized exploiting the resonant enhancement. Beside the resonance, the probable photochemical damage of the sample promoted by the intense UV radiation has to be avoided: the tools presented in Chapter 2 find in this type of study an optimal benchmarking opportunity.

According to the dissolution/GC experiment run over several catalysts, the presence of relatively small PAHs (which sizes are in the order of the zeolite channels/cavities ones) as deactivation products is expected.[13] The same studies also showed as deactivation PAHs are often methylated

molecules, as well as the presence of saturated bonds can be find occasionally breaking their aromatic structure: according to this variability, a construction of a complete database of reference molecules requires to take into account hundreds of different species. To limit the (huge) number of possible reference samples, only the progenitor of each PAH (*i.e.* the fully aromatic, unsubstituted molecule) was considered as reference for its whole set of possible variations. The structures of the selected molecules are reported in Figure 3.1.

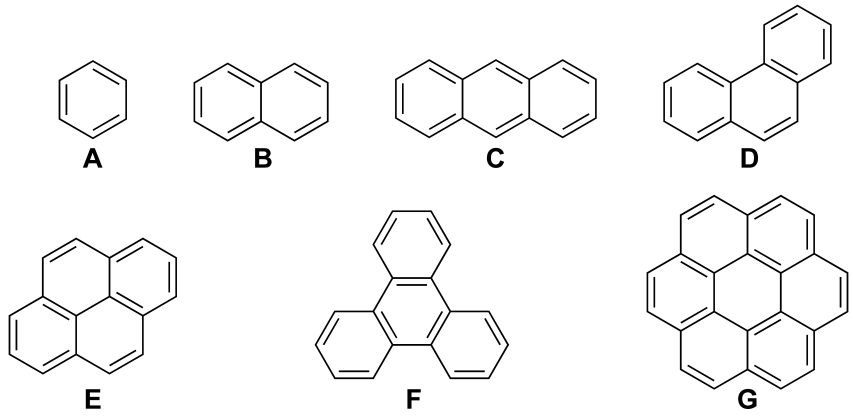

Figure 3.1 Structures of benzene A; naphthalene B; anthracene C; phenanthrene D; pyrene E; triphenylene F; and coronene G.

This is in principle a strong assumption: in order to verify its robustness, the Raman spectra of some differently methylated naphthalenes were simulated by DFT methods. In detail, the spectra were calculated exploiting the Gaussian 09 (D1 revision) code at the B3LYP level, with an Ahlrichs TZV2P as basis set. Dispersive forces were empirically included through the Grimme D3 scheme. All the molecules were geometry relaxed and then frequencies calculations were performed. Raman intensities were computed through a static CPHF scheme as implemented in the code. Resonant Raman spectra were instead simulated through dynamic CPHF: this kind of approach is not the most correct in simulating Resonant Raman, being a vibronic one (*i.e.* based on Frank-Condon and/or Herzberg-Teller theories)

the better way to describe such process.[35] However, taking into account the effect of a given electric field (*i.e.* an excitation wavelength), the variation in the polarization of the analyzed molecules (selected on the basis of the results from methylation of naphthalene over H-ZSM-5)[36] can be evaluated in a more realistic way. The results of both the approaches are reported in Figure 3.2.

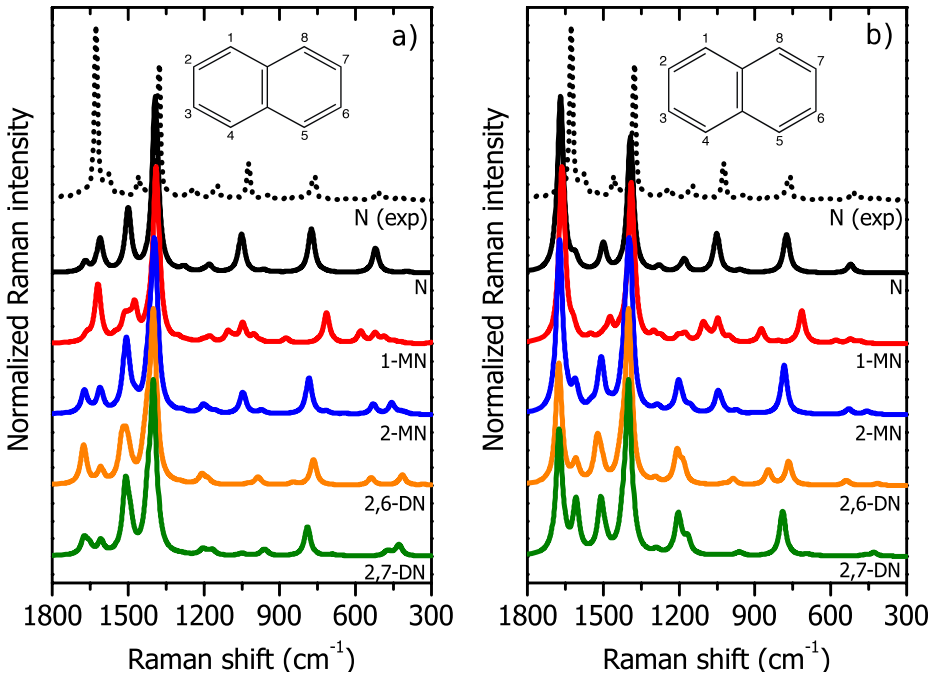

Figure 3.2 Calculated Raman spectra of bare naphthalene (N), 1-methyl-naphthalene (1-MN), 2-methyl-naphthalene (2-MN), 2,6-dimethyl-naphthalene (2,6-DN) and 2,6-dimethyl-naphthalene (2,7-DN) according to a) static CPHF and b) dynamic CPHF simulating 244 nm excitation approaches. The experimental spectrum (λ =244 nm) of naphtahlene (N(exp)) is reported for comparison. The spectra are normalized to the maximum intensity peak.

As demonstrated in both panels of Figure 3.2, a good agreement in terms of frequency is observed for the experimental and calculated spectra of bare naphthalene, testifying the reliability of the computational approach. However a mismatch in relative intensities is achieved with static CPHF approach,[37] as this is representative for totally out-of-resonance conditions only; the dynamic CPHF approach, even being a rough approximation to the description of Raman resonance, is able to give a more realistic result as demonstrated in

Figure 3.2b. Considering now the effect of methylation of naphthalene, simulation demonstrates as the high frequency region (1600-1400 cm^{-1}) is almost unaffected by the insertion of methyl groups in terms of peaks shift. Some variations in the relative intensities of these peaks are observed, however never resulting in a complete quench of the most intense modes. Conversely most of the spectral alterations are seen in the low frequency region (below 1300 cm^{-1}), where each molecule exhibits its vibrational fingerprints as a consequence of the different methylation. Thus the assumption performed on the reference samples selection is demonstrated to be reliable, since methylation effect is in first approximation nil on the main skeletal modes of PAHs (both in terms of frequency and relative intensities).

Since the previous computational data testified the reliability of the proposed compounds in getting insights on the molecular nature of coke, the PAHs reported in were exploited as references in a set of progressive increasingly complexity: only the most important results, as needed for the following discussion on the MTH process studies, are reported here. For further details, the complete set of data is published as a research paper, attached to this thesis as Appendix A. The most significant result of this research work is represented by the characterization of PAHs dispersed from vapor phase (with the exception of triphenylene and coronene, because of their too small sublimation extent, which have been characterized only as pure solids or in solution) on some selected supports mimicking the catalyst in MTH reaction: silica (Aerosil 300), Silicalite-1 (MFI zeolite with Si/Al = ∞) and activated carbon. The first two materials were chosen in order to verify the possible effect of microporosity, being their chemical nature (*i.e.* silicates) fixed. Pure siliceous materials were preferred to more realistic Al containing ones, since the presence of acid sites could in principle catalyze undesired reactions, making impossible the correct characterization of the bare PAHs. Activated carbon was instead included to simulate a heavy coverage of coke, a

challenging situation under the spectroscopic point of view accounting for the high absorption of the support. The results are outlined in Figure 3.3.

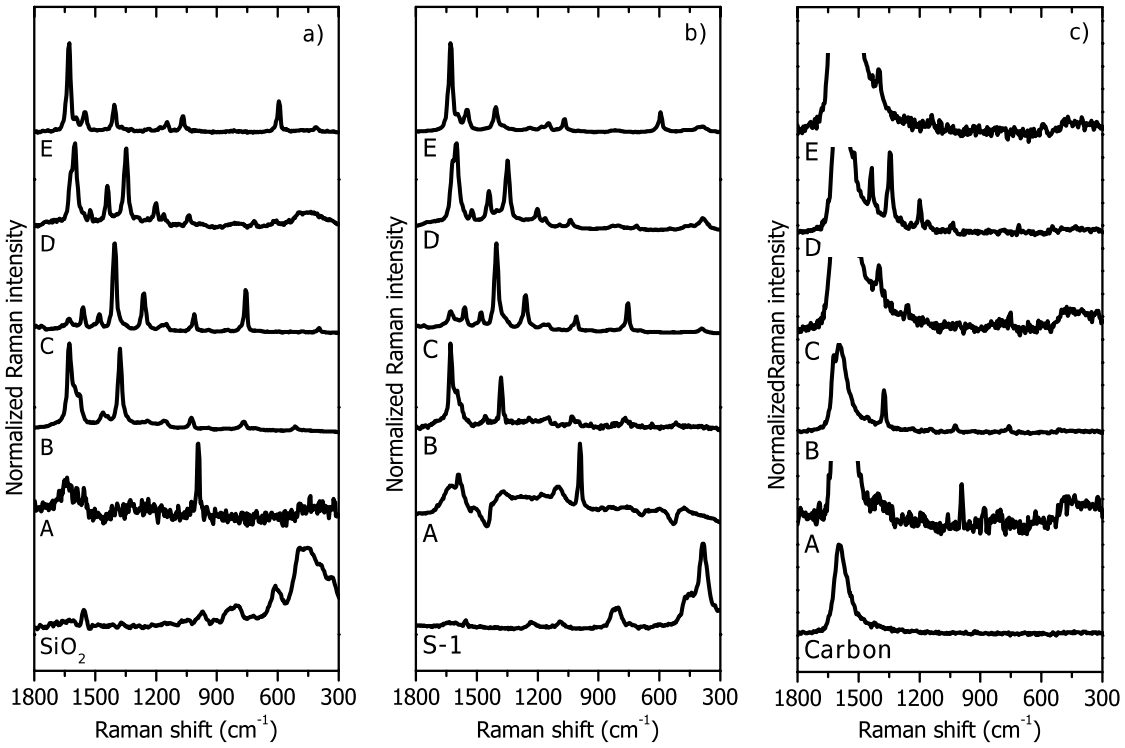

Figure 3.3 UV (λ = 244 nm) Raman spectra of benzene A, naphthalene B, anthracene C, phenanthrene D and pyrene E adsorbed from vapor phase on Silicalite-1 a); Aerosil 300 b); and activated carbon c). The spectra of the adsorption supports spectra are also reported. Spectra have been rescaled and shifted for a better comparison.

The spectra of PAHs were easily obtained on Aerosil 300 and Silicalite-1, being the resonance sufficiently strong to make their Raman signal much bigger than the supports ones. Also on activated carbon the results are completely satisfactory: the main features of each PAHs are clearly distinguishable, even on top of the intense G band of the carbonaceous support. A further interesting feature is related to the peak position according to the different supports: the maxima frequencies are in fact almost constant in the solution, Aerosil 300 and Silicalite-1 data, whereas an average red-shift of 4 cm^{-1} is measured on the main peaks of PAHs supported on carbon. This shift is

probably due to the better interaction PAHs can establish with the structurally similar carbon. Interestingly the signals are instead unperturbed by the microporosity of Silicalite-1: most probably the molecules were unable to diffuse in the porous channel at the experimental conditions, since confinement effects (*i.e.* peaks shifts) are expected from the literature.[38]

The last set of data represent the state-of-art reference for interpreting the formation of molecular coke in MTH process: previous studies only involved the pure molecules or their solutions.[31,34,39] Such approach further allowed to carefully benchmark the potentialities of the newly developed setup presented in Chapter 2: the possibility to measure these photosensitive molecules in a reliable way demonstrates the strength of the device, opening not only to the study of deactivation products in MTH but, in a more general way, to an overall improvement of the applicability of Raman spectroscopy.

3.3 Study on the catalyst activation procedure: the case of ZSM-5

Before entering the study of the MTH process, another important step is the understanding of the correct catalyst preparation, *i.e.* its activation. Industrially this phase is often regarded a secondary importance stage (seen a simple impurities "burn out"), however it is of outmost importance to consider it for fundamental purposes: in fact the presence of preexisting carbon residual can lead to an improper interpretation of data collected during the first steps of MTH, maybe also influencing the reactivity itself. Indeed, a careful characterization on the samples activation has been conducted. As already introduced in Chapter 1, establishing a treatment protocol for zeolites activation is not a straightforward task: summarizing, the diffusion limitation due to the microporosity and the possible undesired side reactions occurring during the process are the main reasons for the failure of samples pretreatment.

The preliminary study presented in the following can be conceptually articulated in three phases: i) the *ex situ* characterization of activation with a vacuum/static gas atmosphere approach; ii) the *in situ* characterization of activation with a vacuum/static gas atmosphere approach; iii) the *in situ* characterization of an industrial-like activation treatment (*i.e.* in gas flow conditions). In order to systematically verify the real efficiency of each approach and to make proper comparisons among them, all the experiments were conducted on the same material: a commercial H-ZSM-5 with Si/Al = 12. This sample was selected according to its low Si/Al ratio, since the large number of active sites is expected to make its complete activation a challenging task. Furthermore this feature can also represent a practical advantage in the study of the proper MTH process: ZSM-5 samples with low Si/Al ratios showed faster reaction kinetics, thus allowing to follow the key stages of the reaction in a reasonable time framework.

Moving to the first point, the goal of this phase was to perform several activation tests, systematically checking the effect of each introduced variation on the final Raman outcome. The optimized activation strategy, giving the better results, will be described here. The proper "in cell" activation was preceded by a pre-calcination step: this had the double function to convert the zeolite from the ammonic (as it is commercialized) to the protonic form and to act as a preliminary cleaning stage (where most of the organic residuals are eliminated). The calcination was performed in static air at 550 °C for 5 h, reaching the final temperature with a 5 °C/min ramp in order to guarantee a sufficiently slow desorption of guest molecules and combustion products. Together with the sample, all the thermally resistant components of the setup in close contact with it (*i.e.* the sample holder, the glass parts of the cell and the cell-vacuum line connectors) were calcined as well. The sample was mounted on the sample holder before calcination (in order to reduce the post-calcination handling time) and the latter was inserted and sealed in the glass

cell after the calcination when all the parts were still quite warm (about 150 °C). All these precautions, reducing the possibility of sample recontamination, allow starting the proper activation in a very clean state. After these initial operations, the real activation treatments were performed: the sample was initially outgassed at RT for few minutes in order to remove air. A heating ramp (5 °C/min) under dynamic vacuum was followed up to 150 °C. After this temperature was reached, it was kept constant for 30 min, still under dynamic vacuum: this stage is intended to remove the larger amount of water possible without reaching temperatures where the acid zeolite can catalyze undesired side reactions. After the outgassing, 100 mbar of O_2 were introduced in the cell and a new ramp (again with a 5 °C/min heating rate) brought the sample/cell to 550 °C. At this temperature, the O_2 was refreshed with a new dose and then left in contact for 1 h. The treatment is concluded by 30 min of outgassing at 550 °C (intended to remove all the combustion residuals) and then by the cooling back to RT. The schematic representation of the strategy, together with the corresponding UV-Raman spectrum, is reported in Figure 3.4.

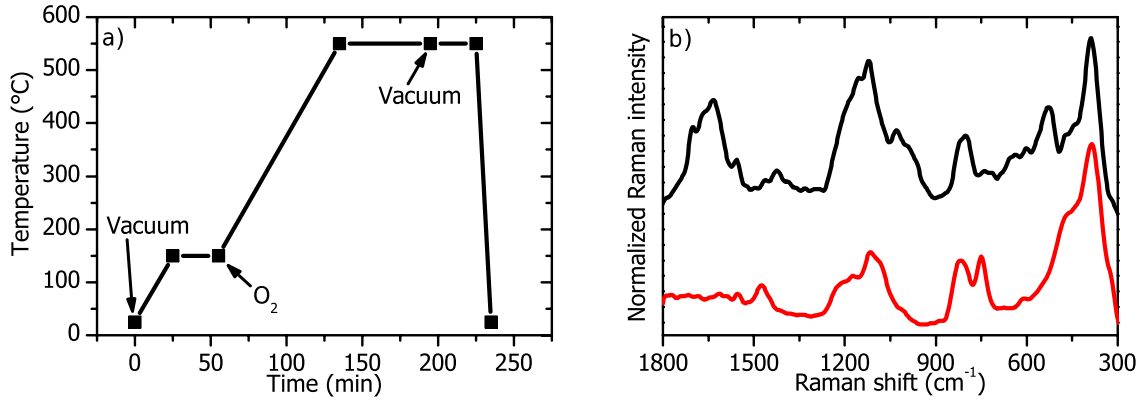

Figure 3.4 a) Schematic representation of the activation procedure; and b) UV-Raman of the bare ZSM-5 (black line) and upon its activation (red line). The spectra have been normalized to the intensity of the 800 cm^{-1} band.

The importance of the activation treatment is depicted in Figure 3.4b: the spectrum of ZSM-5 collected on the bare sample looks in fact more complex than expected. The presence of spurious signals can be generically attributed to adsorbed pollutants: a clear evidence of this is the complex band growing above 1600 cm^{-1}, with a broad extension toward higher frequencies, testifying the existence of several organic moieties (in this region the C=C and C=O stretching modes are present). Other features originating from adsorbates are the broad signal with maximum around 1100 cm^{-1} (too intense to belong to a Si-O-Si stretching as expected for a silicate) and the sharper peak just above 500 cm^{-1}. Upon activation, all these vibrations completely disappears, leaving intact the well documented Raman features of the ZSM-5:[40–42] the spectrum shows the intense and sharp peak at about 380 cm^{-1}, a peculiar fingerprint of ZSM-5 assigned to the 5-members rings typical of its structure, whereas the wide shoulder extending at higher frequencies is attributed to the vibrational modes involving the other ring structures (10-, 6- and 4- member rings). Concerning the Si-O-Si stretching regions, both the asymmetric (around 1200 cm^{-1}) and symmetric (800 cm^{-1}) modes are observed. Close to the latter band, instead, an undocumented feature is observed at 745 cm^{-1}.

Interestingly, the careful *ex situ* study conducted with the main purpose to optimize the activation procedure revealed a new vibrational feature of the material, not observable in samples measure in air and indeed never commented in the literature. Because of the novelty of such outcome, a deeper investigation was conducted in order to clarify its origin. The complete study is attached as Appendix B, whereas its key steps are presented in the following. The first clue on the nature of the vibrational mode was its relation with the level of "cleanness" of the sample: since it could be observed only upon activation, it is possible to ascribe to a moiety easily affected by adsorption of molecules. The most probable site is thus the Brønsted proton. In order to demonstrate this guess, the first trial was to check if a quantitative

relation exists between the intensity of the 745 cm^{-1} peak and the sample concentration of Brønsted sites (*i.e.* in first approximation to its Al content): a set of five H-ZSM-5, with Si/Al ratio ranging from 140 to 12, were investigated. Furthermore, since the Brønsted proton can be easily exchanged, it was intentionally replaced by some selected cations: sodium (from liquid phase ion-exchange procedure), ammonium (form gas phase treatment of the protonic zeolite) and deuterium (from vapor phase exchange with D_2O) ions were introduced. The structural change in the local environment of the Brønsted site resulting from these substitutions was exploited as a "probe" of the vibrational mode, allowing to make some preliminary hypothesis concerning about its origin. All the exchange experiment were performed on the lower Si/Al ZSM-5 sample, in order to exalt the effects of substitution. The set of results is summarized in Figure 3.5.

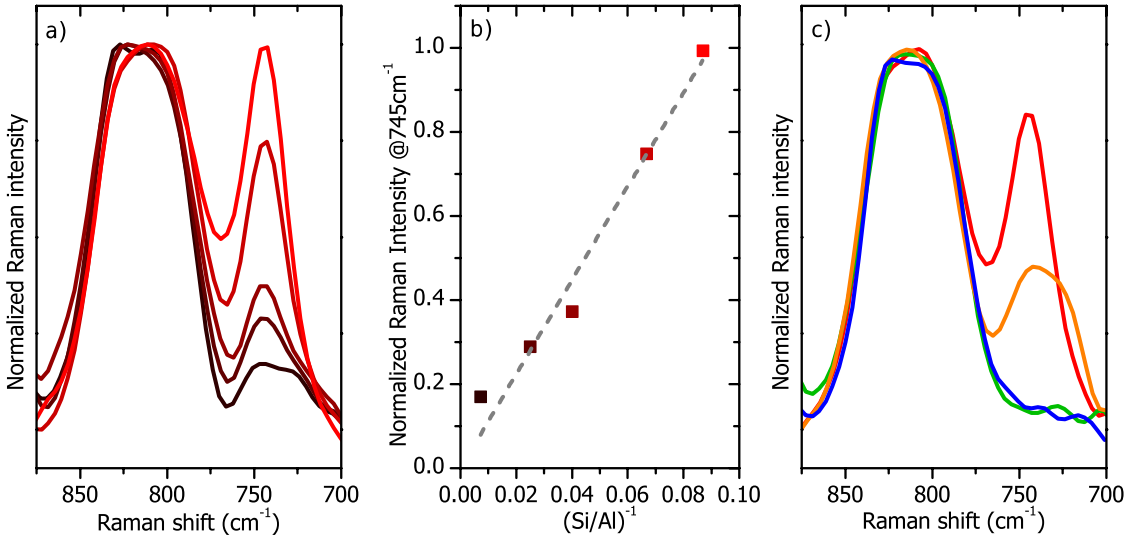

Figure 3.5 a) UV-Raman spectra of H-ZSM-5 with increasing Si/Al ratio (from red to brown); b) 745 cm^{-1} band intensity *vs* the inverse of Si/Al ratio; c) H-ZSM-5 (Si/Al = 12, red line) exchanged by ammonium (green line), sodium (blue line) and (partially) by deuterium (orange line) ions. All the spectra have been normalized to the intensity of the 800 cm^{-1} band.

Very interestingly the intensity of the band at 745 cm^{-1} univocally correlates with the Al content (the larger this, the higher the intensity): further, as shown

in panel b of Figure 3.5, the intensity / Al-content relation is almost linear in the whole compositional range. This first insight demonstrates the relation between the 745 cm^{-1} signal and the concentration of Al, however it does not shed light on the exact Al moiety (*e.g.* Brønsted proton or extraframework Al) giving rise to the vibration. The more sophisticated approach offered by the ion exchange experiments allowed to get further insights on the origin of the vibration: as the proton is replaced by the heavier Na^+ or is bound by NH_3 (thus forming NH_4^+) the band is completely eroded, in agreement with an assignment of the mode to the Brønsted moiety. Even more informative is the (partial) deuteration obtained with D_2O: as expected by the substitution of the proton with the heavier D^+, the 745 cm^{-1} peak clearly exhibits a red-shifted shoulder, which maximum displacement is estimated to be around -20 cm^{-1}. Even if the exact assignment of the mode is arduous without the support of modeling, some preliminary considerations can be stated on the basis of the isotopic substitution results through a comparison with well-known systems and a simple prediction of the shift based on the harmonic approximation of the vibrational mode. Indeed, considering as a rough model the vibrational modes of isolated surface silanols on fumed silica, upon deuterium exchange the Si-OH stretching (*i.e.* the stretching of the Si-O bond, being the proton rigidly held by the oxygen atom) mode experimentally shows a similar shift (-13 cm^{-1}), while a Si-O-H bending is subjected to an approximately ten times larger displacement.[43] Even bigger red-shifts, about 1000 cm^{-1}, are expected for O-H stretchings. Such difference is ascribable to the different weight of the proton in the normal coordinate associated to these vibrations, much smaller in the Si-OH stretching case. Also the shift computed through the harmonic approximation (-17 cm^{-1} upon deuteration) supports this assumption. This observation suggests that the 745 cm^{-1} mode could be ascribed to Si-O-Al bridge stretching mode (also considering its energy, close to the one of Si-O-Si symmetric stretching vibrations). The motion of the proton is probably rigidly

driven by the displacement of oxygen, thus with a low contribution to the normal coordinate of the overall vibration in agreement with the experimental results.

As final check for the assignment, the response of the 745 cm^{-1} band to a reversible and to an irreversible modification of the Brønsted site was considered: the Temperature Programmed Desorption of ammonia (NH_3-TPD) and the progressive dealumination by steaming-like treatments were tested. Only the latter will be discussed here: the characterization of dealumination was chosen since the Al leaching in out of framework position can't be re-incorporated in the framework, leading to a diminishing of the Brønsted sites concentration. This occurrence causes a permanent reduction of the catalytic performances in acid zeolites, thus its understanding is of outmost importance also regarding the practical/industrial applications of zeolites. In order to cause dealumination, a steaming-like treatment was adopted: after the activation, the sample was contacted with the vapor pressure of water (~30 mbar at RT) and then heated in this wet environment up to the desired temperature. Since dealumination is expected to occur as side effect in petrolchemical reaction (where water is often found as byproduct), two temperatures representative for the most relevant industrial processes were chosen: 350 °C and 450 °C. After 30 min of contact at the given temperature, the excess water was outgassed and the temperature rose up to 550 °C in order to re-activate the material. The results are reported in Figure 3.6.

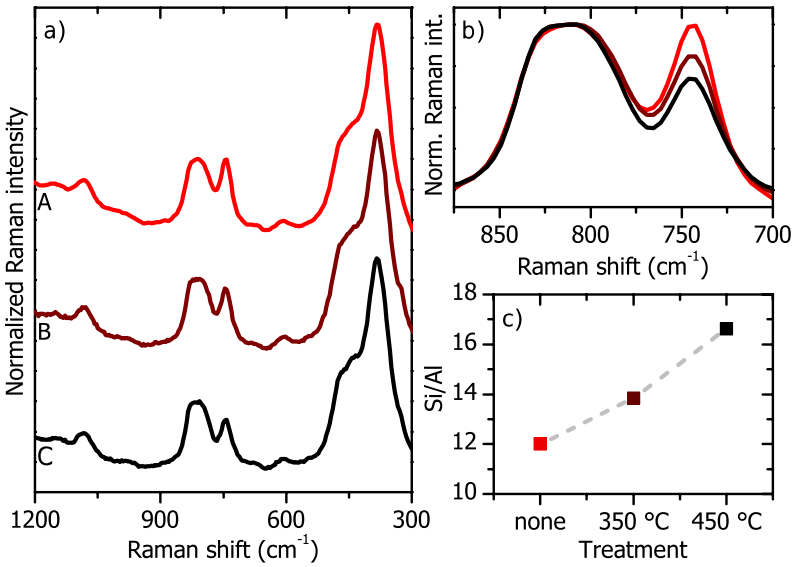

Figure 3.6 a) UV-Raman spectra of H-ZSM-5 (Si/Al = 12): A, activated; B, treated in H_2O at 350°C and reactivated; and C, treated in H_2O 450°C and reactivated. b) Detail of the 745 cm^{-1} band. c) Si/Al ratios upon delaumination treatments, calculated according to the calibration shown in Figure 3.5. All the spectra have been normalized to the intensity of the 800 cm^{-1} band.

The results of dealumination are clearly seen, as the reduced intensity of the 745 cm^{-1} band demonstrates. As obviously expected, the higher the temperature, the larger the dealumination extent (the reduction of the framework Al is about -25% after dealumination at 450 °C). This last experiment also represent a proof-of-concepts toward one of the most relevant thematic in the acid zeolite field: dealumination is in fact the irreversible cause for total deactivation of zeolite catalysts, thus its study is of wide interest. The quantitative nature of the proposed UV-Raman approach can clearly depict the speciation of the Al sites in steamed zeolites whereas most of the techniques fail. By comparison, FTIR is not easily suitable for quantitative considerations on dealumination, since the typical fingerprints for this process fall in the 3800-3600 cm^{-1} region: because of the strong scattering of zeolites in this wavenumbers range, the transmittance is usually poor (below 10%) and close to the detector saturation limit, thus limiting the quantitative meaning of the recorded intensities. Conversely by Raman, thanks to the low scattering power of silicates, the measure can give a more accurate

result, not biased by instrumental limits. Exploiting the calibration curve as reported in Figure 3.5, the Si/Al relative to framework Al upon dealumination treatments have been computed. Thus UV-Raman can be regarded as a potential analytic method for the quantitative speciation of Al in acid zeolites.

The natural evolution of this study has been the implementation of the *in situ* setup, allowing to perform the measurement at a given temperature (*i.e.* while activating the sample). Exploiting the new tool presented in Chapter 2, the activation procedure previously proposed was followed *in situ*. A spectrum was collected at each important point of the activation (*e.g.* vacuum/O_2 switch), as well as each 100 °C during the heating ramps. The findings of this first *in situ* experiment are depicted in Figure 3.7.

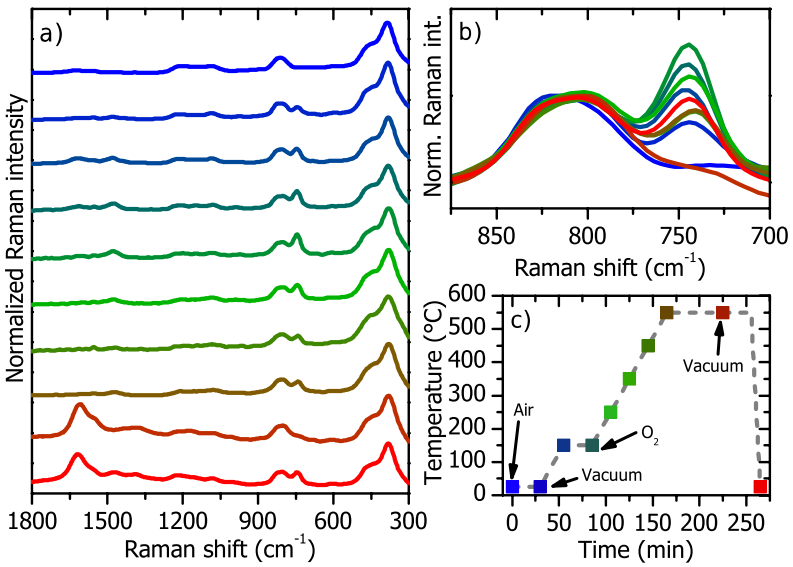

Figure 3.7 a) Sequence of UV-Raman spectra collected during the activation of H-ZSM-5 (Si/Al = 12), from top: RT in vacuum; 150 °C in vacuum, 150 °C in O_2; 250 °C in O_2; 350 °C in O_2; 450 °C in O_2; 550 °C in O_2; 550 °C in vacuum; RT in vacuum (after activation). b) Detail of the 745 cm^{-1} band. c) Schematic of the activation treatment: each node corresponds to the collection of a UV-Raman spectrum. All the spectra have been normalized to the intensity of the 800 cm^{-1} band.

The possibility to collect the spectra during the sample treatment allowed to get new interesting insight on the activation steps: first of all (since the sample is clean thanks to the pre-calcination step) also the mild outgassing at RT is sufficient to make free a fraction of Brønsted protons, as testified by the comparison of the 745 cm^{-1} peak. Later on, a progressive increase in the intensity of such band is observed up to 250°C, independently from the treatment atmosphere (vacuum or O_2). Above this temperature, a progressive reduction of the intensity at 745 cm^{-1} is recorded since the sample is kept under O_2, whereas it readily turns to zero as pressure is reduced to conclude the high temperature step of the activation. The two regimes can be discussed separately: in the first case, the reduction is apparently nonsense, as the treatment condition should univocally promote the elimination of molecules interacting with the Brønsted site (*i.e.* leading to the suppression of the relative Raman feature). Then, since O_2 pressure is present in the cell, a re-adsorption process is really unlike to occur. The reduction in intensity can be then ascribed to a material property: the proton mobility. From both experimental[44] and computational[45] literature, the transfer of Brønsted protons in H-ZSM-5 is likely to occur above 200 °C, where the energy barriers can be easily overcome. It is thus reasonable to infer that the proton mobility reduces the intensity of the 745 cm^{-1} band, through a mechanism based on thermal disorder. However a detailed study is required to completely understand this phenomenon. The complete disappearance of the peak in the last high temperature step (*i.e.* when O_2 is outgassed) can be instead ascribed to a different phenomenon: looking at the 1700 - 1200 cm^{-1} region of the spectrum, a number of new bands has appeared. These signals are univocally ascribable to coke like species, thus testifying a rapid reactivity of the zeolite with some residual hydrocarbons. The most surprising observation following this interpretation (assuming it is correct) is the capability of the zeolite to adsorb hydrocarbons from the cold part of the cell (far at least 10 cm from the

sample) even if it is still at 550 °C and against a pressure gradient produced by the pump. This fact further highlights the challenge beyond the proper activation of zeolites: a confirmation arose from the last spectrum of the series (collected after cooling in vacuum), where the 745 cm^{-1} is observed but, due to the contamination produced by the high temperature vacuum step, its intensity is far lower than as measured at 250 °C in O_2.

3.4 Preliminary study of the MTH reaction: from *ex situ* toward *operando*

As last section of this chapter, some preliminary results on the study of the MTH reaction will be given. In detail, the focus of Raman spectroscopy in this process is the characterization of deactivation products, as previously introduced. The same strategy adopted for the study of H-ZSM-5 activation was followed, following the reaction first *ex situ* (in batch conditions) and then *in situ* (both in batch and continuous flow conditions). Involving the study of a reaction, even more than in the case of activation the outcomes can be substantially different from a realistic situation because of the differences in the adopted conditions. This is very likely for batch experiments, where the exploitation of a static atmosphere rather than a flow is expected to produce significant differences in the final products (and deactivation species). In particular, the products are not continuously removed (as instead occurs in a flow reaction stream), thus the possibility to observe different deactivation paths (driven by the presence of products themself) is quite high. However the study in batch conditions (both *ex* or *in situ*) is of primary importance in the perspective of the setup development, as this type of approach is better suited for fundamental studies.

Moving to the results, the easiest approach is represented by the study of deactivated samples from catalytic tests with a completely *ex situ* method. Even if rather crude, this type of measurements allows to get a clear picture of

the heavier and/or trapped components of coke, whereas the most volatile ones are expected to be progressively depleted along the time as the spent catalysts is removed from the reactor. In detail, this type of study was devoted to investigate the effect of topology on the deactivation path for 5 different framework types: MFI (ZSM-5, Si/Al = 15), BEA (Beta, Si/Al = 17), MOR (Mordenite, Si/Al = 8), TON (ZSM-22, Si/Al = 47) and CHA (SAPO-34, (Al+P)/Si = 11). Each catalyst was analyzed after complete deactivation (*i.e.* after methanol conversion reached 0% on the catalytic test), as well as at intermediate deactivation extents. Part of the following data is included in the submitter paper attached as Appendix C. The related UV-Raman spectra are shown in Figure 3.8, together with the methanol conversion curves for each catalyst. As clearly depicted in Figure 3.8f, the lifetimes of the catalysts are substantially different. Since all the materials shows a similar density of acid sites (with the only exception of ZSM-22), this spread of values can be ascribed in first approximation to the different zeolites topologies: in particular, the main variables to be considered are the pore opening (usually measured in zeolites by the number of tetrahedra forming the pore window) and the dimensionality of the pores network (1-, 2- or 3-Dimensional). The easiest interpretation is that wider the pores facilitates the diffusion of reactants/products, thus increasing the catalyst lifetime. In the same way, the best transport properties, as allowed by a highly branched pore system (*e.g.* a 3D one), improve the catalyst endurance. Moving to the discussion of results, the considered catalysts belong to three different regimes: long lifetime (ZSM-5 and SAPO-34), medium lifetime (Beta) and short lifetime (ZSM-22 and Mordenite). The first class is represented by two catalysts with deep structural differences: in fact, ZSM-5 owns a 3D porous system formed by the intersection of straight and sinusoidal 10 members channel, whereas SAPO-34 is characterized by large cavities connected through 8 members windows in a 3D network.

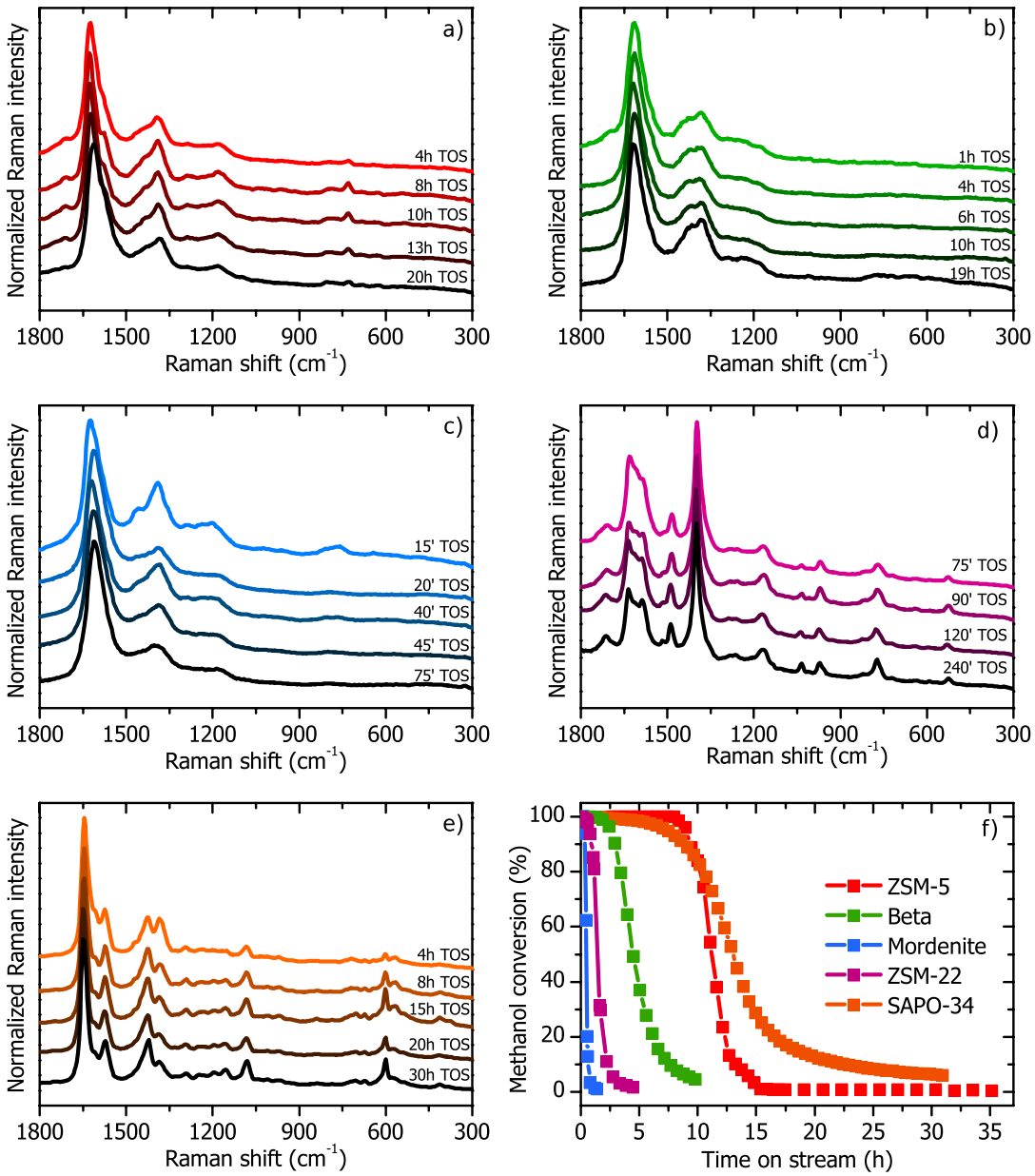

Figure 3.8 UV-Raman spectra of a) ZSM-5, b) Beta, c) Mordenite, d) ZSM-22 and e) SAPO-34 catalyst after different times on stream during the MTH reaction. In part f), the methanol conversion for each catalyst is shown as function of time. The spectra have been normalized to their most intense signal.

The excellent lifetime for the former zeolite is easily explained on the only basis of its topology, since the combination of medium-opening pores and high dimensionality of the channels system leads to optimal transport properties. Less trivial is the discussion on the prolonged lifetime of SAPO-34, which is

expected to experience serious diffusion limitations in relation to its peculiar structure. The main reason for deactivation in this catalyst is the accumulation of bulk molecules in the cages, unable to diffuse and thus to be eliminated (the so called "ship in the bottle" effect). Conversely the formation of external coke is limited, indeed the deactivation occurs only as the bulk molecules are formed and accumulated after a quite long reaction time. The lifetimes of the other three catalysts are instead much shorter: in the case of Beta, despite the wide pores (12 member windows) and the 3D pore structure, the deactivation occurs relatively faster. This short lifetime is possibly related to the typical defective structure of Beta, constituted by the intergrowth of two polymorphs where stacking faults could act as diffusion barriers. Furthermore this specific Beta sample is characterized by a very small particle size, thus many acid sites are available on the outer surfaces, facilitating the formation of bulk coke indeed occluding the pores from the exterior. For the last two catalysts, the fast deactivation is mostly related to the poor diffusive properties according to their 1D pores network: in the case of ZSM-22, the diffusion limitation is worsened by the small opening of the pore mouths (8 members), whereas the Mordenite lifetime is further shortened by its very low Si/Al ratio. Moving to the discussion of the spectroscopic data, the sets of UV-Raman spectra collected for each sample are strongly connected to their topologies as well. ZSM-5 (Figure 3.8a) shows the presence of extended carbonaceous species at every Time On Stream (TOS), but the complex structure of the bands (with maxima, shoulders, *etc*) suggests the presence of molecular moieties. The initial stages of the catalyst lifetime (*i.e.* before the drop in the conversion) are characterized by a progressive increase of the amount of these molecular species, as testified by the growth of some sharp features on top of the smooth profile of bulk coke (*i.e.* D and G bands of carbon).[29] Moving to higher TOS, the following trends of the Raman signals are observed: the shoulder at 1585 cm^{-1} grows in intensity, whereas the intensity of the bands at 1710 cm^{-1},

1390 cm^{-1} and 730 cm^{-1} is progressively reduced. Furthermore, the G band related to bulk carbonaceous species is visibly red-shifted as total deactivation is achieved. The band at 1585 cm^{-1} can be ascribed to the presence of biphenyl moieties, as also testified by secondary features as the small peaks at 1290 cm^{-1} and 1185 cm^{-1}. The band at 1390 cm^{-1} could result from the combination of major features of naphthalene (1380 cm^{-1}) and anthracene (1400 cm^{-1}). The interpretation of the 730 cm^{-1} is not univocal, since the only reasonable molecule an intense mode close to this frequency is fluorene. However, its presence is hardly confirmable as all its main features fall below the G band, furthermore overlapping with the main biphenyl bands. Another possibility is to relate the peak to methylated moieties: as previously demonstrated (see Figure 3.2), methylation mostly determines such soft vibrational modes, constituting the fingerprints for methylated PAHs. Interestingly also a high frequency band is observed at 1710 cm^{-1}, which intensity reduces increasing the reaction time: this mode can be related to a carbonyl stretching, thus inferring the presence of oxygenated compounds as reaction products. According to the increase of the PAHs signals in the early reaction stages, possibly some of the quite large PAHs observed are not deactivating species, whereas they are entering the hydrocarbon pool mechanism[4] as reaction intermediates. The possibility to observe naphthalenes as active moieties was recently recognized on Chabazite catalysts at relatively high reaction temperatures (above 350 °C):[27] since the catalytic test was performed at 400 °C, the active role of naphthalenes in the catalytic cycle can be inferred also for ZSM-5. A similar deactivation pattern arises from the UV-Raman study of the Beta catalyst (Figure 3.8b): in this case, the bulk carbonaceous species are prevailing on the molecular ones, however a sharp maximum can be observed at 1380 cm^{-1}. This signal, assignable to naphthalene, shows a quite constant intensity along the reaction time: most probably the molecular coke is stuck in the zeolite channels as a consequence

of the formation of external carbonaceous bulk species, blocking the pores openings. Also in the case of Mordenite (Figure 3.8c) deactivation by extended carbonaceous species is observed: the main difference with respect to Beta is the presence of clear molecular coke fingerprints just at the very beginning of the reaction, whereas only the D and G bands of bulk carbon are measured after few minutes of reaction. Again, the main molecular species are naphtalenes and anthracenes. A radically different situation is observed for ZSM-22 and SAPO-34: such catalysts, where diffusion limitations are more severe than in the previous cases, are characterized by an almost completely molecular type of deactivating species. In ZSM-22 (Figure 3.8d) the main contributions to the spectrum are ascribable to anthracene (main signal at 1400 cm^{-1}, peak at 1630 cm^{-1}), biphenyl (peak at 1585 cm-^{1} and 1610 cm^{-1}) and fluorene (peaks at 1485 cm^{-1} and 1610 cm^{-1}, in common with biphenyl). Possibly naphthalene (peak at 1630 cm^{-1}, too intense to be only related to anthracene, and shoulder at 1380 cm^{-1}) can be present as well. The spectra are rather similar at each TOS, suggesting that deactivation occurs by molecules accumulations rather than through their transformation in unreactive species along the time. A remarkable presence of oxygenated compounds (carbonyls peak at 1710 cm^{-1}) is constantly detected as well. Finally SAPO-34 (Figure 3.8e) follows a peculiar deactivation path, mainly ascribable to molecules in principle described as reaction products. In fact the most peculiar feature is an intense peak with maximum at 1650 cm^{-1}: the considerably high frequency of such signal, not compatible with the ones typical of condensed aromatics, allows to assign it to the presence of heavy olefins. Considering the low selectivity of such zeotype toward C_{5+} products, it is possible to infer that these products actually are produced in the large cavities of the CHA framework but, because of their large dynamic diameter (especially in the case of branched molecules) they are not able to diffuse out of the pores, behaving definitely as deactivating species. Other contributions

to the spectra clearly assignable are the peak at 1380 cm^{-1}, ascribed to naphthalene, which also follows a clear trend diminishing as TOS increases: as previously inferred for ZSM-5, naphthalenes could enter the hydrocarbon pool as active species at the selected reaction temperature (400 °C), indeed being consumed progressively during the reaction.

The following step in the UV-Raman approach to the MTH reaction was the *ex situ* study of a fully deactivated catalyst through a model reaction performed directly inside the Raman cell. With respect to the previous type of experiment, this way to proceed represents a step back concerning the reaction, since this was conducted in batch, *i.e.* under model conditions. However, since direct control on the reaction can be exploited, a more detailed study on the role of each variable can be performed. Furtherermore, by performing the reaction in batch the exposure of the sample to atmosphere is avoided, then the study of volatile/labile products is possible as well. The preliminary study involved the H-ZSM-5 catalyst, since this is the most important material under an applicative point of view. In order to perform the reaction, the sample was preliminary activated: as the treatment was concluded, instead of bringing the sample back to RT, the temperature was reduced to the desired reaction one (400 °C) while outgassing the sample. The temperature was allowed to stabilize for some minutes, than methanol was dosed (vapor pressure at RT, about 130 mbar) on the activated material, thus starting the reaction. The temperature was kept constant for 30 min after the methanol dosage: after this time lapse, the reaction was rapidly quenched and the sample was finally analyzed by UV-Raman. As last stage of the experiment, the spent catalyst was outgassed at RT for 30 min, in order to remove all the light reaction products and thus providing a detailed picture on the non-volatile coke fraction. The results of this model experiment are given in Figure 3.9.

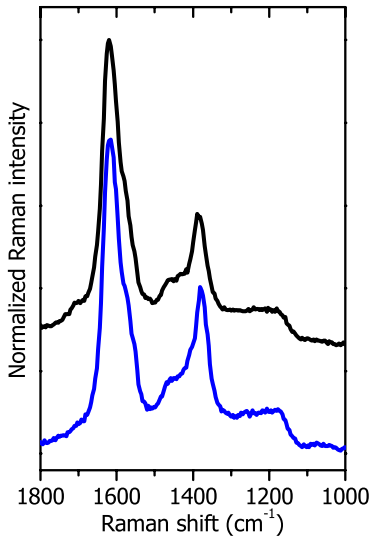

Figure 3.9 UV-Raman spectra of H-ZSM-5 reacted in batch conditions with methanol for 30 min (black line) and outgassed for 30 min after reaction quenching (blue line). Both the spectra have been collected at RT. The spectra have been normalized to their most intense signal.

The conversion of methanol to hydrocarbons occurred as the collected UV-Raman spectra demonstrate. After 30 min of reaction the spectrum is representative of a severely deactivated sample, with clear features from bulk carbon superimposed to sharp/molecular signals. Concerning the latter, the most evident is the narrow peak with maximum at 1380 cm^{-1}: as already commented for the *ex situ* experiment performed on materials from catalytic test, such band can be easily ascribed to the presence of naphthalenes. Interestingly the peak increases in relative intensity (with respect to the main features around 1600 cm^{-1}) upon outgassing: this behavior is of difficult rationalization, as outgassing should remove molecules *i.e.* reducing their signals intensities. Most probably lighter molecules (*e.g.* olefins and/or benzenes), whose Raman signals are weak with respect to naphthalenes (since measured in out of resonance conditions), are eliminated, indeed a larger portion of excitation photons can be efficiently scattered by the resonant naphthalenes. All the other spectral features remain unvaried upon outgassing thus relating them to heavy coke species (*e.g.* large PAHs,

extended carbon). Comparing the spectrum collected upon outgassing with the *ex situ* ones from the same material (see Figure 3.8a), the discrepancy of batch reactivity with respect to proper catalytic tests is observed: this mismatch is probably not involving the deactivation mechanism, since the UV-Raman spectra are rather similar among them. What is totally altered is the kinetic of the reaction: deactivation occurs at much higher rates in the batch reactor, probably as a consequence of the instantaneous dosage of a bulk amount of methanol on a tiny amount of sample. In this way, the reaction space velocity can be approximately considered infinite and after 30 min the sample exhibits the Raman spectrum of a catalyst working for 8-10 h in a standard catalytic test. However the quality of the data obtained, together with the strict control on the reaction variables, makes the *ex situ* batch experiment of fundamental interest.

A step forward in this respect was the *in situ* study of the initial stages of batch reactivity, *i.e.* characterizing the material at reaction conditions (400°C) at short times after the methanol dosage. This kind of experiment requires to achieve a sufficient time resolution, *i.e.* to reduce as much as possible the accumulation time of each spectrum. However the collection should allow to get data of sufficient quality (*i.e.* with reasonable signal-to-noise ratio), thereby useful in the understanding of the early stages of activity. Therefore Raman spectra were collected according to the following methodology: during the first 5 min of reaction Raman spectra were collected continuously (30 s each), then the acquisition time was increased to 5 min and spectra were collected repeatedly up to the desired reaction time. The preliminary results achieved upon this strategy are reproduced in Figure 3.10.

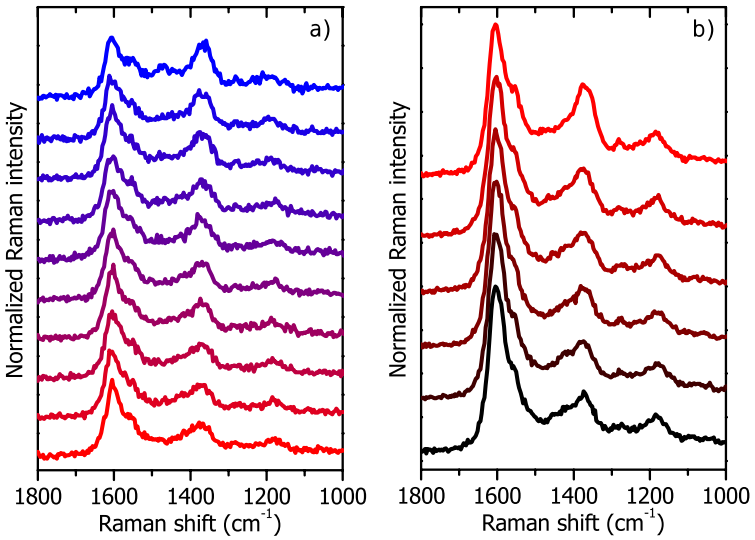

Figure 3.10 UV-Raman spectra of H-ZSM-5 reacting with methanol at 400°C: a) in the 0-5 min time lapse (time evolution from blue to red, 30 s accumulation for each spectrum); and b) in the 5-30 min time lapse (time evolution from red to black, 5 min accumulation for each spectrum). The first spectrum (bright red line) of panel b) represents the sum of the spectra of panel a). The spectra in panel b have been normalized to their most intense signal.

The early stages of deactivation showed a very fast evolution toward the final state as observed in the previous *ex situ* experiment: after 30 s from dosage, the main vibrational signals of coke as collected after 30 min are already recognized univocally. The main difference is represented by the higher intensity of the 1380 cm^{-1} band and a weak but clear maximum around 1450 cm^{-1}: the former indicates that naphthalenes are readily formed upon these conditions, the latter instead can be related to methanol at the catalyst surface. Furthermore, following the time evolution of these peaks along the first 5 min of reaction, their intensity progressively decreases: the methanol feature is completely consumed in the first minute of reaction, whereas the one belonging to naphthalenes reaches a steady-state in 3-4 min. After this time, the UV-Raman spectra are almost unvaried along the following 25 min, testifying the complete deactivation of the catalyst occurred in a very short time in batch conditions. At late reaction stages some other spectral features, not recorded in the *ex situ* experiment, are observed: in particular a clear peak

at 1185 cm^{-1} and a weak signal at 1275 cm^{-1} are present. The former can be related to the presence of phenanthrene, as the low frequency shoulder of the 1600 cm^{-1} peak also allows to infer. The assignment of the latter is less trivial also because of its low spectral quality: methylated benzenes (and especially highly methylated ones, e.g. owning 4 to 6 methyl groups) represent a possible set of candidates, which show their most intense vibrational features close to this frequency.[46,47]

The final section of this chapter is devoted to measurements conducted in realistic conditions: reaction was performed in flow (rather than in batch), with continuous supply of methanol vapors through a stream of inert gas. In order to make a comparison with the *ex situ* experiment with samples from catalytic tests showed before, the same reaction parameters were adopted: methanol was dosed on the catalyst at 400°C (after activation in pure O_2 at the same temperature) at a Weight Hourly Space Velocity (WHSV) of 2 $g_{methanol}$ $g_{catalyst}^{-1}$ h^{-1}. Furthermore the reactivity was evaluated while exploiting two different reactor-cells: the flow setup developed during this thesis (simulating a fix-bed reactor and hereafter referred as spinning pellet cell, see Chapter 2) and the fluid-bed Linkam CCR1000, developed by dr. Beato,[32] were compared. Both the cells (even if on the basis of different principles) are designed to perform *in situ* experiments preserving the sample from the laser beam damaging. For both the studies, a mass spectrometer (MS) was connected to the outlet of the cell, allowing the on-line analysis of reaction products. The following experiments are reasonably labeled as *operando*. As for the previous *in situ* approach, the incipient stages of reactivity were followed by "fast" spectra (30 s each, for the first 5 min), whereas the following hour of reaction was sampled with spectra every 5 min. The results are summarized in Figure 3.11. In both the reactors, as the conversion of methanol begins (set as "time 0" on the MS charts), a little delay (2-3 min) occurs before the selected products are detected. In the Raman spectra this trend is clearly observed:

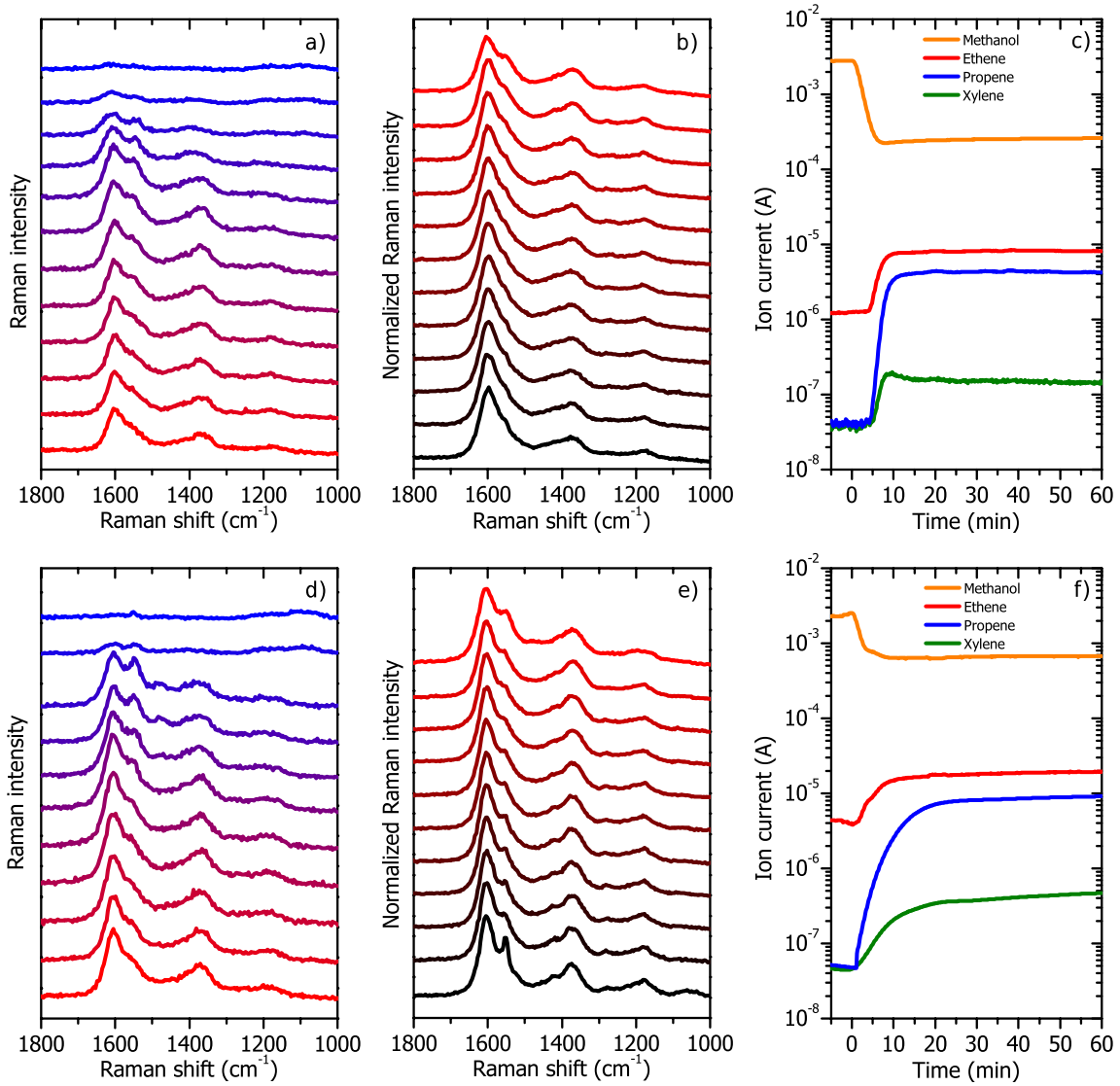

Figure 3.11 UV-Raman spectra of H-ZSM-5 reacting with methanol at 400°C in *operando* conditions: in the spinning pellet flow cell a) in the 0-5 min time lapse (time evolution from blue to red, 30 s accumulation for each spectrum); and b) in the 5-30 min time lapse (time evolution from red to black, 5 min accumulation for each spectrum); and in the Linkam CCR1000 d) in the 0-5 min time lapse (time evolution from blue to red, 30 s accumulation for each spectrum); and e) in the 5-30 min time lapse (time evolution from red to black, 5 min accumulation for each spectrum). The ion currents measured for some selected reactants/products are reported for both c) the spinning pellet and f) Linkam CCR1000 cells. The spectra in panels b and e have been normalized to their most intense signal.

across the first 4-6 spectra a sudden growth of the usual features (*e.g.* maxima at 1600 cm^{-1} and 1400 cm^{-1}) is observed. This initial stage can be preliminary ascribed to the establishment of the hydrocarbon pool and, until a sufficient number of autocatalytic species is not formed, the proper MTH reaction cannot take place. For both the reactors the initial stages are

considerably similar, thus suggesting the mechanism (for the ZSM-5 catalyst) is actually independent from the reaction bed conditions at early reaction times. In the case of the fluidized bed, a slight difference is represented by the presence of the already commented feature with maximum close to 1450 cm^{-1}, ascribable to methanol, which can be probably observed at the earliest reaction stages as a consequence of the better catalyst-reactant contact achieved in these conditions. However, as the induction time is completed, the signal disappears, and thus the entire supplied methanol can react as the hydrocarbon pool is established. Concerning the spectra collected at later reaction time, the behavior of the catalyst is rather constant along the observes period: as also suggested by the plateaus in the ions signals detected by MS, the catalyst is probably working in steady state conditions, indeed the relative intensities of the various hydrocarbon species are not expected to be subjected to important variations (as actually observed). With respect to the *in situ* batch approach, a major difference is the lesser formation of naphthalenes: the region just below 1400 cm^{-1}, even if the presence of sharp features can be inferred, does not show the clear maximum due to the bulk formation of these moieties. Two possible interpretations can be given: i) in the batch reaction, as an enormous amount of methanol is supplied almost instantaneously, the reaction kinetics are extremely fast, thus the UV-Raman spectra give the picture of a fast evolving system also reaching the end of its catalytic life; ii) in flow conditions, as (by)products can be in principle depleted from the catalyst by the reaction stream and, as only adsorbed species contribute to the Raman spectrum, cannot be detected with the same efficiency of batch conditions. Apart this mismatch, all the main features previously commented are encountered, also suggesting that the batch reaction actually follows the same path of the flow one.

As conclusive remark, ZSM-5 can be effectively characterized by UV-Raman in various reaction conditions: even if the univocal assignment of all

the spectral features is not straightforward, most of them (at least the principal ones) can be related to class of compounds of interest in the understanding of the MTH reaction and deactivation paths. UV-Raman, in more general terms, was found to be a relevant tool not only in the study of deactivation mechanism (occurring at long reaction times), but of initial stages (intended as the induction period/establishment of the hydrocarbon pool) as well. The natural continuation of this work will be to exploit *operando* conditions in a rational study of reaction variables (catalyst topology and morphology, temperature, acidity, *etc*), adding time by time a new sentence to the complex puzzle of MTH. As last step of this thesis work concerning MTH, the preliminary results from *operando* investigation on the five topologically different catalysts already treated in the *ex situ* study are reported. In order to give an overall picture of the outcome, the spectra collected (with both the spinning pellet and the Linkam CCR1000 cells) after 1 h of reaction are shown in Figure 3.12.

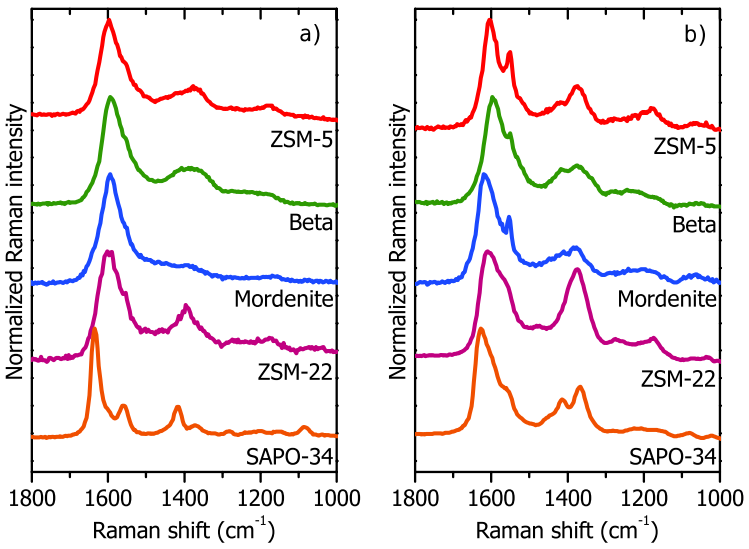

Figure 3.12 Comparison of the UV-Raman spectra of the five topologically different catalysts, collected with a) the spinning pellet cell; and b) with the Linkam CCR1000 cell after 1 h of reaction.

A detailed assignment of the spectral components will not be give here: anyway most of the features are coincident with those ones already commented for the *ex situ* experiments reported in Figure 3.8. At this preliminary stage, the comparison of the different catalytic bed conditions in determining the final type of coke is more interesting. Concerning the spinning pellet cell (simulating a fixed bed reactor), the spectra collected after 1 h of reaction are closely similar to the *ex situ* experiment ones (with the only exception for ZSM-22, probably due to experimental drawbacks). In the case of the Linkam CCR1000 fluid-bed reactor, instead, the coke is rather different: in particular, bulk species seem to be always present, also in the case of samples expected to give molecular type coke (*i.e.* SAPO-34). This peculiar behavior is unexpected: fluid-bed conditions should in fact improve the transport properties, *i.e.* facilitating the feeding of reactant and the elimination of (by)products. Assuming that bulk coke grows by condensation of byproducts, its formation should be unfavored in these conditions. This is still an open point: hopefully, upon the complete data analysis, an interpretation of this unexpected phenomenon could be give.

References

(1) U.S. Energy Information Administration. *International Energy Outlook*; **2016**.

(2) Wittcoff, H. A.; Reuben, B. G.; Plotkin, J. S. *Industrial Organic Chemicals, 3rd Edition*; John Wiley & Sons, Inc., **2013**.

(3) Chang, C. D. Hydrocarbons from Methanol. *Catal. Rev.* **1983**, *25* (1), 1–118.

(4) Olsbye, U.; Svelle, S.; Bjørgen, M.; Beato, P.; Janssens, T. V. W.; Joensen, F.; Bordiga, S.; Lillerud, K. P. Conversion of Methanol to Hydrocarbons: How Zeolite Cavity and Pore Size Controls Product Selectivity. *Angew. Chemie-International Ed.* **2012**, *51* (24), 5810–

5831.

(5) Hemelsoet, K.; Van der Mynsbrugge, J.; De Wispelaere, K.; Waroquier, M.; Van Speybroeck, V. Unraveling the Reaction Mechanisms Governing Methanol-to-Olefins Catalysis by Theory and Experiment. *ChemPhysChem* **2013**, *14* (8), 1526–1545.

(6) Tian, P.; Wei, Y.; Ye, M.; Liu, Z. Methanol to Olefins (MTO): From Fundamentals to Commercialization. *ACS Catal.* **2015**, *5* (3), 1922–1938.

(7) Aguayo, A. T.; Gayubo, A. G.; Vivanco, R.; Olazar, M.; Bilbao, J. Role of Acidity and Microporous Structure in Alternative Catalysts for the Transformation of Methanol into Olefins. *Appl. Catal. A Gen.* **2005**, *283* (1–2), 197–207.

(8) Bjørgen, M.; Joensen, F.; Lillerud, K.-P.; Olsbye, U.; Svelle, S. The Mechanisms of Ethene and Propene Formation from Methanol over High Silica H-ZSM-5 and H-Beta. *Catal. Today* **2009**, *142* (1–2), 90–97.

(9) Choi, M.; Na, K.; Kim, J.; Sakamoto, Y.; Terasaki, O.; Ryoo, R. Stable Single-Unit-Cell Nanosheets of Zeolite MFI as Active and Long-Lived Catalysts. *Nature* **2009**, *461* (7261), 246–249.

(10) Bleken, F.; Bjørgen, M.; Palumbo, L.; Bordiga, S.; Svelle, S.; Lillerud, K.-P.; Olsbye, U. The Effect of Acid Strength on the Conversion of Methanol to Olefins Over Acidic Microporous Catalysts with the CHA Topology. *Top. Catal.* **2009**, *52* (3), 218–228.

(11) Kim, J.; Choi, M.; Ryoo, R. Effect of Mesoporosity against the Deactivation of MFI Zeolite Catalyst during the Methanol-to-Hydrocarbon Conversion Process. *J. Catal.* **2010**, *269* (1), 219–228.

(12) Li, J.; Wei, Y.; Liu, G.; Qi, Y.; Tian, P.; Li, B.; He, Y.; Liu, Z. Comparative Study of MTO Conversion over SAPO-34, H-ZSM-5 and H-ZSM-22: Correlating Catalytic Performance and Reaction Mechanism to Zeolite Topology. *Catal. Today* **2011**, *171* (1), 221–228.

(13) Teketel, S.; Skistad, W.; Benard, S.; Olsbye, U.; Lillerud, K. P.; Beato, P.; Svelle, S. Shape Selectivity in the Conversion of Methanol to Hydrocarbons: The Catalytic Performance of One-Dimensional 10-Ring Zeolites: ZSM-22, ZSM-23, ZSM-48, and EU-1. *ACS Catal.* **2012**, *2* (1), 26–37.

(14) Bleken, F. L.; Chavan, S.; Olsbye, U.; Boltz, M.; Ocampo, F.; Louis, B. Conversion of Methanol into Light Olefins over ZSM-5 Zeolite: Strategy to Enhance Propene Selectivity. *Appl. Catal. A Gen.* **2012**, *447–448*, 178–185.

(15) Álvaro-Muñoz, T.; Márquez-Álvarez, C.; Sastre, E. Use of Different Templates on SAPO-34 Synthesis: Effect on the Acidity and Catalytic Activity in the MTO Reaction. *Catal. Today* **2012**, *179* (1), 27–34.

(16) Jamil, A. K.; Muraza, O.; Yoshioka, M.; Al-Amer, A. M.; Yamani, Z. H.; Yokoi, T. Selective Production of Propylene from Methanol Conversion over Nanosized ZSM-22 Zeolites. *Ind. Eng. Chem. Res.* **2014**, *53* (50), 19498–19505.

(17) Teketel, S.; Lundegaard, L. F.; Skistad, W.; Chavan, S. M.; Olsbye, U.; Lillerud, K. P.; Beato, P.; Svelle, S. Morphology-Induced Shape Selectivity in Zeolite Catalysis. *J. Catal.* **2015**, *327*, 22–32.

(18) Park, J. W.; Lee, J. Y.; Kim, K. S.; Hong, S. B.; Seo, G. Effects of Cage Shape and Size of 8-Membered Ring Molecular Sieves on Their Deactivation in Methanol-to-Olefin (MTO) Reactions. *Appl. Catal. A Gen.* **2008**, *339* (1), 36–44.

(19) Bjørgen, M.; Akyalcin, S.; Olsbye, U.; Benard, S.; Kolboe, S.; Svelle, S. Methanol to Hydrocarbons over Large Cavity Zeolites: Toward a Unified Description of Catalyst Deactivation and the Reaction Mechanism. *J. Catal.* **2010**, *275* (1), 170–180.

(20) Schmidt, F.; Paasch, S.; Brunner, E.; Kaskel, S. Carbon Templated SAPO-34 with Improved Adsorption Kinetics and Catalytic Performance

in the MTO-Reaction. *Microporous Mesoporous Mater.* **2012**, *164*, 214–221.

(21) Schmidt, F.; Lohe, M. R.; Büchner, B.; Giordanino, F.; Bonino, F.; Kaskel, S. Improved Catalytic Performance of Hierarchical ZSM-5 Synthesized by Desilication with Surfactants. *Microporous Mesoporous Mater.* **2013**, *165*, 148–157.

(22) Gayubo, A. G.; Benito, P. L.; Aguayo, A. T.; Olazar, M.; Bilbao, J. Relationship between Surface Acidity and Activity of Catalysts in the Transformation of Methanol into Hydrocarbons. *J. Chem. Technol. Biotechnol.* **1996**, *65* (2), 186–192.

(23) Park, J. W.; Kim, S. J.; Seo, M.; Kim, S. Y.; Sugi, Y.; Seo, G. Product Selectivity and Catalytic Deactivation of MOR Zeolites with Different Acid Site Densities in Methanol-to-Olefin (MTO) Reactions. *Appl. Catal. A Gen.* **2008**, *349* (1–2), 76–85.

(24) Deimund, M. A.; Harrison, L.; Lunn, J. D.; Liu, Y.; Malek, A.; Shayib, R.; Davis, M. E. Effect of Heteroatom Concentration in SSZ-13 on the Methanol-to-Olefins Reaction. *ACS Catal.* **2016**, *6* (2), 542–550.

(25) Wilson, S.; Barger, P. The Characteristics of SAPO-34 Which Influence the Conversion of Methanol to Light Olefins. *Microporous Mesoporous Mater.* **1999**, *29* (1–2), 117–126.

(26) Schulz, H. "Coking" of Zeolites during Methanol Conversion: Basic Reactions of the MTO-, MTP- and MTG Processes. *Catal. Today* **2010**, *154* (3–4), 183–194.

(27) Borodina, E.; Meirer, F.; Lezcano-González, I.; Mokhtar, M.; Asiri, A. M.; Al-Thabaiti, S. A.; Basahel, S. N.; Ruiz-Martinez, J.; Weckhuysen, B. M.; Lezcano-González, I.; et al. Influence of the Reaction Temperature on the Nature of the Active and Deactivating Species during Methanol to Olefins Conversion over H-SSZ-13. *ACS Catal.* **2015**, *5* (2), 992–1003.

(28) Ferrari, A.; Robertson, J. Interpretation of Raman Spectra of Disordered

and Amorphous Carbon. *Phys. Rev. B* **2000**, *61* (20), 14095–14107.

(29) Ferrari, A. C.; Robertson, J. Resonant Raman Spectroscopy of Disordered, Amorphous, and Diamondlike Carbon. *Phys. Rev. B* **2001**, *64* (7), 75414.

(30) Li, C.; Stair, P. C. Ultraviolet Raman Spectroscopy Characterization of Coke Formation in Zeolites. *Catal. Today* **1997**, *33* (1–3), 353–360.

(31) Chua, Y. T.; Stair, P. C. An Ultraviolet Raman Spectroscopic Study of Coke Formation in Methanol to Hydrocarbons Conversion over Zeolite H-MFI. *J. Catal.* **2003**, *213* (1), 39–46.

(32) Beato, P.; Schachtl, E.; Barbera, K.; Bonino, F.; Bordiga, S. Operando Raman Spectroscopy Applying Novel Fluidized Bed Micro-Reactor Technology. *Catal. Today* **2013**, *205* (0), 128–133.

(33) Guisnet, M.; Magnoux, P. Coking and deactivation of zeolites: influence of the pore structure. *Appl. Catal.* **1989**, *54* (1), 1–27.

(34) Asher, S.; Johnson, C. Raman Spectroscopy of a Coal Liquid Shows That Fluorescence Interference Is Minimized with Ultraviolet Excitation. *Science* **1984**, *225* (4659), 311–313.

(35) Avila Ferrer, F. J.; Barone, V.; Cappelli, C.; Santoro, F. Duschinsky, Herzberg – Teller, and Multiple Electronic Resonance Interferential Effects in Resonance Raman Spectra and Excitation Profiles. The Case of Pyrene. *J. Chem. Theory Comput.* **2013**, *9* (8), 3597–3611.

(36) Fraenkel, D.; Cherniavsky, M.; Ittah, B.; Levy, M. Shape-Selective Alkylation of Naphthalene and Methylnaphthalene with Methanol over H-ZSM-5 Zeolite Catalysts. *J. Catal.* **1986**, *101* (2), 273–283.

(37) Frisch, M. J.; Yamaguchi, Y.; Gaw, J. F.; Schaefer, H. F.; Binkley, J. S. Analytic Raman Intensities from Molecular Electronic Wave Functions. *J. Chem. Phys.* **1986**, *84* (1), 531.

(38) Márquez, F.; Zicovich-Wilson, C. M.; Corma, A.; Palomares, E.; García, H. Naphthalene Included within All-Silica Zeolites: Influence of the Host

on the Naphthalene Photophysics. *J. Phys. Chem. B* **2001**, *105* (41), 9973–9979.

(39) Chua, Y.; Stair, P. C. A Novel Fluidized Bed Technique for Measuring UV Raman Spectra of Catalysts and Adsorbates. *J. Catal.* **2000**, *196* (1), 66–72.

(40) Dutta, P. K.; Rao, K. M.; Park, J. Y. Correlation of Raman Spectra of Zeolites with Framework Architecture. *J. Phys. Chem.* **1991**, *95* (17), 6654–6656.

(41) Scarano, D.; Zecchina, A.; Bordiga, S.; Geobaldo, F.; Spoto, G.; Petrini, G.; Leofanti, G.; Padovan, M.; Tozzola, G. Fourier-Transform Infrared and Raman Spectra of Pure and Al-, B-, Ti- and Fe-Substituted Silicalites: Stretching-Mode Region. *J. Chem. Soc. Faraday Trans.* **1993**, *89* (22), 4123.

(42) Knops-Gerrits, P.-P.; De Vos, D. E.; Feijen, E. J. P.; Jacobs, P. A. Raman Spectroscopy on Zeolites. *Microporous Mater.* **1997**, *8* (1–2), 3–17.

(43) Boccuzzi, F.; Coluccia, S.; Ghiotti, G.; Morterra, C.; Zecchina, A. Infrared Study of Surface Modes on Silica. *J. Phys. Chem.* **1978**, *82* (11), 1298–1303.

(44) Sarv, P.; Tuherm, T.; Lippmaa, E.; Keskinen, K.; Root, A. Mobility of the Acidic Proton in Broensted Sites of H-Y, H-Mordenite, and H-ZSM-5 Zeolites, Studied by High-Temperature 1H MAS NMR. *J. Phys. Chem.* **1995**, *99* (38), 13763–13768.

(45) Franke, M. E.; Sierka, M.; Simon, U.; Sauer, J. Translational Proton Motion in Zeolite H-ZSM-5. Energy Barriers and Jump Rates from DFT Calculations. *Phys. Chem. Chem. Phys.* **2002**, *4* (20), 5207–5216.

(46) Girlando, A.; Pecile, C. The Raman Spectrum of Hexamethylbenzene Single Crystal. *Chem. Phys. Lett.* **1973**, *20* (5), 467–470.

(47) Colthup, N. B.; Daly, L. H.; Wiberley, S. E. *Introduction to Infrared and Raman Spectroscopy*; Elsevier, **1975**.

Chapter 4

Titanium Silicalite-1: experimental approach

Titanium Silicalite-1 (TS-1), along its thirty-years old history, has been widely characterized by numerous experimental techniques. In the first, pioneering stages the researchers from EniChem demonstrated the introduction of the titanium atoms in the siliceous MFI framework of Silicalite-1 on the basis of three simple observations:

1. all the synthesized material, independently from their Ti loading, on the basis of diffraction experiments were isostructural with the purely siliceous Silicalite-1;
2. the cell volume derived from diffraction was increasing linearly as the Ti loading increased;
3. a characteristic infrared band, with maximum at 960 cm^{-1}, was observed in Ti substituted materials, with an intensity linearly increasing with the Ti loading.

These findings, together with the exceptional activity and selectivity in partial oxidation reaction toward numerous organic substrates in presence of aqueous hydrogen peroxide, brought in the 1983 to patent the synthesis of TS-1.[1]

Since these first discoveries, TS-1 was the object of several characterization studies which progressively enriched the knowledge on this material. Diffraction techniques provided data of increasing quality, improving both the instrumental potentialities and the ability in the sample handling.[2–4] The highest point achieved by diffraction techniques has been the attainment of the Ti distribution among the 12 possible sites of the MFI framework: these results were obtained by neutron diffraction, exploiting its superior contrast among Ti and Si atoms with respect to standard X-rays diffraction.[5,6] Simultaneously, even larger developments arose from spectroscopic

approaches: FTIR,[7–12] optical,[8,12,13] X-rays adsorption and emission,[8–10,14–17] and (of course) Raman[7,18–22] spectroscopies were diffusely applied, giving rise to a constant enrichment in the understanding of TS-1 and its catalytic sites. It is really important to underline that most of these studies actually exploited the complementarity among the different spectroscopic techniques, allowing a better understanding of the system as observed from different points of view.

Even if TS-1 is probably one of the better characterized heterogeneous catalysts, in the recent years some new question "re-ignited" the debate on this material. In detail, the interest of the scientific community moved toward the characterization of defective Ti sites in TS-1: in the past defective materials (even if already documented)[13,23] were disregarded because: i) the definition of the defects structures is not straightforward; and ii) the presence of defects was expected to have a negative effect on the catalytic performances. Nowadays the exact structures are still unknown, but some insights have been obtained: the defects surely own a higher coordination with respect to the perfect framework Ti (*e.g.* penta- or octa-hedral) and maybe they are no longer single Ti site (*e.g.* Ti-O-Ti chains, titania nanoclusters, etc).[13,23–26] Concerning the effects on the reactivity, in some cases defects have been confirmed to produced a negative or nil effect on the catalytic performances,[27,28] but also an ameliorative contribution has been reported for some specific Ti species.[26]

The experimental results reported in this Chapter are the results of an active collaboration with Evonik Industries AG on the open questions of TS-1 defectivity, aiming to develop a method to qualitatively and quantitatively depict the Ti speciation. The possibility to completely characterize a wide variety of TS-1 materials allowed to increase the fundamental understanding on the various Ti sites. In combination with a parallel computational approach (see Chapter 5), this study helped giving a precise definition of the structure and the related properties of some specific defects.

4.1 Experimental

A spectroscopic method for the evaluation of the nature of the Ti sites was developed, based on Diffuse Reflectance (DR) UV-Vis spectroscopy, Raman spectroscopy (exploiting multiple excitation laser lines) and FTIR (both in transmission and ATR modes). A set of three representative samples was selected: some of their main features are reported in Table 4.1.

Table 4.1 Ti loading and surface area for the selected samples. Analytic data courtesy of Evonik Industries AG.

Sample name	TiO_2 wt% (ICP)	Surface area (m^2g^{-1})
TS-1A	2.44	479
TS-1B	2.89	512
TS-1C	4.33	481

Three different materials have been provided by Evonik Industries AG, showing different Ti loadings and speciation as it will be discussed in the following. However the quite similar values of surface areas point to the macroscopical homogeneity of the samples. DR-UV-Vis spectra were collected on a Varian Cary5000 spectrophotometer, equipped with a diffuse reflectance sphere. The samples were measured in a home-made quartz cell, allowing to perform thermal and/or vacuum treatments. All the materials in their bare form were characterized first in air, then upon the following activation treatments: i) outgassing at RT for 1 h ($p \sim 10^{-1}$ mbar); ii) outgassing at high temperature under high vacuum ($< 10^{-3}$ mbar), reaching the final temperature (500 °C) with a ramp of 5 °C/min; the final temperature was kept for 1 h. The same fractions of sample measured in activated form by DR-UV-Vis were exploited in the ATR-FTIR measurements as well: these were performed on a Bruker Alpha instrument, equipped with DTGS detector and single reflection

diamond ATR accessory. The re-exposure of the samples to atmosphere was avoided as the instrument is placed in a N_2 filled glove-box, preserving them in their activated form during the measurement. The ATR-FTIR spectra were collected with a resolution of 2 cm^{-1}, accumulating 32 scans. The Raman spectra were collected in air by exploting three different excitation lines: 1064 nm (Bruker, solid state laser), 266 nm (CryLas FQSS266-Q2, solid state laser) and 244 nm (Coherent MotoFred 300C, frequency doubled Ar^+ laser). Each laser is coupled with a different instrument: 1064 nm spectra were collected on a Bruker RFS100 Fourier-transformed Raman spectrometer. The 266 nm spectra were collected at the IUVS beamline Raman facility (Elettra synchrotron, Trieste, Italy) on a home-built macro Raman setup:[29] the scattered light is dispersed by a three-stages TriVista 557 spectrometer (Princeton Instruments) equipped with a 1800 line/mm grating and detected by an UV enhanced CCD. The 244 nm Raman was performed on a Renishaw inVia Raman Microscope spectrometer, equipped with 3600 line/mm grating and UV enhanced CCD detector. The FTIR spectra in transmission mode were collected with a Bruker Vertex70 spectrometer, equipped with a cryogenic MCT detector. 32 scans were performed for each spectrum, at a resolution of 2 cm^{-1}. The samples were prepared as thin self-supported pellets and activated (following the same procedure previously described for DR-UV-Vis) in an home-made quartz cell. The measurements were performed in the same cell, *i.e.* without re-exposing the sample to the external atmosphere.

4.2 Qualification of the Ti sites

The starting point for the Ti identification has been to establish a fast screening method, able to face the high sample throughput proper of an industrial R&D department, as well as the requirement to select the most interesting samples for fundamental research. The technique of choice for these purposes was the optical spectroscopy: as documented in the literature,

the presence of different Ti structures gives rise to well distinguishable electronic transition, genuine fingerprints for their qualitative identification.[8,12,13] Very briefly, the perfect tetrahedral, in-framework Ti sites give a sharp peak with maximum at 50000 cm-1 ascribed to the Ligand-to-Metal Charge Transfer (LMCT) transitions of the TiO4 moieties.[8,13,30] Lowering the energy, the range comprise between 45000-35000 cm-1 is interested by the electronic transitions of defective sites: as already introduced, the origin of such features is controversial since many unidentified structures can give rise to them. The lower energy with respect to the perfect Ti sites can be symptomatic of a higher coordination number in the Ti ligand sphere, as well as an incipient clustering of TiOx species.[13,23–26] What is clear is that more than a single defective structure exhibit their spectral features in this region, making the interpretation really complex. Finally, reaching even lower frequencies (down to 30000 cm-1), the electronic transitions of extended TiO_2 phases can be encountered.[31–33] An important variable to take into account evaluating the optical spectra of TS-1 is its hydration state: the presence of molecules coordinated to the c.u.s. sites of the perfect tetrahedral Ti can affect their electronic transition, *i.e.* causing a significant red-shift of the absorption peak and a possible overlap with the signal proper of defects.[8,12] Because of this, the TS-1 samples should be properly activated in order to obtain meaningful results. The Diffuse Reflectance (DR) UV-Vis spectra of some selected TS-1 samples are reported in Figure 4.1. The DR-UV-Vis measurement were carried out under different conditions in order to find out the proper measurements method: the spectra were collected on the materials as such in air, upon dehydration by low vacuum ($p \sim 10^{-1}$ mbar) treatment at ambient temperature and, finally, after an high temperature/high vacuum activation procedure ($p < 10^{-3}$ mbar, 1h at 500 °C, 5 °C/min ramp from RT).

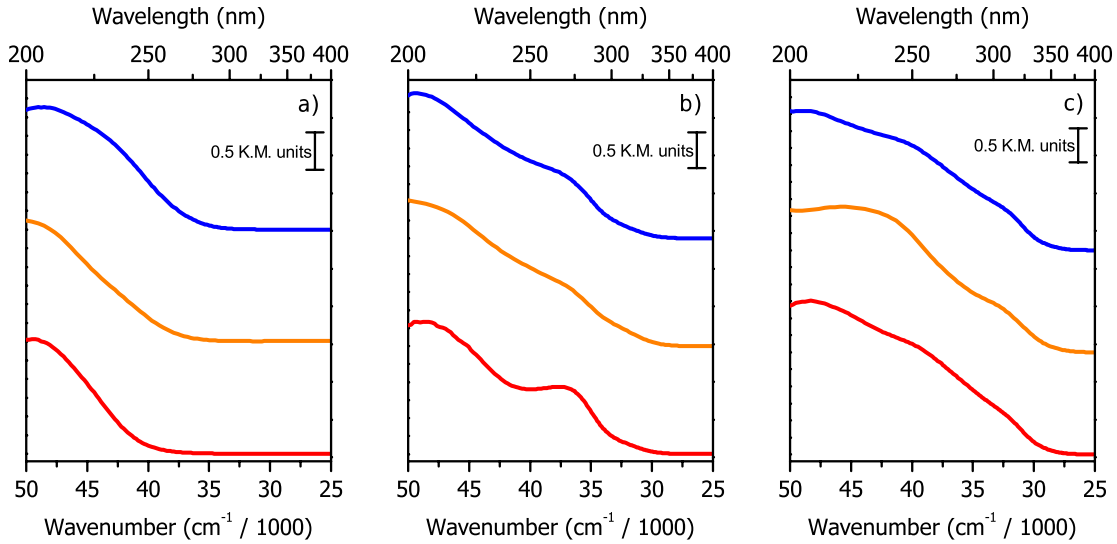

Figure 4.1 DR-UV-Vis spectra of the a) TS-1A; b) TS-1B; and c) TS-1C samples collected: in air (blue lines); upon low vacuum treatment at RT ($p \sim 10^{-1}$ mbar, orange lines); and upon high vacuum and thermal treatment ($p < 10^{-3}$ mbar, 500°C, red lines).

The TS-1A spectra exhibit a single transitions with maximum at 50000 cm^{-1}, quite broad when the measurement is performed in air. That band is surely ascribable to perfect tetrahedral Ti sites, as also confirmed upon mild and strong activations: applying vacuum, the signal sharpens loosing the low frequency shoulder, testifying the progressive dehydration of the Ti sites. The difference observed between mild and strong activation is not really pronounced, suggesting that perfect sites can be easily cleaned from weak adsorbates (*e.g.* water). This is not the case of sample TS-1B, where the mild outgassing at RT does not produces a modification of the spectral features. However, already in the spectrum collected in air, the presence of a second band with maximum at ~ 37000 cm^{-1} can be inferred. In order to resolve this signal the high temperature/high vacuum treatment is compulsory: the band is now clearly distinguishable, showing a narrow width possibly related to a well-defined electronic transition (*i.e.* to a precise defective structure). The presence of such structure makes the interaction of the TS-1B sample with water more strong, as the difficulties encountered in the dehydration demonstrate. Concerning their hypothetical structure, the few literature

assignments available ascribe the electronic transitions falling in that spectral region to octahedrally coordinated species, possibly clusterized.[13,23,25] Finally the TS-1C sample is the less affected by activation (note: the spectrum collected after mild dehydration is probably affected by some instrumental artifacts), showing negligible variations even after the high vacuum thermal treatment. The last point can be interpreted in different ways: i) the huge concentration of defects make the material so hydrophilic that the applied treatment becomes ineffective; ii) conversely, the kind of defects are really hydrophobic, making the material unable to interact with water; iii) the electronic transitions of the various defects are so overlapped that the hydration effect cannot be properly evaluated. Considering the contributions to the spectrum, the TS-1C material shows a wide distribution of Ti species giving rise to a variety of electronic transitions: together with the perfect sites, several type of defective structures are observed as testified by the very broad tail extending down to 30000 cm^{-1}. The very low transition energies reached suggest that some extended titania phases are formed as well: according to the heavy Ti loading of this sample (see Table 4.1) it is absolutely reasonable that a bulk, crystalline TiO_2 phase is formed. Anyway DR-UV-Vis is not able to univocally state which TiO_2 polymorph is formed, since all the main titania phases exhibit very similar electronic fingerprints.[31–33]

As optical spectroscopy represents the faster screening method, Raman spectroscopy can be regarded as a very powerful tool able to look closer to the Ti sites. The possibility of Raman spectroscopy toward TS-1 are in fact very rich: being the main piece of the information of vibrational type, Raman is able to give also electronic insights thanks to the possibility to exploit the resonance effect (see Chapter 1 for theoretical details). Resonant Raman is useful in the characterization of TS-1: while the vibrational modes related to Ti shows a poor intensity in out-of-resonance measurements, they are enhanced by orders of magnitude as the proper conditions are adopted. In detail, it is

sufficient to excite the sample with a wavelength approaching the one of the characteristic optical absorption of Ti sites to achieve such resonance, as the associated electronic transitions own the same symmetry of certain peculiar vibration involving Ti. In this way, some features related to Ti turn to be the dominant contributions to the Raman spectrum. Of course adequate technical means are required, *i.e.* the correct excitation lasers must be exploited: in the case of TS-1 this means that a UV-Raman instrumentation is required. Being a well established approach for perfect sites,[20,21] recently resonant UV-Raman has been successfully applied also to the characterization of defect-like structure in TS-1 synthetic environment by Guo and coworkers.[25] Because of this, a multiple excitation (UV-)Raman study was performed: the spectra of the three materials, collected in air, are reported in Figure 4.2. The TS-1A (Figure 4.2a), when measured out of resonance (*i.e.* 1064 nm excitation) shows as dominating spectral features the bands ascribed to the siliceous MFI framework (as the 380 cm^{-1} peak due to ring motions and the 800 cm^{-1} band due to the Si-O-Si symmetric stretching modes).[7,34,35] The evidence of the Ti insertion in the framework is given by a pair of bands in the high frequency region: the 960 cm^{-1} feature, ascribed to the antisymmetric Ti-O-Si stretching modes, and the weak contribution at 1125 cm^{-1}, related to the symmetric Ti-O-Si stretching.[11,12] Fully exploiting the resonance conditions as allowed by the 244 nm excitation line, the 1125 cm^{-1} band is selectively enhanced, becoming the most intense spectral feature and showing an intensity ratio with respect to the 960 cm^{-1} inverted in comparison with the out-of-resonance spectrum. Two further features (other than the 1125 cm^{-1} and 960 cm^{-1} contributions), which have not yet deeply investigated, are observed: an intense and broad band centered at 500 cm^{-1}, possibly arising from the convolution of more signals as suggested by its unusual shape, and a small maximum at 780 cm^{-1}. The origin of the 500 cm^{-1} band has been attributed by Li et al.[19] to framework

motions involving the Ti, as similar bands are not observed in the pure siliceous Silicalite-1.

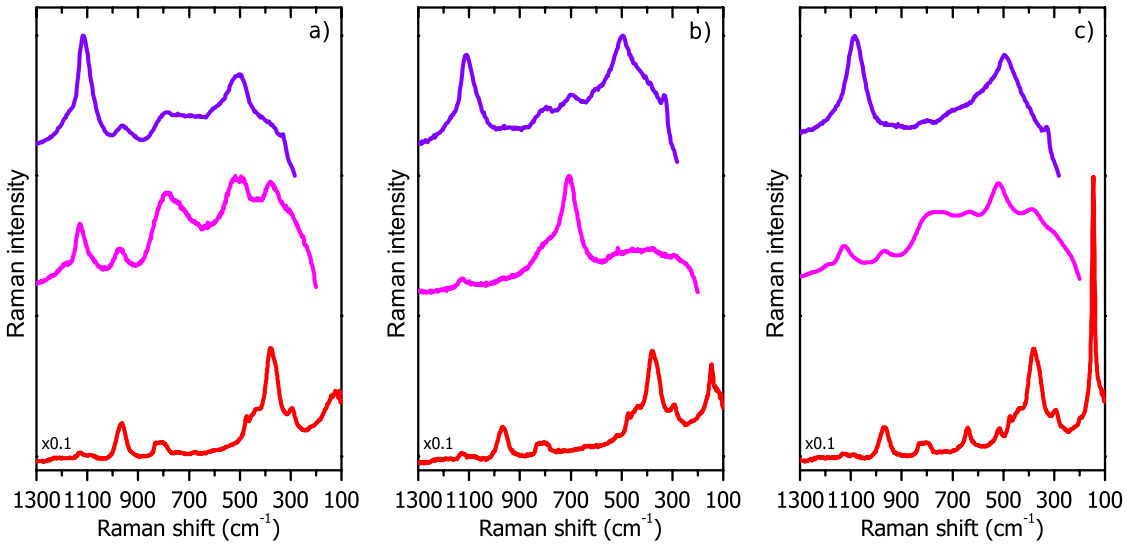

Figure 4.2 Raman and UV-Raman spectra of samples a) TS-1A; b) TS-1B; and c) TS-1C collected with excitation wavelengths of: 1064 nm (red lines), 266 nm (magenta lines) and 244 nm (violet lines). The spectra were collected in air. The 1064 nm spectra were multiplied by a factor 0.1 for sake of visualization.

However a precise assignment is not given in the literature and dedicated studies are required to fully elucidate its origin. The same situation occurs for the 780 cm^{-1} peak, but with the help of the spectrum collected with the 266 nm excitation some hypothesis can be formulated: by lowering the excitation energy, the resulting spectrum looks like a convolution of the ones previously commented (as the resonance conditions for the perfect Ti are fairly satisfied). Interestingly the relative intensity of the 780 cm^{-1} with respect to the tetrahedral Ti features is much higher, suggesting a specific resonance for the species causing it. According to the DR-UV-Vis spectra reported in Figure 4.1, the spectrum of the TS-1A sample collected in air (*i.e.* in presence of water coordinated to the Ti sites) is still able to absorb photons in the vicinity of the excitation wavelength (266 nm), while upon activation the low frequency tail of the tetrahedral Ti sites is completely eroded. This can suggest that the vibration observed at 780 cm^{-1} arises from a Ti-$(H_2O)_x$ adsorption complex,

selectively enhanced by the 266 nm excitation wavelength (and, in a lesser extent, also by the 244 nm one). Other interesting insights have been obtained on the sample TS-1B: looking at the out-of-resonance spectrum only this material looks quite similar to TS-1A. The only visible difference is the presence of a sharp peak at 144 cm^{-1}, easily ascribable to the E_g vibration of anatase:[36] in this regard, Raman spectroscopy is much more sensitive of DR-UV-Vis in detecting TiO_2, since the optical spectrum of TS-1B revealed only a weak tail on the region of bulk titania electronic transitions (~ 30000 cm^{-1}). Very interestingly, the resonant spectra obtained with the 266 nm and 244 nm excitations look totally different with respect to each other: the former is dominated by a single feature with maximum at 700 cm^{-1}, the latter instead resembles the TS-1A spectrum (*i.e.* determined by the perfect Ti sites) with a much weaker contribution at 700 cm^{-1}. The result obtained with the 266 nm excitation points to the existence of a well defined kind of defect as already suggested by DR-UV-Vis spectroscopy: a Ti defective structure with similar spectroscopic fingerprints was observed by Guo and coworkers,[25] who described it as "isolated octahedral titanium species". The case of TS-1B sample demonstrates the importance of a multiple excitation approach in the Raman characterization of TS-1: a small change in the incidence wavelength can lead to dramatically different spectra, as each electronic transition gives rise to a different resonance. Finally, the TS-1C sample exhibits a 1064 nm spectrum dominated by the convolution of the TS-1 signals with the well known fingerprints of anatase: in addition to the peak at 144 cm^{-1}, other two bands are observed at 515 cm^{-1} and 640 cm^{-1}.[36] The high anatase content observed is perfectly in line with the outcomes of optical spectroscopy. Unexpectedly the 266 nm and 244 nm Raman spectra are really similar to the corresponding ones for the TS-1A sample. The former is quite complex but can be rationalized as a combination of the spectra produced by framework (390 cm^{-1}), perfect Ti sites (500 cm^{-1}, 960 cm^{-1}, 1125 cm^{-1} and hydration complex

close to 780 cm^{-1}) and anatase (640 cm-1 and possible overlaps with the 500 cm^{-1} and 390 cm^{-1} bands). The latter instead is fully determined by the tetrahedral Ti species. These results are apparently astonishing considering the richness of electronic transitions highlighted by DR-UV-Vis in the vicinity of the excitation wavelengths, *i.e.* very specific resonant Raman spectra are expected. Possibly the wide heterogeneity of the defects makes the concentration of the single Ti species so low that they cannot be effectively probed. Alternatively the resonance conditions are not achieved for symmetry reasons: the vibrational modes of defects could not match the symmetry of their electronic transitions. Another option could be the outcome of purely absorptive phenomena for the defects: being the excitation exactly matching the energy of the electronic transitions of a given Ti moiety, the inelastic scattering leading to the Raman signal cannot occur as all the incoming photons are absorbed.

The importance to perform multiple excitation wavelengths Raman experiments (especially in the UV region) leaded to the submission of a proposal (n. 20155146, "Resonant UV Raman spectroscopy applied to TS-1 zeolites characterized by different Ti species") for beamtime at the IUVS beamline at the Elettra synchrotron facility (Trieste, Italy): this has been recently implemented with a Raman setup, allowing in principle to perform measurements with variable excitation wavelength in the 280-200 nm range with an almost continuous tunability.[29] The power of such approach has been widely discussed in the previous paragraph, as it can allow to selectively enhance the vibrational mode of a specific Ti moiety with a tuning level unapproachable by conventional laser sources. Unluckily the low optimization of the setup for solid samples (it has been mainly developed for solution studies) brought to unsatisfactory results: as an example, the spectrum collected for the TS-1A sample at 225 nm is reported in Figure 4.3.

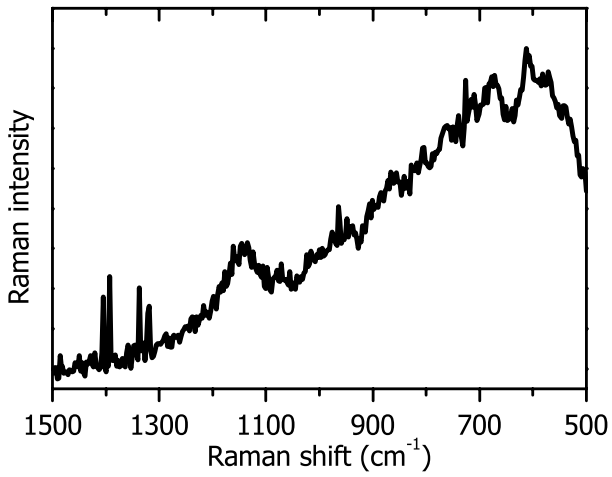

Figure 4.3 UV-Raman spectrum (synchrotron excitation source) of samples TS-1A collected with an excitation wavelengths λ = 225 nm.

Even if the spectral quality is low, the main feature of the tetrahedral Ti (1125 cm^{-1} peak) is identified, demonstrating the reliability of the setup. Hopefully the setup will be progressively improved, opening to the possibility to perform meaningful resonant Raman experiments with variable excitation. Despite the current failure of the synchrotron approach, the IUVS beamline allows to perform conventional laser Raman experiments as well: in particular a diode 266 nm UV laser is available, being of particular interest for the TS-1 characterization. Some of the obtained results have been already shown in Figure 4.2 and consequently discussed. Furthermore some preliminary controlled atmosphere experiments were carried out: an activation similar to the one performed for DR-UV-Vis was performed, but limiting the treatment temperature to 150 °C for technical reasons. Even if 500 °C were not reached, according to the DR-UV-Vis characterization, such procedure should guarantee a reasonable dehydration level (at least for the perfect TS-1A sample). Further, the samples were exposed to the vapor pressure of H_2O to systematically verify the effect of hydration. The same experiment was repeated for sake of comparison with the 244 nm Raman instrument in Torino.

The UV-Raman (266 nm and 244 nm) spectra for the TS-1A and TS-1B are reported in Figure 4.4.

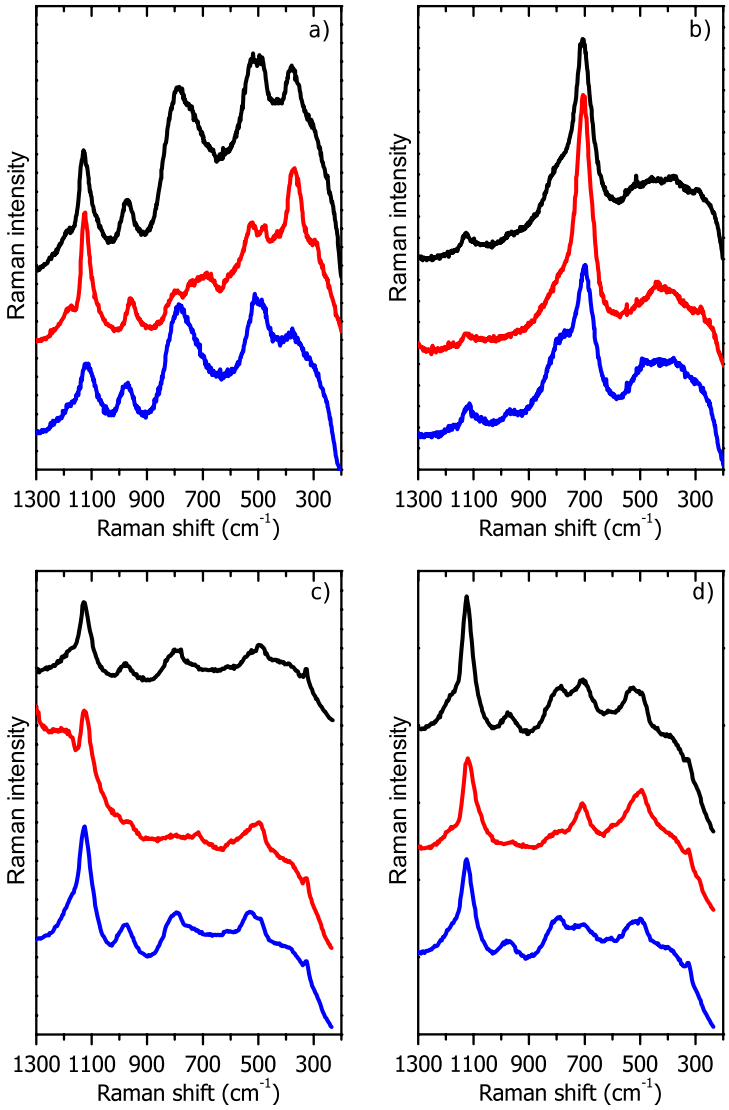

Figure 4.4 UV-Raman spectra of a) TS-1A (266 nm); b) TS-1B (266 nm); c) TS-1A (244 nm); and d) TS-1B (244 nm) samples collected: in air (black lines), upon activation in vacuum ($p < 10^{-3}$) at 150 °C (red lines) and after contact with the vapor pressure of H_2O at RT (blue lines).

In both the 266 nm and 244 nm measurements, the spectra of the activated TS-1A do not show anymore the intense feature with maximum at 780 cm^{-1}. Instead, the signals from the framework and the perfect Ti sites are maintained: with 266 nm excitation these are of similar intensity, whereas in

the 244 nm spectrum the latter completely overcome the former thanks to the stronger resonance achieved with this wavelength toward the perfect Ti sites. Furthermore (still with 244 nm excitation), even if the signal is slightly affected by a interfering background, the 960 cm^{-1} peak is observed to almost disappear with respect to the dominant 1125 cm^{-1} one: most probably the elimination of water and/or other ligands further increases the resonance of the most symmetric vibration, indeed prevailing on all the other components. Another interesting behavior is related to the band at 500 cm^{-1}: in the 266 nm spectrum it decreases in intensity and it is resolved in two well defined components (maxima at 480 cm^{-1} and 520 cm^{-1} respectively). Conversely, with the 244 nm line, the feature looks more intense and a sharper maximum (480 cm^{-1}) is now clearly defined. Even if not clearly giving rise to a maximum (as for the 266 nm excitation), also the presence of the second component at 520 cm^{-1} can be inferred by the asymmetric shape of the band. The complexity of the low frequency region of TS-1 is again pointed out, which signal intensities are probably determined by the combination of different resonance extents and hydrated structures. Dedicated experiments are thus required to clarify its intimate relations with the Ti sites. As water is dosed back, the spectra return very similar to the one collected in air. With 266 nm excitation, both the framework and the tetrahedral Ti spectral features look less intense in comparison to the corresponding signals in the air spectrum, probably because of the much larger amount of water interacting with the sample. In the 244 nm case the 960 cm^{-1} band is restored and the background is quenched: this suggests that a sample contamination occurred during the dehydration procedure, giving rise to a (rare) case of fluorescence in the mid-UV range. The dosage of a relevant amount of water molecules allows the energy arising from photons absorption to be dissipated in a non-emissive way (*e.g.* vibrationally), thus avoiding the emission by pollutants. The 780 cm^{-1} band appears again upon hydration, as observed with both excitation wavelengths,

and thereby its relation with Ti-H_2O complexes is highly probable. An analogous behavior is observed also for the modes falling around 500 cm^{-1}, where the relative intensities of the two main components turn back to the one observed for the sample in air for the 244 nm excitation. In 266 nm measurements, instead, the intensity of the 500 cm^{-1} features rises again with a concomitant broadening of the signal: in this case most probably a third band component, strictly related to a hydrated Ti structure, is responsible for such spectral modification. The TS-1B sample presents a simpler trend upon (de)hydration: in the 266 nm spectra, the 700 cm^{-1} peak is the main spectral feature along the whole experiment, whereas the perfect Ti features are still dominant in the 244 nm set of spectra. The different resonances achieved upon different excitation are the main reason for such diversity, since different Ti species are selectively enhanced. The dosage of the water, concerning the 266 nm experiment, "regulates" the intensity of the perfect Ti sites, which turn to be more evident as the sample hydrates. This is probably connected to the extension toward lower energies of the electronic transition of tetrahedral Ti, allowing these sites to "enter in resonance" and to better compete with the more absorbing defects. The behavior under 244 nm excitation is instead following the same interpretation for the TS-1A sample, with a further enhancement of the 1125 cm^{-1} with respect to all the other components in anhydrous conditions. Again, the trend already commented for the 780 cm^{-1} and 500 cm^{-1} bands is observed for both the excitations. Finally, considering the effect of water on the defective Ti sites, the most important observation is the lack of a peak shift for the 700 cm^{-1} band as the hydration state changes (while a displacement is clearly observed for the tetrahedral Ti features, especially for the 960cm^{-1} band).[7,21] A possible explanation is that the Ti site is completely surrounded by permanent ligands, *e.g.* in an octahedral field, thus not accessible to the dosed molecules. Concerning the relative intensity of the peak with respect to the signals of the tetrahedral Ti, this increases as the

water content is reduced. By exciting with the 266 nm excitation, only the defective sites own an electronic transition in the vicinity of this wavelength in the dehydrated state, whereas the perfect Ti sites exhibit a closer one only if hydrated. In presence of water, the two species are competitors in capturing the incoming exciting photons, resulting in a "balance" of the related resonant enhancements of the Raman intensities. With 244 nm excitation, a similar pattern is observed, even if smoothed by the larger fraction of photons drained by the perfect sites.

4.3 Quantification of the Ti sites

The capability to quantify (or at least to give an estimate of) the amount of the various Ti species observed in TS-1 is a considerable added value to the understanding of this system. Industrially it is a very important analytical tool in order to progressively improve the synthesis of the real catalysts. Concerning more fundamental aspects, to know the exact distribution of the Ti among the different sites can be really helpful in making correlations with the catalytic activity as the effect of the defects in epoxidation reactions is controversial.[26–28] A four-step quantification protocol was developed:

1. the total amount of Ti (Ti_{tot}) is determined by elemental analysis (ICP);
2. the amount of tetrahedral framework Ti (Ti_{fram}) is determined by FTIR exploiting the 960 cm^{-1} band;
3. the (eventual) amount of anatase (Ti_{anat}) is obtained by Raman referring to the 144 cm^{-1} peak;
4. the amount of defects (Ti_{def}) is obtained by difference, *i.e.* $Ti_{def} = Ti_{tot} - Ti_{fram} - Ti_{anat}$.

This procedure represents the state-of-art for Ti quantification: the only weakness is the impossibility to further discriminate among the possible defects, but it is the best compromise since their real nature is still unclear.

Skipping the routine ICP analysis, the first relevant step is the quantification of the tetrahedral Ti: in the introductory paragraphs of this chapter, the linear relation between the amount of framework Ti and the absorbance of the infrared band at 960 cm^{-1} was introduced.[1,11] The dependence reported in the literature was obtained through standard transmission FTIR. The main drawback of this approach is represented by the sample preparation: in order to obtain quantitative information, the samples cannot be diluted, thus extremely thin self-supported TS-1 pellets must be used in order to keep in scale the 960 cm^{-1} peak. This sample preparation becomes indeed time consuming, incompatibly with the time framework of an industrial quality control laboratory. To avoid such problem, Attenuated Total Reflectance (ATR) FTIR was applied: this measurement method allows to obtain results comparable with the transmission ones, but keeping all the signals in scale disregarding the sample preparation. The only tricky point is the sample hydration state: the presence of water (or other ligands) coordinated to the Ti sites can lead to an alteration of the intensity of the 960 cm^{-1} band,[21,37] thus affecting the quantification. The samples indeed need to be activated (as for the DR-UV-Vis) and then measured avoiding their re-exposure to the atmosphere: this condition was achieved by collecting the ATR spectra with an instrument placed inside a dry, N_2 filled glovebox, therefore keeping them activated. As first step, a calibration line was built: some dedicated materials with Ti content in the 0.5-2.5 $_{wt}$% were synthesized by Evonik Industries and their purity (*i.e.* the complete framework inclusion of the Ti) was checked by DR-UV-Vis. Also the TS-1A sample was included in the curve construction. Since these materials contain only perfect tetrahedral Ti, the relation $Ti_{fram} = Ti_{tot}$ is satisfied. In this way, the numerical integrated area of the 960 cm^{-1} band was related to the total Ti amount (evaluated as TiO_2 $_{wt}$%) determined by ICP: the obtained calibration curve is shown in Figure 4.5a.

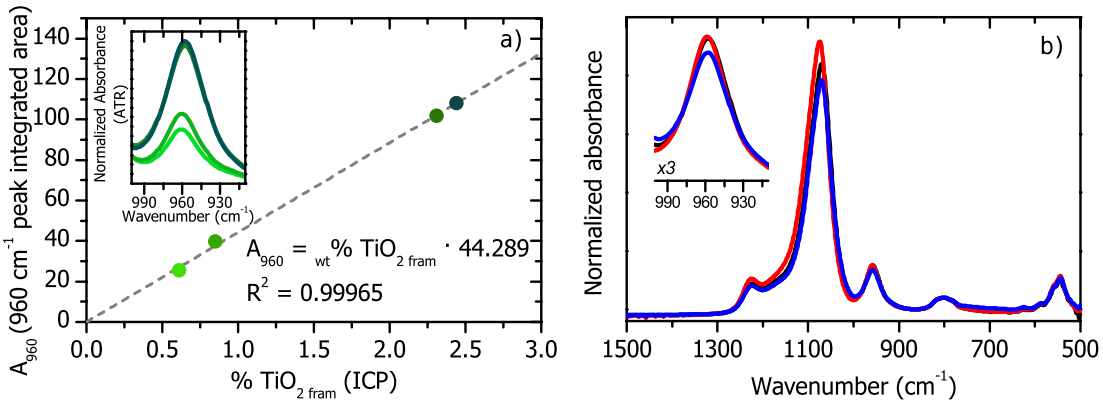

Figure 4.5 ATR-FTIR calibration curve for the determination of the framework Ti amount (panel *a*) and ATR-FTIR spectra for the TS-1A (black line), TS-1B (red line) and TS-1C (blue line) samples (panel *b*). In the insets, the details for the 960 cm^{-1} peak for calibration (panel *a*) and TS-1A, TS-1B and TS-1C (panel *b*) samples are presented. All the spectra refers to materials activated in high vacuum ($p < 10^{-3}$ mbar) at 500°C and were normalized to the 800 cm^{-1} to guarantee a quantitative comparison.

An important requirement in order to obtain quantitative data is to perform a proper spectral normalization: the 800 cm^{-1} band, ascribed to the Si-O-Si symmetric stretching modes of the siliceous framework,[7] was exploited as convenient internal reference. The relation obtained shows an optimal linearity, thereby allowing its exploitation for quantitative purposes. A significant improvement to the calibration will be the inclusion of other points to the line, possibly in the 1.5-2.0 $_{wt}$% concentration range. The ATR-FTIR spectra were then collected as showed in Figure 4.5b. Upon normalization at 800 cm^{-1}, the three TS-1 samples are characterized by similar framework Ti contents, being this slightly lower for TS-1C.

After achieving the quantification of tetrahedral Ti, the next step is to obtain the amount of anatase produced during the synthesis. As stated earlier in this chapter (see Figure 4.2 and the related comments), Raman is probably the most sensitive to anatase among the ones considered in this work. The real problem concerning quantification by Raman spectroscopy is the sample homogeneity: usually Raman instruments are coupled with a microscope in the so called micro-Raman configuration, thus taking advantage of the focusing of

the excitation light in a limited spatial region (*i.e.* obtaining a gain in the signal intensity). Depending on the magnification provided by the microscope/objective, the probed area can span approximately in the 1-10 μm^2 range. Being really helpful in terms of intensity enhancement, micro-Raman thus also enriches the technique with spatial resolution in the micro scale. This fact is often an advantage (*e.g.* it allows to check the sample homogeneity), but can become a serious drawback concerning quantitative studies: point by point, the intensity of the modes related to the phase of interest can considerably change. When micro-Raman is applied to quantitative analyses, the sample homogeneity must be verified, *i.e.* multiple measurement has to be performed and compared. If the relative intensities of the signal of interest with respect to an internal reference are varying significantly among the test measurement, indeed the sample is heterogeneous on the considered length scale. Thus, the measurement should be repeated a sufficiently large number of time in order to obtain an average view of the sample, *i.e.* tens of spectra must be collected and averaged, with an heavy time consumption. Regarding the anatase quantification in TS-1, the heterogeneity problem did not involve the main samples, but it was dramatic as a set of standard materials had to be considered for calibration purposes. In fact the only effective synthetic strategy was the impregnation of siliceous Silicalite-1 with preformed nano-anatase particles: the nano-anatase (Aldrich, <25 nm particle size, 99.7% purity) was added in a given amount to the Silicalite-1 gel before to start its crystallization. Inducing the latter, Silicalite-1 particles embedding the TiO_2 phase were obtained. Since Ti incorporation phenomena in the framework were not observed (no 960 cm^{-1} from FTIR, no electronic transition at 50000 cm^{-1} from DR-UV-Vis), the total Ti amount determined by ICP correspond for these materials to Ti_{anat}. The easiest solution to the homogeneity problem was the exploitation of a macro-Raman setup, which spatial resolution is about 10-100 times lower than in a micro-Raman

instrument. In this way, even a single measurement directly gives an average idea of the sample. Furthermore macro-FT-Raman was exploited in the present study: with respect to a dispersive instrument, the Fourier Transform based acquisition method allows a significant speedup of the collection time keeping constant the signal-to-noise ratio. The obtained calibration curve is presented in Figure 4.6, together with the FT-Raman spectra of the three TS-1 samples.

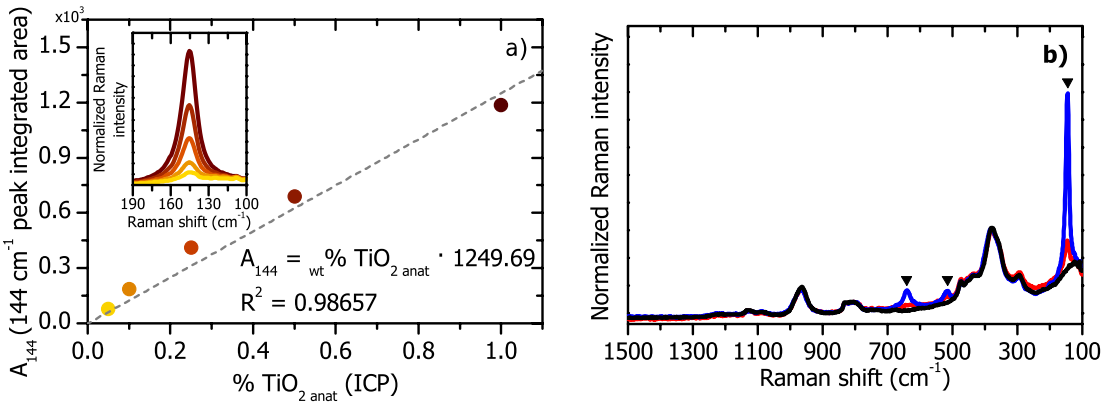

Figure 4.6 a) FT-Raman calibration curve for the determination of the anatase amount and b) FT-Raman spectra for the TS-1A (black line), TS-1B (red line) and TS-1C (blue line) samples (panel *b*). In the inset of panel a, the details for the 144 cm^{-1} peak for calibration samples is presented. All the spectra were collected in air and they were normalized to the 800 cm^{-1} to guarantee a quantitative comparison. The triangles label the position of the anatase distinctive signals.

The quality of the calibration line, even if slightly lower with respect to the framework Ti one, is sufficiently high to obtain trustable data. The spectra consistently reproduce the qualitative result from DR-UV-Vis and micro-Raman (see Figure 4.1 and Figure 4.2 respectively): TS-1A does not show the presence of anatase; TS-1B containss a low amount of anatase, as testified by the weak intensity of the 144 cm^{-1} peak; TS-1C instead is characterized by a relevant amount of TiO_2 and the secondary signals proper of the anatase phase are easily recognized as well.

Owning all the necessary elements, the speciation of the Ti sites in the three considered samples can be stated: the results are reported in Table 4.2.

Table 4.2 Speciation of Ti sites expressed as $TiO_{2\ wt}$%. In brackets, the fraction of each type of site, calculated as: $_{wt}\%\ TiO_{2\ site}$ / $_{wt}\%\ TiO_{2\ tot}$.

Sample	$_{wt}\%\ TiO_{2\ tot}$	$_{wt}\%\ TiO_{2\ fram}$	$_{wt}\%\ TiO_{2\ anat}$	$_{wt}\%\ TiO_{2\ def}$
TS-1A	2.44	2.44 (1.00)	0.00 (0.00)	0.00 (0.00)
TS-1B	2.89	2.57 (0.89)	0.12 (0.04)	0.19 (0.07)
TS-1C	4.33	2.09 (0.48)	0.37 (0.09)	1.88 (0.43)

The data shows that irrespective of the synthesis a threshold exists for the Ti incorporation and this is comprised between 2-3 $_{wt}\%\ TiO_{2\ fram}$. Concerning the not incorporated Ti, they are preferentially of defective type rather than in the extended anatase phase: this is particularly relevant in the case of TS-1C sample, where defects represent the 43% of the Ti species against an anatase content approximately five times lower. What is missing in the picture presented in Table 4.2 is a more detailed description of the so defined defects: this could be really important in the proper interpretation of catalytic data, as it will be commented in the next section of this chapter. The only possibility to shed light on this open topic is to progressively increase their, identifying their structures and relating them to their spectroscopic fingerprints.

4.4 Catalytic performances: comparison with spectroscopic results

The final point reached in this thesis work concerning TS-1 has been to combine the set of obtained characterization results with the outcomes of catalytic tests for the conversion of propene to propene oxide with hydrogen peroxide as oxidizing agent (the so called HPPO process). Evonik performed

the tests on the bare TS-1 powders: these were conducted in a continuously stirred batch reactor, where the TS-1 catalyst is suspended in methanol. The reactor is heated to 40 °C and then pressurized up to 3 bars by introducing propene. To start the reaction, the required amount of 30% aqueous solution of hydrogen peroxide is loaded in the reactor. The initial molar composition for the TiO_2(TS-1) : H_2O_2 : propene: H_2O : methanol mixture is approximately 1 : 400 : 860 : 1700 : 48000, indeed the catalyst amount (here considering only the molar amount of Ti sites) is really small in comparison to other reactants. The reaction is performed along 1 h and its evolution is evaluated after 5, 10, 20, 30, 45 and 60 min: in detail, the residual amount of H_2O_2 is titrated by ceric sulfate method, whereas the reaction products are quantified by gas chromatography. The results of the test for samples TS-1A, TS-1B and TS-1C are graphically outlined in Figure 4.7. The catalytic test showed that all the samples are considerably active toward the propene epoxidation reaction: the conversion of the peroxide is very high, reaching the 95% for both TS-1A and TS-1B samples after 1 h. A slightly lower value is achieved with the TS-1C catalyst, where the conversion at 60 min is "only" 86%.

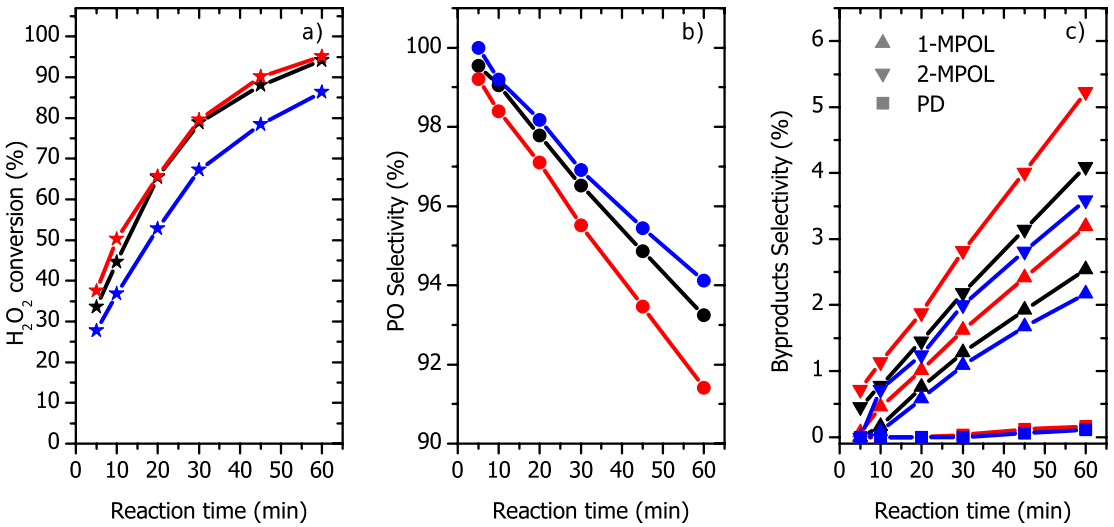

Figure 4.7 Catalytic data for the HPPO reaction performed on the TS-1A (black lines), TS-1B (red lines) and TS-1C (blue lines) samples: a) H2O2 conversion; b) Propene Oxide (PO) selectivity; and c) byproducts (MPOL-1, 1-Methoxy-2-propanol; MPOL-2, 2-Methoxy-1-propanol; PD, Propane-1,2-diol) selectivity.

In order to give a better comparison of the three materials, the rate constants for the H_2O_2 conversion were calculated assuming the reaction to be of pseudo-first order (being the excess reactant the catalyst, since it is not consumed by definition) and the reaction rate r can be expressed as:

$$r = -k[H_2O_2][TS1]_0 \tag{4.1}$$

where $[H_2O_2]$ is the concentration of hydrogen peroxide at a given time, $[TS1]_0$ is the concentration of Ti sites of the TS-1 catalyst (assumed to be constant along the reaction) and k is the reaction rate constant. Since $[TS1]_0$ is assumed constant, a new pseudo-first order rate constant k' can be defined:

$$k' = k[TS1]_0 \tag{4.2}$$

and Eq. 4.1 is thus recasted as:

$$r = -k'[H_2O_2] \tag{4.3}$$

Another way to express the reaction rate taking into account its time dependence is:

$$r = -\frac{d[H_2O_2]}{dt} \tag{4.4}$$

Substituting Eq. 4.3 in Eq. 4.4 and rearranging Eq. 4.5 is obtained:

$$\frac{d[H_2O_2]}{[H_2O_2]} = -k'dt \tag{4.5}$$

Integrating over a time range $0 \rightarrow t$ where the peroxide concentration varies as $[H_2O_2]_0 \rightarrow [H_2O_2]$ the concentration $[H_2O_2]$ at time t is expressed as:

$$\ln\frac{[H_2O_2]}{[H_2O_2]_0} = -k't \tag{4.6}$$

where $[H_2O_2]_0$ corresponds to the initial concentration of hydrogen peroxide. Further considering the conversion-concentration relation:

$$\frac{[H_2O_2]}{[H_2O_2]_0} = 1 - conversion \tag{4.7}$$

the (a) panel of Figure 4.7 is transformed as reported in Figure 4.8 thanks to the relation:

$$\ln(1 - conversion) = -k't \tag{4.8}$$

The slopes of the new curves, obtained by linear fitting, represent the $-k'$ values for the three catalysts from which the k rate constants can be evaluated dividing by $[TS1]_0$, the TiO_2 weight concentration of each TS-1 catalyst with respect to the full reaction batch.

$$[TS1]_0 = \frac{weight(\mathrm{TiO_2})}{weight(\mathrm{batch})} \tag{4.9}$$

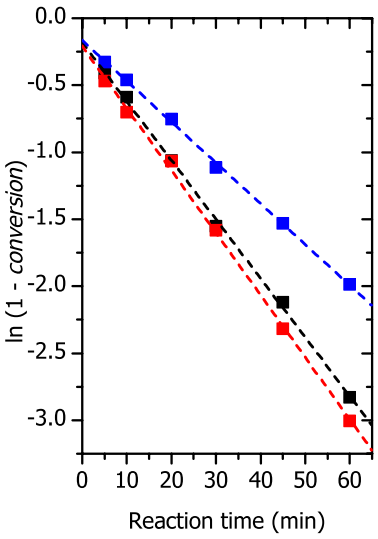

Figure 4.8 Linear fit calculation of rate constants k' for the TS-1A, TS-1B and TS-1C catalysts toward H_2O_2 conversion in the HPPO reaction.

Two different values of $[TS1]_0$ were chosen: the first one considering the whole TiO_2 amount measured by ICP, the second one taking into account only the framework tetrahedral TiO_2 fraction as determined by ATR (see Table 4.2). The results that have been obtained are reported in Table 4.3. The results

shown in Table 4.3 depict the main role of tetrahedral framework sites in determining the TS-1 activity toward propene epoxidation: as the rate constants are calculated considering the total TiO_2 content of the catalysts (k_{tot}) a considerable spreading of the values is observed among the different materials. Such broad distribution could suggest that most of the Ti defective sites are not active toward H_2O_2 conversion. A confirmation to this interpretation arises from the k_{fram} (*i.e.* computed taking into account the framework TiO_2 content only) values, being these much closer among the three catalysts. In detail TS-1A and TS-1B show almost identical k_{fram}, whereas TS-1C presents a lower value: the discrepancy is possibly related to other effects, such as diffusive problems, which reduce the rate of conversion of H_2O_2.

Table 4.3 Calculation of the rate constants $\boldsymbol{k_{tot}}$ and $\boldsymbol{k_{fram}}$, obtained considering the whole TiO_2 amount and the framework TiO_2 content only respectively.

Sample	k' (min^{-1})	Catalyst weight (g)	TiO_2 tot weight (g)	TiO_2 fram weight (g)	Batch tot. weight (g)	k_{tot} (min^{-1})	k_{fram} (min^{-1})
TS-1A	0.037	1.024	0.025	0.025	422.7	620	620
TS-1B	0.027	1.064	0.031	0.027	422.2	563	633
TS-1C	0.041	1.038	0.045	0.022	421.7	255	531

Another important point is the lesser role of peroxide decomposition: if Ti defective structures would act effectively in H_2O_2 degradation, the k_{fram} for TS-1B and TS-1C should look artificially larger than one of TS-1A because of the overlapping of decomposition and proper conversion to products.

If the Ti speciation seems to be a secondary factor in determining the H_2O_2 conversion, it could play a main role with respect to the formation of

byproducts. In fact, the initial selectivity toward propene oxide is about 100% for all the catalysts, whereas it is reduced progressively along the reaction time because of the increasingly formation of by products deriving from the esterification of propene oxide by methanol (thus giving 1-Methoxy-2-propanol and 2-Methoxy-1-propanol) or by its hydrolysis (obtaining the Propane-1,2-diol). Because of the different activities of the catalysts, a direct comparison of selectivities is not straightforward: in order to correctly look at the data, reaction yields were computed at 80% conversion (Table 4.4). Even if the difference among the three catalysts are pretty small, the TS-1A univocally shows a higher yield of the desired product, thus a lower production of byproducts. Indeed it is possible to infer that the defects observed for catalysts TS-1B are slightly detrimental for the selectivity towards PO. TS-1C shows a similar behavior but, since its defects content is about 50% of the total Ti amount (see Table 4.2), these has to be considered mostly as spectators, not affecting the reactivity.

Table 4.4 Reaction yields at 80% H_2O_2 conversion for: Propene Oxide (PO), 1-Methoxy-2-propanol (MPOL-1), 2-Methoxy-1-propanol (MPOL-2) and Propane-1,2-diol (PD).

	Yield at 80% conversion (%)			
Sample	PO	MPOL-1	MPOL-2	PD
TS-1A	77.02	1.10	1.86	0.02
TS-1B	76.34	1.34	2.33	0.05
TS-1C	76.30	1.36	2.30	0.04

In order to properly evaluate the catalytic features of the TS-1 materials, the tests will be repeated by increasing the reaction time, indeed allowing all the catalysts to reach complete conversion. Furthermore, the reproducibility of the tests should be verified, as well as the catalyst cyclability.

References

(1) Notari, B.; Perego, G.; Taramasso, M. Preparation of Porous Crystalline Synthetic Material Comprised of Silicon and Titanium Oxides. *US4410501 A*, **1983**.

(2) Millini, R.; Previde Massara, E.; Perego, G.; Bellussi, G. Framework Composition of Titanium Silicalite-1. *J. Catal.* **1992**, *137* (2), 497–503.

(3) Lamberti, C.; Bordiga, S.; Zecchina, A.; Carati, A.; Fitch, N. N.; Artioli, G.; Petrini, G.; Salvalaggio, M.; Marra, G. L. L. Structural Characterization of Ti-Silicalite-1: A Synchrotron Radiation X-Ray Powder Diffraction Study. *J. Catal.* **1999**, *183* (2), 222–231.

(4) Millini, R.; Perego, G.; Berti, D.; Parker, W. O.; Carati, A.; Bellussi, G. Structural Characterization of as-Synthesized B- and Ti-Containing MFI-Type Molecular Sieves. *Microporous Mesoporous Mater.* **2000**, *35-36*, 387–403.

(5) Hijar, C. A.; Jacubinas, R. M.; Eckert, J.; Henson, N. J.; Hay, P. J.; Ott, K. C. The Siting of Ti in TS-1 Is Non-Random. Powder Neutron Diffraction Studies and Theoretical Calculations of TS-1 and FeS-1. *J. Phys. Chem. B* **2000**, *104* (51), 12157–12164.

(6) Lamberti, C.; Bordiga, S.; Zecchina, A.; Artioli, G.; Marra, G.; Spanò, G. Ti Location in the MFI Framework of Ti-Silicalite-1: A Neutron Powder Diffraction Study. *J. Am. Chem. Soc.* **2001**, *123* (10), 2204–2212.

(7) Scarano, D.; Zecchina, A.; Bordiga, S.; Geobaldo, F.; Spoto, G.; Petrini, G.; Leofanti, G.; Padovan, M.; Tozzola, G. Fourier-Transform Infrared and Raman Spectra of Pure and Al-, B-, Ti- and Fe-Substituted Silicalites: Stretching-Mode Region. *J. Chem. Soc. Faraday Trans.* **1993**, *89* (22), 4123.

(8) Bordiga, S.; Coluccia, S.; Lamberti, C.; Marchese, L.; Zecchina, A.; Boscherini, F.; Buffa, F.; Genoni, F.; Leofanti, G. XAFS Study of Ti-Silicalite: Structure of Framework Ti(IV) in the Presence and Absence of

Reactive Molecules (H_2O, NH_3) and Comparison with Ultraviolet-Visible and IR Results. *J. Phys. Chem.* **1994**, *98* (15), 4125–4132.

(9) Bolis, V.; Bordiga, S.; Lamberti, C.; Zecchina, A.; Carati, A.; Rivetti, F.; Petrini, G.; Spanò, G. A Calorimetric , IR , XANES and EXAFS Study of the Adsorption of NH_3 on Ti-Silicalite as a Function of the Sample Pre-Treatment. *Microporous Mesoporous Mater.* **1999**, *30*, 67–76.

(10) Bolis, V.; Bordiga, S.; Lamberti, C.; Zecchina, A.; Carati, A.; Rivetti, F.; Spanò, G.; Petrini, G. Heterogeneity of Framework Ti(IV) in Ti–Silicalite as Revealed by the Adsorption of NH_3. Combined Calorimetric and Spectroscopic Study. *Langmuir* **1999**, *15* (18), 5753–5764.

(11) Ricchiardi, G.; Damin, A.; Bordiga, S.; Lamberti, C.; Spano, G.; Rivetti, F.; Zecchina, A.; Spanò, G.; Rivetti, F.; Zecchina, A. Vibrational Structure of Titanium Silicate Catalysts. A Spectroscopic and Theoretical Study. *J. Am. Chem. Soc.* **2001**, *123* (46), 11409–11419.

(12) Bordiga, S.; Damin, A.; Bonino, F.; Zecchina, A.; Spanò, G.; Rivetti, F.; Bolis, V.; Prestipino, C.; Lamberti, C. Effect of Interaction with H_2O and NH_3 on the Vibrational, Electronic, and Energetic Peculiarities of Ti(IV) Centers TS-1 Catalysts: A Spectroscopic and Computational Study. *J. Phys. Chem. B* **2002**, *106* (38), 9892–9905.

(13) Geobaldo, F.; Bordiga, S.; Zecchina, A.; Giamello, E.; Leofanti, G.; Petrini, G. DRS UV-Vis and EPR Spectroscopy of Hydroperoxo and Superoxo Complexes in Titanium Silicalite. *Catal. Letters* **1992**, *16* (1–2), 109–115.

(14) Bordiga, S.; Boscherini, F.; Coluccia, S.; Genonic, F.; Lamberti, C.; Leofanti, G.; Marchese, L.; Petrini, G.; Vlaic, G.; Zecchina, A. XAFS Study of Ti-Silicalite: Structure of Framework Ti(IV) in Presence and in Absence of Reactive Molecules (H_2O, NH_3). *Catal. Letters* **1994**, *26* (1–2), 195–208.

(15) Lamberti, C.; Bordiga, S.; Arduino, D.; Zecchina, A.; Geobaldo, F.;

Spano, G.; Genoni, F.; Petrini, G.; Carati, A.; Villain, F.; et al. Evidence of the Presence of Two Different Framework Ti(IV) Species in Ti–Silicalite-1 in Vacuo Conditions: An EXAFS and a Photoluminescence Study. *J. Phys. Chem. B* **1998**, *102* (33), 6382–6390.

(16) Gallo, E.; Lamberti, C.; Glatzel, P. Investigation of the Valence Electronic States of Ti(IV) in Ti Silicalite-1 Coupling X-Ray Emission Spectroscopy and Density Functional Calculations. *Phys. Chem. Chem. Phys.* **2011**, *13* (43), 19409.

(17) Gallo, E.; Bonino, F.; Swarbrick, J. C.; Petrenko, T.; Piovano, A.; Bordiga, S.; Gianolio, D.; Groppo, E.; Neese, F.; Lamberti, C.; et al. Preference towards Five-Coordination in Ti Silicalite-1 upon Molecular Adsorption. *ChemPhysChem* **2013**, *14* (1), 79–83.

(18) Tozzola, G.; Mantegazza, M. A.; Ranghino, G.; Petrini, G.; Bordiga, S.; Ricchiardi, G.; Lamberti, C.; Zulian, R.; Zecchina, A. On the Structure of the Active Site of Ti-Silicalite in Reactions with Hydrogen Peroxide: A Vibrational and Computational Study. *J. Catal.* **1998**, *179* (1), 64–71.

(19) Li, C.; Xiong, G.; Liu, J.; Ying, P.; Xin, Q.; Feng, Z. Identifying Framework Titanium in TS-1 Zeolite by UV Resonance Raman Spectroscopy. *J. Phys. Chem. B* **2001**, *105* (15), 2993–2997.

(20) Bordiga, S.; Damin, A.; Bonino, F.; Ricchiardi, G.; Lamberti, C.; Zecchina, A. The Structure of the Peroxo Species in the TS-1 Catalyst as Investigated by Resonant Raman Spectroscopy. *Angew. Chemie-International Ed.* **2002**, *41* (24), 4734–4737.

(21) Bordiga, S.; Damin, A.; Bonino, F.; Ricchiardi, G.; Zecchina, A.; Tagliapietra, R.; Lamberti, C. Resonance Raman Effects in TS-1: The Structure of Ti(IV) Species and Reactivity towards H_2O, NH_3 and H_2O_2: An in Situ study. *Phys. Chem. Chem. Phys.* **2003**, *5* (20), 4390.

(22) Guo, Q.; Feng, Z.; Li, G.; Fan, F.; Li, C. Finding the "Missing Components" during the Synthesis of TS-1 Zeolite by UV Resonance

Raman Spectroscopy. *J. Phys. Chem. C* **2013**, *117* (6), 2844–2848.

(23) Blasco, T.; Camblor, M. A.; Corma, A.; Perez-Pariente, J. The State of Ti in Titanoaluminosilicates Isomorphous with Zeolite Beta. *J. Am. Chem. Soc.* **1993**, *115* (25), 11806–11813.

(24) Zuo, Y.; Wang, X.; Guo, X. Synthesis of Titanium Silicalite-1 with Small Crystal Size by Using Mother Liquor of Titanium Silicalite-1 as Seeds (II): Influence of Synthesis Conditions on Properties of Titanium Silicalite-1. *Microporous Mesoporous Mater.* **2012**, *162*, 105–114.

(25) Guo, Q.; Feng, Z.; Li, G.; Fan, F.; Li, C. Finding The "missing Components" during the Synthesis of TS-1 Zeolite by UV Resonance Raman Spectroscopy. *J. Phys. Chem. C* **2013**, *117* (6), 2844–2848.

(26) Zuo, Y.; Liu, M.; Zhang, T.; Hong, L.; Guo, X.; Song, C.; Chen, Y.; Zhu, P.; Jaye, C.; Fischer, D. Role of Pentahedrally Coordinated Titanium in Titanium Silicalite-1 in Propene Epoxidation. *Rsc Adv.* **2015**, *5* (23), 17897–17904.

(27) Zuo, Y.; Wang, X.; Guo, X. Synthesis of Titanium Silicalite-1 with Small Crystal Size by Using Mother Liquid of Titanium Silicalite-1 As Seed. *Ind. Eng. Chem. Res.* **2011**, *50* (14), 8485–8491.

(28) Su, J.; Xiong, G.; Zhou, J.; Liu, W.; Zhou, D.; Wang, G.; Wang, X.; Guo, H. Amorphous Ti Species in Titanium Silicalite-1: Structural Features, Chemical Properties, and Inactivation with Sulfosalt. *J. Catal.* **2012**, *288*, 1–7.

(29) D'Amico, F.; Saito, M.; Bencivenga, F.; Marsi, M.; Gessini, A.; Camisasca, G.; Principi, E.; Cucini, R.; Di Fonzo, S.; Battistoni, A.; et al. UV Resonant Raman Scattering Facility at Elettra. *Nucl. Instruments Methods Phys. Res. Sect. A Accel. Spectrometers, Detect. Assoc. Equip.* **2013**, *703*, 33–37.

(30) Bonino, F.; Damin, A.; Ricchiardi, G.; Ricci, M.; Spanò, G.; D'Aloisio, R.; Zecchina, A.; Lamberti, C.; Prestipino, C.; Bordiga, S. Ti-Peroxo Species

in the TS-1/H_2O_2/H_2O System. *J. Phys. Chem. B* **2004**, *108* (11), 3573–3583.

(31) Amtout, A.; Leonelli, R. Optical Properties of Rutile near Its Fundamental Band Gap. *Phys. Rev. B* **1995**, *51* (11), 6842–6851.

(32) Tang, H.; Lévy, F.; Berger, H.; Schmid, P. E. Urbach Tail of Anatase TiO2. *Phys. Rev. B* **1995**, *52* (11), 7771–7774.

(33) Mattsson, A.; Österlund, L. Adsorption and Photoinduced Decomposition of Acetone and Acetic Acid on Anatase, Brookite, and Rutile TiO2 Nanoparticles. *J. Phys. Chem. C* **2010**, *114* (33), 14121–14132.

(34) Dutta, P. K.; Rao, K. M.; Park, J. Y. Correlation of Raman Spectra of Zeolites with Framework Architecture. *J. Phys. Chem.* **1991**, *95* (17), 6654–6656.

(35) Knops-Gerrits, P.-P.; De Vos, D. E.; Feijen, E. J. P.; Jacobs, P. A. Raman Spectroscopy on Zeolites. *Microporous Mater.* **1997**, *8* (1–2), 3–17.

(36) Ohsaka, T.; Izumi, F.; Fujiki, Y. Raman Spectrum of Anatase, TiO_2. *J. Raman Spectrosc.* **1978**, *7* (6), 321–324.

(37) Bonino, F.; Damin, A.; Bordiga, S.; Lamberti, C.; Zecchina, A. Interaction of CD_3CN and Pyridine with the Ti(IV) Centers of TS-1 Catalysts: A Spectroscopic and Computational Study. *Langmuir* **2003**, *19* (6), 2155–2161.

Chapter 5

Titanium Silicalite-1: computational approach

Beside the experimental approach toward TS-1 characterization presented in Chapter 4, a parallel computational investigation strategy was adopted. TS-1 is in fact an easily suitable system for theoretical purposes: the presence of a metallic center homogeneously inserted in a siliceous crystalline framework makes it an excellent model of single site catalyst. This fact is really interesting for fundamental purposes, since quantum mechanical methods can be applied to a relatively simple (but however realistic) model of the catalyst, indeed allowing to get reliable insights on the intimate nature of the active site. Furthermore, since its crystalline nature, TS-1 is straightforwardly suitable for a periodic computational approach, indeed able to naturally evaluate the effect of the system porosity, without involving extremely large clusters taking into account the pore construction.

With respect to the topic of this thesis, the focus of the computational activity on TS-1 was mostly on the interpretation of the spectroscopic data obtained: in particular, the problem of defectivity in TS-1 can obtain a significant help from simulation in determining univocally the structure of defective species on the basis of their spectroscopic fingerprints. Before to face the intriguing problem of defectivity, however, it has been necessary to develop an adequate model for the perfect TS-1, as will be introduced in the next paragraph.

5.1 Development of a Ti-Chabazite model: a good candidate for TS-1 representation

As already introduced, TS-1 is a siliceous zeolite, belonging to the MFI framework topology, where Ti atoms substitute Si ones at some tetrahedral positions (in the order of two per unit cell). The MFI structure is a relatively large system, characterized by an orthorombic crystal system ($Pnma$ space group) with an asymmetric unit formed by 38 atoms (of which 12 occupying tetrahedral sites). Even in this system size is easily affordable with average computational resources, it turns to be a bulk computational problem as Ti is inserted: in fact each tetrahedral position gives rise through the symmetry operators to 4-8 equivalent atoms, *i.e.* producing an unrealistic Ti loading. The reduction of the symmetry becomes thus unavoidable in order to reach a realistic Ti content and, further considering the spacing among the Ti sites (requested to be sufficiently large to consider them as isolated), it is quite easy that the symmetry operators should be completely depleted. The final $P1$ model contains 288 independent atoms: for this reason, just few papers appeared in the past concerning TS-1.[1–3]

Another possible approach for reducing computational cost is to adopt as TS-1 model other Ti-zeolites with less demanding frameworks: even if this approach could appear as a rough approximation, it is justified by many experimental evidences, showing the similarities of the Ti sites incorporated in different zeolitic frameworks with the typical fingerprints of TS-1.[4–7] In this thesis, Ti-Chabazite (hereafter Ti-CHA) was conveniently exploited as Ti-zeolite model. The Chabazite (CHA) topology, as previously described in the Chapter 3, is rather different from the MFI one under a structural point of view: the former is in fact built by large cages interconnected by small (8 members) windows, whereas the latter is constituted by a 3D network of 10 members channels. CHA is really convenient under a computational point of view, since its rombohedral unit cell ($R\bar{3}m$) contains only 5 independent atoms, of which

only a single tetrahedral site. Apart from the differences in their crystal structures, both TS-1 and Ti-CHA experimentally show a very similar environment for the Ti atoms: the vibrational features from FTIR and Raman spectroscopies, the electronic transitions from optical spectroscopy and the ligand sphere determined by XAS techniques are in fact amazingly coincident.[6] The first step in the Ti-CHA model development was the selection and the optimization of the computational method on the simpler CHA: as previously introduced, the system was mainly described through a periodic approach exploiting the features of the CRYSTAL14 code.[8] All the reported calculation were performed with the B3LYP hybrid DFT functional, combining the B3[9] hybrid exchange functional with the LYP[10] correlation functional. This preliminary study focused on the results of a structural relaxation of CHA, obtained exploiting different basis set and numerical accuracy levels. Dispersive forces were semiempirically included in the calculations through the Grimme GD2 scheme.[11] The final goal was (trivially) to obtain the better agreement with the experimental observables at the lower computational cost. In detail the goodness of the model was evaluated on the basis of three selected parameters as schematized in Figure 5.1.

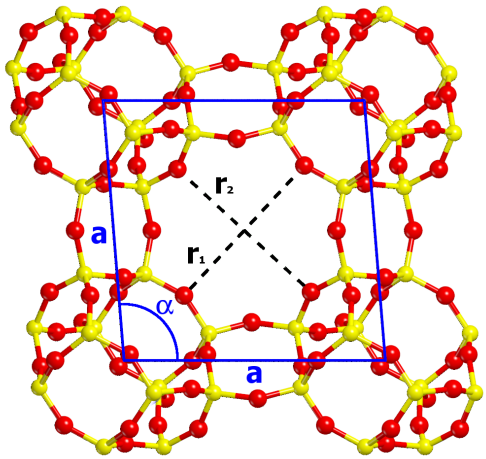

Figure 5.1 Schematic representation of the geometrical parameters evaluated to establish the goodness of the computational approaches toward CHA optimization.

The cell parameter **a**, the cell angle α and the deformation of the 8 members windows, evaluated as the ratio r_1/r_2 of two window radii were chosen. More than 30 computational parameters combinations were attempt: the most significant for the logical understanding of the final method choice are reported in Table 5.1.

Table 5.1 Results of the geometry relaxation calculations of CHA performed with variable Basis Sets (B.S.), integral series truncation thresholds (TOLINTEG) and order of the polynomial approximation of the multipolar expansion of Coulomb interaction (POLEORDR, P.O.): the cell parameter a, the cell angle α and the 8 members window deformation (expressed as r_1/r_2, see Figure 5.1) are reported. The goodness of each approach is evaluated by the figure of merit G, computed as product of the Average Relative Deviations (ARD) of the three geometrical parameters with respect to the experimental values and the average total CPU time per SCF cycle (t_{SCF}).

Si B.S.	O B.S.	TOLINTEG	P.O.	a (Å)	α (°)	r_1 / r_2	ARD	t_{SCF} (h)	G
6-21G(d)[a]	6-311G(d)[a]	7 7 7 7 14	4	9.229	98.6	0.677	0.122	0.48	0.059
		12 12 12 12 24	4	9.358	94.6	0.954	0.020	1.59	0.032
		7 7 7 7 14	6	9.358	94.7	0.949	0.022	0.47	0.011
88-31G(d)[b]	8-411G(d)[b]	7 7 7 7 14	4	9.337	94.3	0.979	0.010	0.55	0.006
		12 12 12 12 24	4	9.336	94.2	0.993	0.006	2.25	0.013
		7 7 7 7 14	6	9.333	94.0	1.003	0.006	0.57	0.004
88-31G(d)[b]	TZV(2d)[c]	7 7 7 7 14	4	9.331	94.6	0.963	0.016	0.79	0.013
		12 12 12 12 24	4	9.332	94.4	0.974	0.012	3.30	0.040
		7 7 7 7 14	6	9.334	94.4	0.974	0.012	0.88	0.011
TZV(2d,d)[d]	TZV(2d)[c]	7 7 7 7 25	4	9.319	94.2	0.994	0.005	6.30	0.031
		7 7 7 7 25	6	9.317	94.5	0.966	0.015	6.16	0.090
Exp.[12]				9.229	94.3	0.998			

a) From Ref. [13]; b) from Ref. [14]; c) from Ref. [15]; d) derived from a Ahlrichs TZVP basis[15] by adding the polarization functions (only *d* type orbitals) from a Ahlrichs def2-TZVP basis.[16]

Discussing the results, with the lower quality basis sets and truncation exponents (*i.e.* low values of the TOLINTEG parameters) the geometrical optimization leads to the collapse of the porous system. In order to restore a correct behavior it is necessary to increase the quality of the basis set (in

particular for the oxygen atoms) and/or to reduce the approximation on integrals (*i.e.* by tightening the truncation criteria). Adopting both these solutions an enlargement of the computational cost is obviously observed, which is undesired in the idea of a following upscale of the system size (*e.g.* due to symmetry reduction upon Ti insertion). A costless way to significantly improve the computational result is to increase the maximum order of the polynomial series fitting the long range electronic Coulomb interaction (POLEORDR parameter): as demonstrated by the values reported in Table 5.1, in this way it is possible to obtain results comparable with ones obtained with very high values for the integral truncation, but without significantly increase the computational cost. In order to rapidly and easily analyze the outcomes of the calculations, a figure of merit G was defined as it follows:

$$G = ARD \cdot t_{SCF} \tag{5.1}$$

where ARD represents the Average Relative Deviations of the three geometrical parameters with respect to the experimental ones and t_{SCF} is the average CPU time for a SCF cycle. Cross-checking the previous assumptions with the calculated G values the surprising effect of the POLEORDR parameter is readily verified: when this is set to 6, the same ARD obtained with tight truncation criteria are computed, however keeping the same t_{SCF} proper of lower quality calculations. Indeed the G values obtained from POLEORDR = 6 calculations are the lowest, *i.e.* the best ones. Finally ranking the reported calculations on the basis of these G values the optimal computational parameters were derived and systematically exploited in the following calculations: 88-31G(d) basis set for Si,[14] 8-411G(d) basis set for O,[14] TOLINTEG = {7 7 7 7 14} and POLEORDR = 6.

The next step in the model construction was the insertion of Ti in the optimized CHA structure. The symmetry was broken and a single Si tetrahedral

site was replaced by a Ti one: the constructed Ti-CHA models has $P1$ symmetry and contains 36 independent atoms. This model, despite its relatively small size (*i.e.* low computational cost), is in principle poorly representative of the real system, as its Si/Ti ratio of 11 is significantly lower than the experimental values for typical TS-1 samples (Si/Ti ~ 50). The calculations were performed as previously determined for CHA, exploiting a 86-411G(3d,d)[17] basis set in the Ti description. A clear demonstration of this assumption arose from the results obtained upon relaxation of the Ti-CHA structure: its cell parameters, angles and volume are given together with CHA ones in Table 5.2.

Table 5.2 Optimized cell parameters for the CHA and Ti-CHA single cell periodic models. For the latter, the average Ti-O distance is given as well. Distances are given in Å, angles in °, volumes in Å^3.

Model	a	b	c	α	β	γ	Volume	<Ti-O>
CHA	9.333	9.333	9.333	94.0	94.0	94.0	807	-
Ti-CHA	9.493	9.211	9.414	94.8	95.3	94.5	814	1.802

Comparing the two structures, the insertion of Ti leads (as expected) to an increase of the cell volume. The expansion is of the order of 0.8%, a typical value for TS-1 with Si/Ti = 50,[18] thus a much bigger value should be found at the present Ti loading. Furthermore the anisotropy in the deformation (expected to by isotropic experimentally)[18] suggests that the system had to find an "unnatural" path for relaxing the strain induced by the excessive Ti loading to the structure. These facts suggest that the separation of the Ti sites (of about 9.5 Å) is not sufficient to consider them as isolated, producing an unrealistic relaxed structure for Ti-CHA. The solution to such drawback was thereby found by increasing the Ti dilution in the siliceous CHA framework (*i.e.* isolating it). The strategy adopted was the following: a supercell of CHA was

constructed, with cell parameters $\boldsymbol{a}'$, $\boldsymbol{b}'$, $\boldsymbol{c}'$ obtained as a linear combination of the single cell ones $\boldsymbol{a}$, $\boldsymbol{b}$, $\boldsymbol{c}$ as reported in Equation 5.2.

$$\begin{aligned} \boldsymbol{a}' &= -\boldsymbol{a} + \boldsymbol{b} + \boldsymbol{c} \\ \boldsymbol{b}' &= \boldsymbol{a} - \boldsymbol{b} + \boldsymbol{c} \\ \boldsymbol{c}' &= \boldsymbol{a} + \boldsymbol{b} - \boldsymbol{c} \end{aligned} \qquad (5.2)$$

The symmetry was completely removed in order to handle a system with the same symmetry operators (*i.e.* the identity only) of the subsequent Ti-CHA model: this operation resulted in a relevant increase of the computational cost, since the number of independent atoms increased to 144. The supercell CHA model was relaxed and, again, Ti was inserted in a single tetrahedral site giving rise to the Ti-CHA supercell model: the final Si/Ti ratio, equal to 47, is now really close to experimental ones for TS-1, indeed a correct behavior of the system is expected. A confirmation is found in the geometrical parameters reported in Table 5.3.

Table 5.3 Optimized cell parameters for the CHA and Ti-CHA supercell periodic models. For the latter, the average Ti-O distance is given as well. Distances are given in Å, angles in °, volumes in Å^3.

Model	a	b	c	α	β	γ	Volume	<Ti-O>
CHA	16.552	16.492	16.491	112.3	111.1	111.1	3180	-
Ti-CHA	16.622	16.494	16.556	111.9	111.4	111.2	3204	1.799

Again an expansion of the cell is observed, according to the correct estimation of the Ti-O distances. The extent of the volume increase is still around 0.8%, however in this case the value nicely fits with the experimental diffraction data obtained on TS-1 with comparable Si/Ti.[18] Also the isotropy of the expansion is better represented by the supercell model: even if the *a* and *c* parameters experienced a larger elongation than the *b* one, all the parameters vary in the

same direction. The variations on the angles are rather small as well. Concluding this section, the supercell Ti-CHA model is able to properly reproduce the geometrical evolution due to the Ti insertion in a siliceous zeolitic framework. However the model should be still validated on the basis of some selected observables: this process will be presented in the following.

5.2 Validation of the Ti-CHA model: adsorption of simple molecules

In order to check the goodness of the supercell Ti-CHA model a set of tests based on the adsorption of NH_3 and H_2O were performed: these simple molecules are in fact convenient for modeling purposes, as well as a rich experimental[19–21] and computational[22–25] dataset is available on this specific topic. Considering the past computational results, even if these gave a proper description of the Ti sites under both geometrical and spectroscopical points of view, the energetic modeling of adsorption processes was unsatisfactory. Citing the example of a single ammonia molecule adsorbed on a Ti site, experimentally a heat of adsorption of 66 $kJmol^{-1}$ was reported,[19] whereas the computational results largely underestimated such value, showing Binding Energies (BE) in the 25-40 $kJmol^{-1}$ range.[23,24] Similar computational results arose from both cluster or periodic approaches, indeed testifying that the energy mismatch can't be ascribed to the confinement effect experienced by the adsorbate within the porous system. The interaction discrepancy has thus to be ascribed to a different origin: an important ingredient missing in the previous approaches was the inclusion of dispersive forces, which relevance toward the correct evaluation of interaction energies for small molecules over oxides (and thus zeolites) have been largely demonstrated.[26–34] Therefore, before entering the study of NH_3/H_2O adsorption over Ti-CHA, a careful evaluation of the role of dispersive forces was performed: such fundamental study was performed on the Ti-CHA+NH_3 monoadduct.

Dispersive forces can be included in the calculation through two main approaches: i) as already mentioned, exploiting a semiempirical scheme likewise the Grimme's ones;[11,35,36] ii) through a fully *ab initio* description involving correlated methods, such as Møller-Plesset perturbation theory or Coupled Cluster, able to properly describe the long-range electron correlation (the quantum mechanical origin of dispersive forces).[37–39] Because of the high computational cost and/or implementation issues, the latter can't be straightforwardly applied to the large Ti-CHA supercell periodic model, therefore a convenient strategy can be represented by an ONIOM scheme.[40] In this approach (specifically an ONIOM2 scheme), the system is partitioned in two distinct layers: an inner part, containing the site of interest for the simulation (the so called model region), and the whole system (labeled as real model). For obvious reasons, the model region is treated with a higher level of theory (being so defined as High Model, HM), whereas for the real layer a less costly method (Low Real, LR) can be used. The final ONIOM energy can be computed as:

$$BE(ONIOM) = BE(LR) - BE(LM) + BE(HM) \qquad (5.3)$$

In order to properly compute the ONIOM energy, the contribution from the model region calculated at the low level method (Low Model, LM) is included in Equation 5.3. Regarding the Ti-CHA(+NH_3) models, the whole periodic system was selected as LR layer: the calculations were performed as previously discussed, but this time not including the dispersive forces. In the Ti-CHA+NH_3 adduct, the basis sets for the description of the N and H atoms of ammonia were an Ahlrichs TZV(2d) respectively Ahlrichs TZV respectively.[15] Different model regions of increasing size were instead considered: this choice was based on the achievement of the energy convergence of the purely electrostatic contributions for the clusters to the periodic energy. Furthermore

dispersive forces are strongly dependent on the system size, indeed a variable-size model region is interesting toward the evaluation of their effect.[41] The seven model regions adopted are schematized in Figure 5.2.

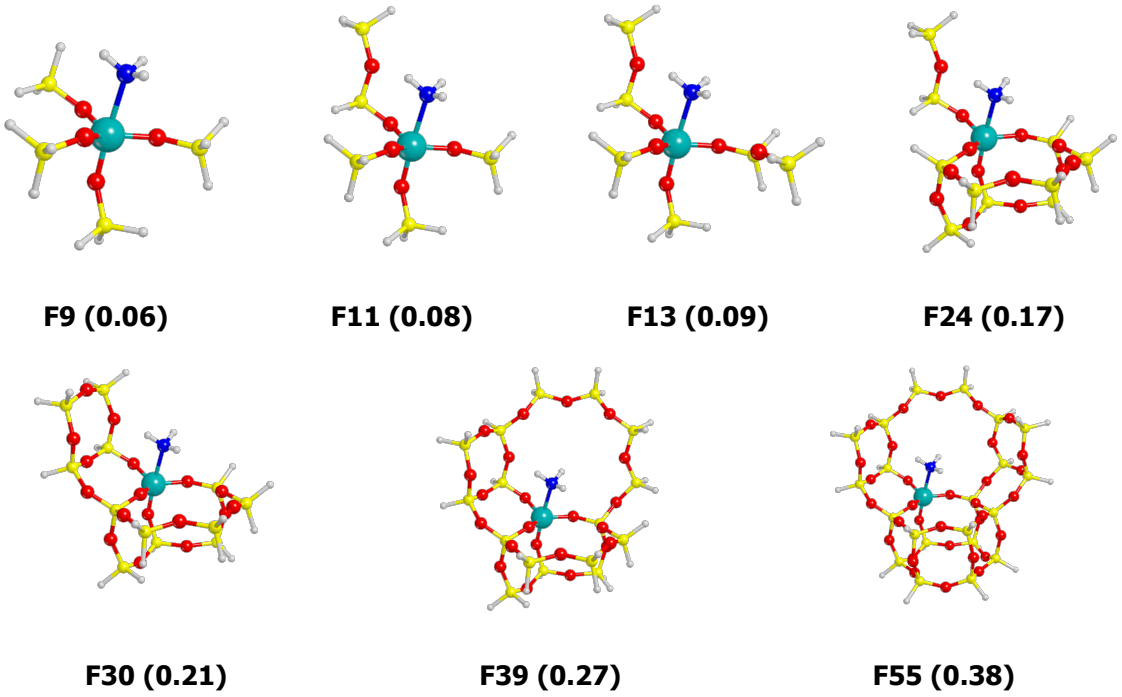

Figure 5.2 Ball and stick representation of the seven model regions exploited in the ONIOM calculations. In the brackets, the fraction of atoms included in the model region with respect to the Low Real layer (χ) are reported.

The dangling bonds on Si centers were saturated by hydrogen atoms, placed at a fixed distance of 1.45 Å along pristine Si – O bonds. HM calculations on the model clusters were performed through B3LYP, B3LYP-D and MP2 methods. The B3LYP, B3LYP-D calculations on all the clusters and the MP2 ones on clusters from F9 to F24, were performed exploiting the Gaussian09 code.[42] The NWChem[43] code was preferred to run the MP2 calculations on the three bulkier clusters (F30, F39, F55), in order to exploit the massive parallelization offered by the software. All the MP2 calculations were limited to the valence electrons. A Dunning aug-cc-pVQZ basis set[44] was chosen for anions (O and N), an Ahlrichs TZV(p)/TZV(d) for cations (Ti/Si)[15] and a Pople

6-311++G(2p,2d) for H atoms.[45] All the G09/NWChem default computational parameters were used in the calculation. LM calculations on the model region were performed exploiting the CRYSTAL14 code, at the B3LYP level and with the same parameters used for the periodic calculations. The full set of results obtained through the ONIOM approach are part of recently published paper, attached to this thesis as Appendix D: such paper was also selected for the cover of the issue.[46] In the following, only the key steps will be discussed: in detail, a schematic view of the outcomes is given in Figure 5.3, where the BSSE corrected Binding Energies (BE^c) are reported as a function of the model region size.

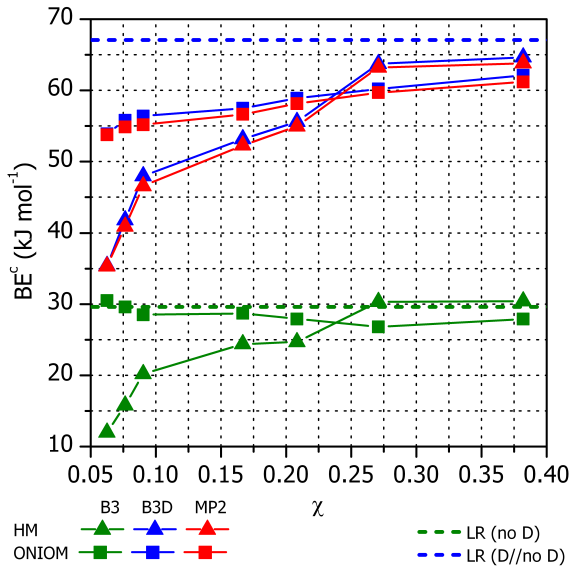

Figure 5.3 High Model (HM) and ONIOM BE^c *vs* the fraction of real atoms included in the model region with respect to the low real model (χ), computed at the B3LYP (B3), B3LYP-D (B3D) and MP2 levels. The BE^c computed for the Low Real (LR) periodic model without including dispersions (no D) and adding them *a posteriori* (D//no D) are reported as reference values.

Concerning the B3LYP calculations, the BE^c rapidly converges to the value calculated for LR (no D) model: first the major electrostatic contributions are included leading to a fast increase of BE^c, whereas this growth is slower adding to the model region atoms farer from the Ti site. Unexpectedly, the

BE^c(HM) values for the larger clusters are found to be higher than the corresponding BE^c(ONIOM). This behavior is probably related to a bad compensation of the two layers; however it is worth to underline that also in these cases the energy difference between BE^c(HM) and BE^c(ONIOM) is below 3 $kJmol^{-1}$, a significantly small value thus allowing a proper comparison with the experimental values. Since dispersive forces are not included, the Ti-CHA - NH_3 interaction energy is underestimated in agreement with the previous litereature.[23,24] The situation totally changes as dispersions are included either empirically (B3LYP-D) or *ab initio* (MP2): a significant increase of the BE^c is observed in both cases, already with the smaller clusters. The difference between the BE^c(HM) computed at B3LYP-D//$B3LYP_{CRY}$ and at B3LYP represents the purely dispersive contribution to the Binding Energy: the value of 23.4 $kJmol^{-1}$ obtained for the smaller cluster (F9) reaches the 34.3 $kJmol^{-1}$ for the bigger one (F55), with an increase of 10.9 $kJmol^{-1}$. By comparison, the dispersive contribution calculated on the BE^c(LR) is 37.5 $kJmol^{-1}$: such result demonstrates that the F55 fragment is sufficiently big to take into account the 91% of the total dispersive contribution, indeed effectively describing the NH_3 adsorption on Ti-CHA (even with a cluster approach). The results achieved by MP2 method are of the same magnitude of B3LYP-D (being the BE^c in average 0.5 $kJmol^{-1}$ lower), thus confirming the reliability of the semiempirical accounting of dispersions.

Since the central role of dispersive interactions (as well the reliability of their semiempirical evaluation through the Grimme GD2 scheme) was demonstrated, they were systematically included in the adsorption calculation reported hereafter. As previously mentioned, the adsorption of NH_3 and H_2O was studied, considering for both molecules a single and a double coverage of the Ti site. The principal outcomes of the calculations are listed in Table 5.4. The first important information is related to the cell volumes: as previously discussed, the insertion of Ti in the CHA siliceous framework leaded to a

realistic increase of the volume of 0.8%. Furthermore, the volume changes upon adsorption are rather small, with the only exception of the double NH_3 adsorption: in the latter case the volume is surprisingly reduced down to the values of the bare CHA.

Table 5.4 Main geometrical features (cell volumes, average Ti-O distances and Ti-Ligands distances) and BSSE corrected Binding Energies (BE^c), Deformation Energies (DE) and Binding Energies for the already deformed monomers (BE^{defc}) for the considered periodic models. Distances are given in Å, angles in °, volume in $Å^3$, energies in $kJmol^{-1}$.

Model	Volume	<Ti – O>	Ti – L^1	Ti – L^2	BE^c	DE	BE^{defc}
CHA	3180	-	-	-	-		
Ti-CHA	3204	1.799	-	-	-		
Ti-CHA							
+ H_2O^1	3208	1.820	2.379	-	50.8	-35.8	86.7
+ H_2O^2	3201	1.850	2.263	2.330	45.7	-32.2	78.0
Ti-CHA							
+ NH_3^1	3202	1.829	2.328	-	69.6	-48.3	118.0
+ NH_3^2	3183	1.861	2.343	2.307	52.2	-62.4	114.6

Looking at the local environment of Ti upon adsorption, the Ti-O average distance is significantly close to the experimental values: in the case of ammonia, the double adduct shows a better agreement with the EXAFS data (1.88 Å)[19,20]; conversely for water the better result is achieved by the single adduct (experimental distance: 1.82).[19,25] However, the general description of the Ti-site local environment is quite reliable and phenomenologically sound. Considering the Ti – L distances, in the case of H_2O a peculiar behavior is observed when the second molecule is adsorbed on the site: in fact the Ti – L^1 distance is reduced, becoming smaller than the Ti – L^2 one. This result can be explained considering the formation of a hydrogen bond among the first ligand and a framework oxygen atom, following the framework deformation induced

by the second adsorption. Conversely for NH_3 a slight increase of Ti – L^1 is observed upon the second adsorption, whereas the Ti – L^2 is shorter than the previous: in this case the second adsorption induces a sudden change in the system, as also the unexpected volume reduction suggests. The addition of a second NH_3 molecule is probably able to significantly detach the Ti from the framework, as the considerable increase in the average Ti-O distances testifies. The framework response to this "detachment" is represented by a partial recovery of its original, siliceous structure as the volume contraction to values proper of CHA model suggests. Further insights arose from energetic considerations: additionally to the Binding Energies, also the Deformation Energies (DE) and the Binding Energies for the already deformed monomers (BE^{defc}) were computed. The relation among the three energetic values is given in Equation 5.4.

$$BE^c = DE + BE^{defc} \tag{5.4}$$

The former takes into account the energy cost of the monomers deformation while forming the adducts, the latter represents the pure interaction contribution to the BE^c (since the deformation contribution is subtracted). The obtained BE^c values were compared with experimental results: it is worth to underline as a proper comparison should be performed with calculated enthalpies, thus requiring a full frequency calculation in order to estimate the zero point energy, the thermal energy and the *pV* contributions. This type of calculation is extremely demanding in terms of computational resources, since the vibrational frequency have to be determined numerically within the CRYSTAL14 code. Therefore, in first approximation, the comparison of experimental heats of adsorption with computed BE^c has been considered satisfactory. Anyway the BE^c values quantitatively approached the calorimetric data: referring to the data of Bolis and coworkers on NH_3 adsorption,[19,20] a

heat of adsorption of 66 $kJmol^{-1}$ is expected for a single adsorption whereas a slightly lower one (55 $kJmol^{-1}$) is ascribed to the second on. The computed binding energies (69.6 $kJmol^{-1}$ for single and 52.2 $kJmol^{-1}$ for double adsorption respectively) are for the first time approaching the experimental values. Similarly, the value expected for water adsorption (of about 50 $kJmol^{-1}$) is correctly reproduced.[47]

Considering the DE and BE^{defc}, as already commented in relation to geometrical parameters, the trends observed for water and ammonia adsorption are substantially different. For H_2O both DE and BE^{defc} decrease upon the second adsorption: the first molecule causes the major deformation of the framework and strongly interacts with the Ti, whereas the second one requires lower deformation energy but also interacts weaker. For NH_3 the second adsorption conversely produces a larger DE: since the Ti moiety moves to "quasi-extraframework" position, the whole zeolite framework is partially reconverted to a pure-siliceous like structure. Furthermore the second NH_3 molecule stabilizes the new local structure of the Ti: the BE^{defc} computed upon the second adsorption is in fact only slightly reduced with respect to the one of the first adsorption.

A more sophisticated test was performed considering the adsorption of two more complex organic molecules: acetonitrile and acetone. In particular, the use of the nitrile and the carbonyl moieties as vibrational probes was investigated: these functional groups, thanks to their slight basicity, can interact with Lewis acid sites (*i.e.* Ti ones). As the molecules are adsorbed, the C≡N and the C=O bonds are polarized, thus the related vibrational modes are perturbed becoming a clear fingerprint for the type of involved Lewis site. The adsorption of such molecules probed by vibrational spectroscopies (usually FTIR) is indeed a powerful technique in surface characterization of acid materials. The coupling of experimental with simulated data is furthermore really informative, since it makes possible a precise interpretation of

experimental data. The adsorption of a single molecule of acetonitrile/acetone on the Ti site of Ti-CHA was thus performed: as for water and ammonia, the adsorbate were described by an Ahlrichs TZV(2d) basis set (TZV for H).[15] The structures were relaxed and vibrational frequencies were then computed: since the moieties of interest for vibrational simulation are the adsorbates, a fragment approach including the molecules was exploited in order to reduce the computational cost. The comparison of the experimental results obtained on TS-1 through FTIR spectroscopy and the computed frequency shifts is outlined in Figure 5.4.

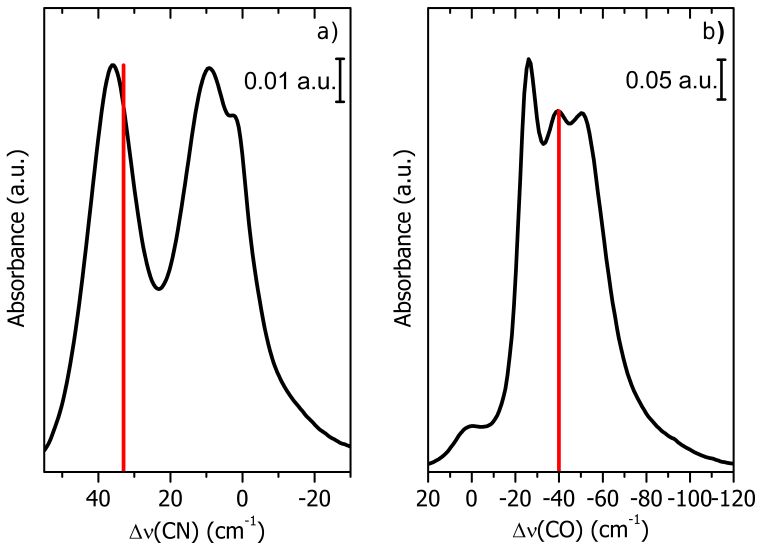

Figure 5.4 FTIR spectra (black lines) of a) acetonitrile; and b) acetone adsorbed on TS-1 from vapor phase. The zero of frequency scale was set in correspondence of the signals from the gas phase, isolated molecules (acetonitrile 2265 cm^{-1}, acetone 1745 cm^{-1}). The red vertical bars show the calculated shifts (with respect to the isolated molecules) from B3LYP-D simulations.

The computed peak shifts for the C≡N and C=O stretching modes are in good agreement with the experimental findings: in the case of acetonitrile the simulated shift of +33 cm^{-1} closely approaches the measured value of +37 cm^{-1}, also improving the quality of computational prevision with respect to previous studies.[48] The other features observed upon acetonitrile adsorption are instead ascribed to the physisorbed molecule (no shift) and to the

molecule interacting with hydroxyl groups (+11 cm^{-1}),[48] indeed not described by the model employed in the calculation. The case of acetone is less trivial to be commented, since specific data on TS-1 are not reported in the literature. However, a number of studies dealt with metal sites supported on silica (*e.g.* Zr, which is expected to show a behavior ascribable to the Ti one), demonstrating that shifts in the order of -40-50 cm^{-1} can be assigned to the interaction of acetone with these Lewis acid sites.[49,50] The calculation showed a good agreement with a component of the complex spectrum reported in Figure 5.4b, showing a shift of -40 cm^{-1} (equal to the calculated value). Concerning the other signals, the band at -26 cm^{-1} can be ascribed to the liquid-like acetone condensing in the zeolite pores, whereas the maximum shifted of -50 cm^{-1} can be compatible with acetone adsorbed on hydroxyls.[51,52]

The dataset of geometrical and energetic results obtained upon adsorption of NH_3 and H_2O, as well as the simulation of vibrational properties of adsorbed acetonitrile and acetone, demonstrates the reliability of Ti-CHA as model system for the most complex TS-1. Because of this, the model was exploited for the evaluation of other properties, mostly related to the TS-1 spectroscopy: in particular vibrational and electronic features were evaluated.

5.3 Modeling the TS-1 spectrocopic features through the Ti-CHA model: vibrational and electronic properties

In Chapter 4 the peculiar spectroscopic fingerprints of TS-1 have been introduced and widely discussed. From the computational side, the possibility to simulate these observables is really interesting since modeling can be exploited in order to shed light on the open questions related to the Ti speciation in defective TS-1 samples. The first step was however to model the spectroscopic properties of the perfect Ti-CHA model: in this regard, the comparative view with the siliceous CHA is really informative. The calculated

Raman spectra and the bands schemes (accounting for electronic properties) for CHA and Ti-CHA are compared in Figure 5.5.

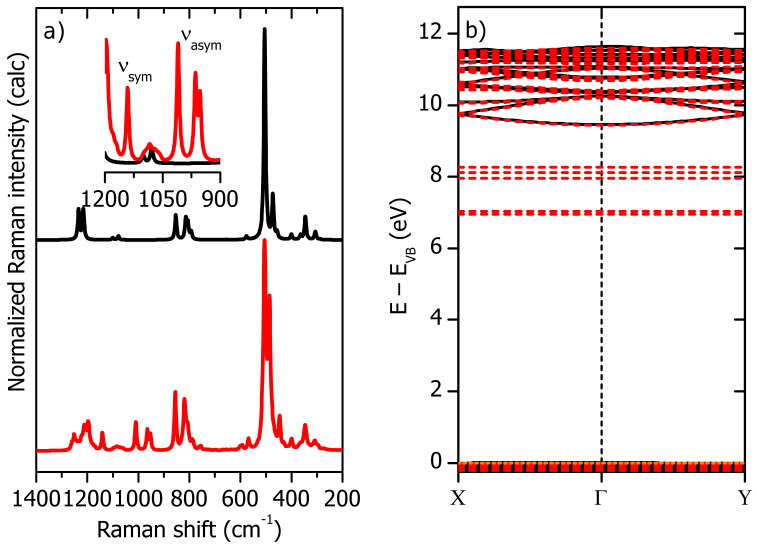

Figure 5.5 Calculated a) Raman spectra; and b) bands structure of CHA (black lines) and Ti-CHA (Si/Ti = 47, red lines). The dotted orange line in the band diagrams shows the position of the Fermi level.

The vibrational datum is in line with experimental expectations:[6] the bare CHA presents the typical Raman features of a zeolite, showing in the low frequency region a doublet of sharp peaks typical for its specific topology (ascribed to the collective vibrations of the 4- and 6- members rings of sodalite building blocks) and at higher frequencies the fingerprints of symmetric (~ 800 cm^{-1}) and antisymmetric (~ 1200 cm^{-1}) Si-O-Si stretching modes. As Ti is inserted these features are mostly unaltered in terms of frequency shift, whereas relative intensities are more affected: the latter fact can be probably ascribed to the different symmetry adopted in the calculation of the CHA ($R\bar{3}m$) and Ti-CHA ($P1$), indeed resulting in a different polarization tensor for the siliceous portion of the materials. However the major difference, as underlined in the inset of Figure 5.5a, is the appearance of four peaks in the 1200-900 cm^{-1} region: these are straightforwardly ascribed to the vibrational modes of Ti-O-Si

stretchings.[53] In detail, the bunch of bands with barycenter at 970 cm^{-1} is assigned to the antisymmetric stretching modes (experimentally expected at 960 cm^{-1}), whereas the symmetric one generates the peak 1130 cm^{-1} (being its experimental frequency 1090 cm^{-1}). Even if an overestimation of the vibrational frequencies is observed, the interpretation of the computed spectrum is univocal. Moving to the electronic features (Figure 5.5b), both CHA and Ti-CHA valence and conduction bands are superimposed along the simple path chosen in the simulation. The bands schemes have been aligned to the top of the Valence Band states, belonging to framework oxygen atoms, in order to facilitate the comparative view of the band diagrams. The key difference is observed close to the bottom of conduction band, where 5 states are located upon Ti insertion. Considering the absence of dispersion along the path, these can be assigned to the localized *d* orbitals of Ti, also showing the expected e-t_2 splitting for a tetrahedral ligands field. Owning the band structure, it is really interesting to infer the origin of the peculiar electronic transition related to the tetrahedral Ti center: this is typically described in the literature as a Ligand to Metal Charge Transfer (LMCT) from the oxygen atoms bonded to the Ti toward the metal site.[47,54,55] Looking at the band diagram, however, the top of the valence band is rich of states: in order to clearly assign them, the DOSS (projected for the Ti and its neighbor O) was computed. The result is shown in Figure 5.6. The isolated states observed just below the conduction band are univocally ascribable to Ti as previously inferred, whereas some interesting consideration can be stated on the role of the neighbor O atoms according to their projected DOSS: these are (even if only partially contributing) to determine the DOSS at the top of the valence band. Thereby the possibility to have a molecular-like LMCT transition from O surrounding the Ti to the metal center is possible according to the model. However, taking into account the mismatch between the total DOSS and the

projected one on Ti first neighbors, the contribution of more distant O atoms cannot be excluded *a priori*.

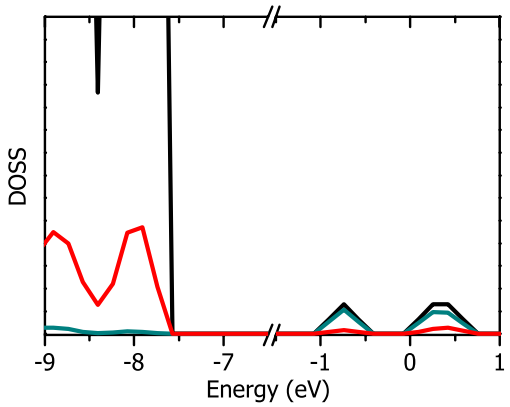

Figure 5.6 Total DOSS (black line) for the bare Ti-CHA and its projected components for Ti (cyan line) and its four neighbor O (summed together, red line).

In order to quantitatively analyze the electronic properties of CHA and Ti-CHA, a crude estimation of the band gaps was performed considering a vertical transition among the valence band and the lowest unoccupied state: the lower energy band gaps computed through this approach are 9.46 eV for CHA and 6.96 eV for Ti-CHA respectively. In comparison with experimental values (5.3 eV, available only for Ti-CHA), the computed gaps are largely overestimated: according to Harrison and coworkers,[56] B3LYP is expected to give a much better description of band gaps for common semiconductors, with an average error of 0.3 eV (*vs* a mismatch of 1.7 eV achieved through the calculation on Ti-CHA). The reasons for this deviation could be various, arising from both computational and/or experimental issues. With respect to the simulation, it is worth to underline that the present calculation have been performed including dispersive forces, not accounted for Ref. 56: since geometries can vary significantly upon the inclusion of the dispersive term, the band gaps prediction capability of B3LYP could be altered in a relevant extent. Furthermore the band gap evaluation based on vertical transitions is rather

rough, since it doesn't take into account the relaxation of electronic structure upon excitation: if this is pronounced for Ti-CHA (more than for the semiconductors studied by Harrison), the computed property will be poorly descriptive of the real system. Another issue is that a correct experimental evaluation of the band gap for TI-CHA is possibly biased by the closeness of its optical absorption to the upper limit (in terms of energy) of the measurable region in conventional instruments. The apparently peaked shape of the band can be ascribed to the loose in efficiency of the detector while progressively entering the UV region, indeed the maximum of the absorption could be locate at higher energies (inaccessible with laboratory equipment). In this regard, an experimental proposal has been submitted to the Elettra Synchrotron: the purpose of the experiment will be the evaluation of the optical properties of Ti-CHA and TS-1 in the vacuum-UV energy range (below 200 nm, above 6 eV) exploiting the features of the BEAR beamline (CERIC proposal n. 20167001, "Vibrational, electronic and structural characterization of Ti-zeolites with increasing defectivity").[57]

From these preliminary tests, vibrational properties seem to be more suitable in the identification of Ti species through simulation with respect to electronic, band gaps based ones. However, always taking into account the considerable size of the model, some considerations on the computational cost of the two strategies are compulsory. The calculation of vibrational frequencies is in fact very demanding in terms of computational resources: in the example showed here, the calculation of the Raman spectrum starting from the optimized Ti-CHA model required about 42000 CPU hours to be completed. Conversely, the presented calculation of band structure (involving 60 point along the selected path and 50 crystalline orbitals) requires only 55 CPU hours, indeed being an almost costless method. Moreover, as will be readily shown, the band gap data can be interpreted in relative terms rather than in absolute ones, giving thus a realistic description of the Ti-CHA system transformations.

In this regard, the effect of water and ammonia adsorption on the band gap was evaluated in comparison to experimental data: the set of results is reproduced in Figure 5.7.

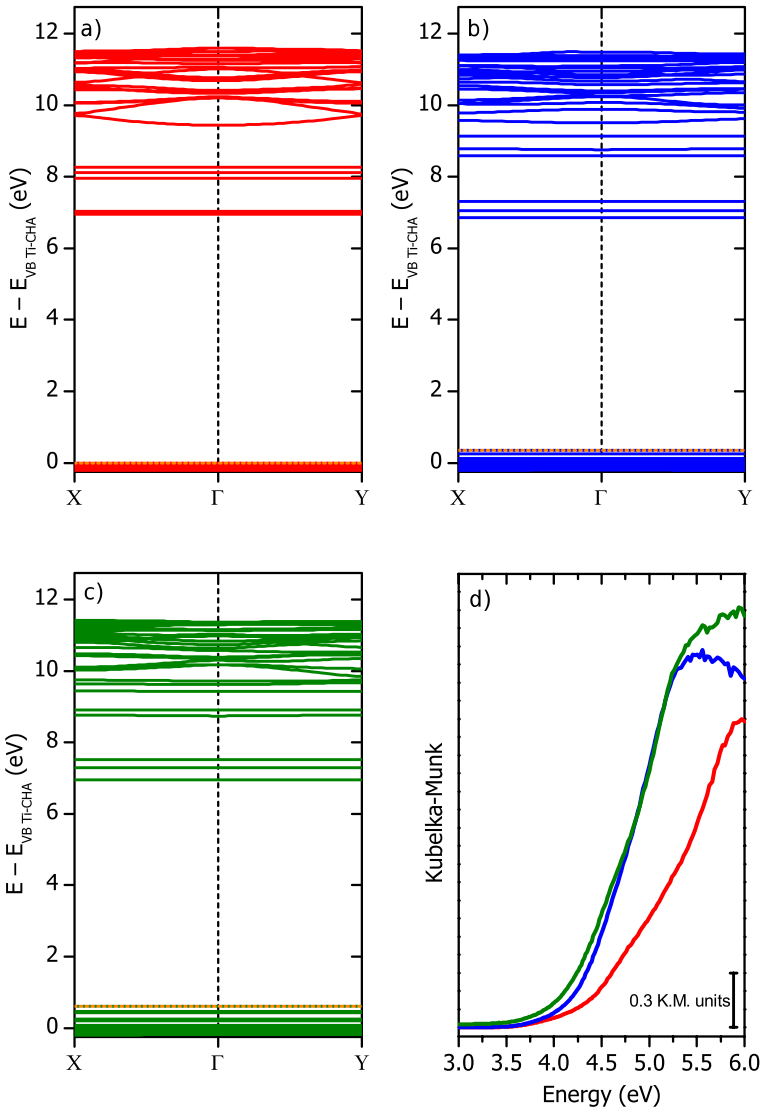

Figure 5.7 Bands structure of: a) bare Ti-CHA; b) Ti-CHA+2H_2O; and c) Ti-CHA+2NH_3. In panel d) the experimental optical spectra of Ti-CHA as such (red line) and contacted with excess water (blue line) and ammonia (green line) are reported. The dotted orange line in the band diagrams shows the position of the Fermi level.

The band structures were computed only for the maximum coverage (*i.e.* two molecules per Ti site) models, in order to have a proper comparison with the experimental data. The adsorption processes lead to a clear modification of

the band structure: first of all, the levels ascribed to titanium *d* orbitals changes, as the coordination sphere of the Ti site is modified from tetrahedral to octahedral, as explained by crystal field theory. Also the Δ_T and Δ_O values (the energy splitting among the *e*-t_2 and the t_{2g}-e_g orbitals respectively) consistently increases, *e.g.* from $\Delta_T = 1.12$ eV (Ti-CHA) to $\Delta_O = 1.61$ eV (Ti-CHA+2H_2O) in the case of water adsorption. However the theoretical ratio Δ_T / $\Delta_O = 0.444$ (4/9) is not achieved, resulting to be about 0.69. This means that the octahedral stabilization cannot be completely reached, probably according to the big distortion of the coordination sphere (the Ti–Ligand distance is ~ 0.5 Å longer than the Ti–O one). Interestingly, also the valence band revealed a relevant perturbation upon adsorption: some isolated stated are clearly introduced on top of the dense band formed by the framework O states, which are simultaneously destabilized with respect to the bare Ti-CHA. The isolated states can be ascribed to the presence of the HOMO levels of the adsorbed molecules, on the basis of the Density Of States (DOSS) diagrams reported in Figure 5.8.

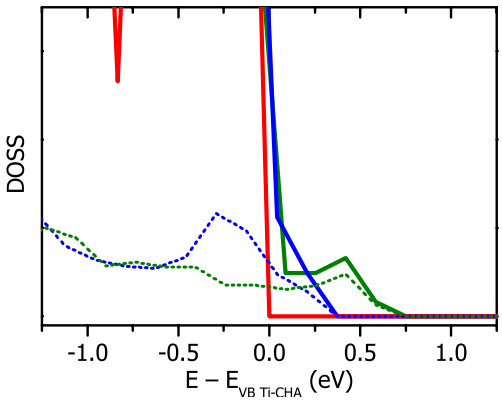

Figure 5.8 Total DOSS (solid lines) for the bare Ti-CHA (red line), Ti-CHA+2H_2O (blue line) and Ti-CHA+2NH_3 models at the top of valence band. The dotted lines represent the projected DOSS for the ligands anions (O, blue line, or N, green line).

The experimental red-shift of adsorption bands of Ti-CHA upon adsorption of basic molecules is thus ascribable to the narrowing of the band gap

consequent to the complex rearrangement of the energy levels upon adsorption. The stabilization of the *d* states of Ti, the destabilization of the valence band O states and the introduction of molecular levels on top of the latter are acting together in this direction.

Moving to more quantitative considerations, the simulated band gaps (evaluated as vertical transitions at the Γ point) were compared with the experimental ones extrapolated from optical absorption measurements through the Tauc plot method for direct band gaps.[58] As in the case of bare Ti-CHA previously discussed in this chapter, the direct comparison of absolute band gap values is not meaningful since the values from simulations are largely overestimating the observable property: therefore a relative comparison has been performed, considering the extent of the band gap red-shift upon adsorption for both experimental and simulated data. The results of such approach are reported in Table 5.5.

Table 5.5 Simulated *vs* experimental band gaps (E_g) for Ti-CHA and its H_2O and NH_3 biadducts. The shifts of the absorption edge upon adsorption (ΔE_g) are reported as well.

	Ti-CHA	$+2H_2O$	$+2NH_3$
E_g calc (eV)	6.96	6.51	6.34
E_g exp (eV)	5.3 ± 0.2	4.8 ± 0.1	4.8 ± 0.1
ΔE_g calc (eV)		-0.45	-0.62
ΔE_g exp (eV)		-0.5 ± 0.2	-0.5 ± 0.2

The agreement of the simulated band gaps variations upon adsorption with experimental ones is rather good: the computed values are in fact included in the error bar of measured ones. Thereby, even if through a rough methodology, the band gap shift related to Ti species (with respect to the perfect tetrahedral one) are a reliable marker in the assignment of experimental electronic transitions to a supposed structural model.

According to this last possibility, the same methodology was applied to some hypothetical Ti defective structures in order to (eventually) assign the origin of the defects electronic transitions to a given structure: in fact, as extendedly discussed in Chapter 4, some real samples show peculiar families of defective Ti sites with well defined optical properties. In particular, in relation to the available set of samples, an important feature is the electronic transition falling at 270 nm (4.59 eV), which structural origin is still object of debate. As already inferred by experimental works, this optical absorption could be ascribed to a Ti moiety showing a higher coordination with respect to the perfect tetrahedral sites, *i.e.* penta- or octahedral.[5,54,59–61] The simplest models of higher coordination Ti sites can result from the breaking of Ti-O framework bonds and the addition of water molecules, giving rise to a titanol and a silanol (still interacting with the Ti site) for each Ti-O bond broken. Pentahedral coordination can be achieved by breaking a single Ti-O bond, whereas double breaking leads to the octahedral structure. The local environment of Ti in such models is sketched in Figure 5.9.

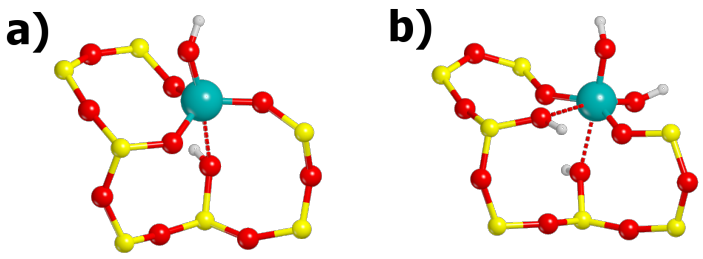

Figure 5.9 Structures of hypothetical Ti defective sites with higher coordination, obtained through a) single and b) double hydrolysis of the perfect tetrahedral site.

The two defective structures described above were introduced in the supercell model previously presented and geometry relaxation was performed: these will be labeled as Ti(OH)-CHA and $Ti(OH)_2$-CHA respectively. The stability of the defective structures was evaluated computing the energy for their conversion

in the correspondent Ti-CHA+$n$$H_2O$ adducts (being n = 1 for Ti(OH)-CHA and n = 2 for $Ti(OH)_2$-CHA), *i.e.* the hypothetical reaction of Ti-O-Si bridge(s) closure upon H_2O elimination occurring during the Ti-zeolite synthesis. The reaction schemes adopted are the following:

$$\mathrm{Ti(OH)\text{-}CHA} \rightarrow \mathrm{Ti\text{-}CHA} + \mathrm{H_2O_{add}} \quad (5.4)$$

$$\mathrm{Ti(OH)_2\text{-}CHA} \rightarrow \mathrm{Ti\text{-}CHA} + 2\mathrm{H_2O_{add}} \quad (5.5)$$

Thus the reaction energies are computed as:

$$\Delta E_{penta} = E(\mathrm{Ti\text{-}CHA} + \mathrm{H_2O_{add}}) - E(\mathrm{Ti(OH)\text{-}CHA}) \quad (5.6)$$

$$\Delta E_{octa} = E(\mathrm{Ti\text{-}CHA} + 2\mathrm{H_2O_{add}}) - E(\mathrm{Ti(OH)_2\text{-}CHA}) \quad (5.7)$$

The computed values for ΔE_{penta} and ΔE_{octa} were -33.8 kJmol^{-1} and -97.7 kJmol^{-1} respectively: the existence of both structure is thus rather improbable according to the energetic information only, since the Ti-CHA+$n$$H_2O$ adducts are more stable than the considered defects. However, as already mentioned in this chapter, a proper energetic evaluation must be performed through thermodynamic functions, *i.e.* the enthalpy or the Gibbs's free energy. Furthermore the simulated reactions don't take into account the complexity of the synthetic environment: TS-1 synthesis is in fact performed in hydrothermal conditions, thus under high temperature/pressure and in presence of excess water and other possible ligands (bases, templating agents).[62] Thereby, even preliminary data suggest these defects to be thermodynamically unstable, their formation under harsh conditions (and/or driven by kinetic forces) cannot be excluded *a priori*. The electronic features of the defective structures were computed: the corresponding band diagrams are reported in Figure 5.10. The creation of the defect, followed by the change in the ligand field of Ti, is accomplished by the expected swap in the order of the *d* orbitals: in the pentahedral defect the band gap is slightly affected by this, whereas in the

octahedral one the lowest unoccupied *d* orbital rises in energy with respect to the perfect site. However, a number of states are introduced on the top of the valence band, helping in sharpening the gap.

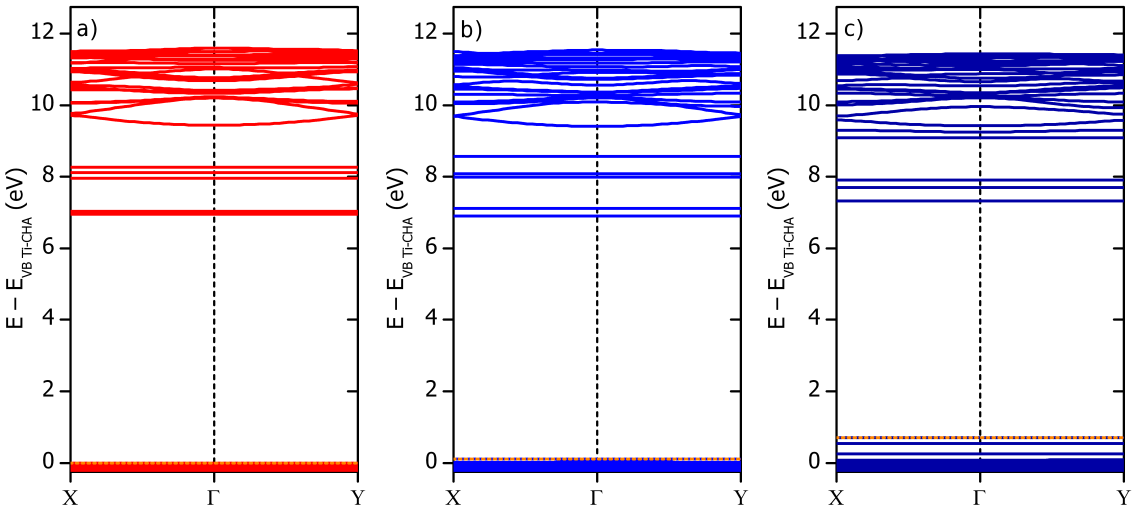

Figure 5.10 Bands structure of: a) bare Ti-CHA; b) TiOH-CHA; and c) $Ti(OH)_2$-CHA. The dotted orange line in the band diagrams shows the position of the Fermi level.

Coming to quantitative considerations, the calculated vertical band gaps at the Γ point are 6.80 eV and 6.63 eV for the penta- and the octahedral defects respectively. This means that the gap shifts with respect to the perfect site are -0.16 eV and -0.33 eV: in comparison with the experimental value (-0.80 eV), these values are rather small, thus most probably the proposed structures do not represent the real defective site.

Since the isolated defective sites did not allowed to explain the origin of the peculiar electronic transition, thereby a model based on polymerized Ti species was chosen. In detail, a convenient structure was found in the ETS-10 zeolite, a wide porosity material which main peculiarity is the presence in the structure of polymerized octahedral Ti linear chains.[63,64] The residual negative charge of the framework is balanced by extaframework cations (typically Na^+ and/or K^+). This structure can represent a particular model of defect with

chained Ti species and, interestingly, it posses an optical absorption peaked at 4.4 eV, relatively close to the defect one showing a maximum at 4.59 eV. In particular, such electronic transition was related to the Ligand to Metal Charge Transfer (LMCT) from O to Ti along the direction parallel to the octahedral Ti chain, indeed being delocalized and red-shifting with respect to isolated species.[65] The ETS-10 (Na^+ form) structure was relaxed and the band structure was simulated: results are reported in Figure 5.11.

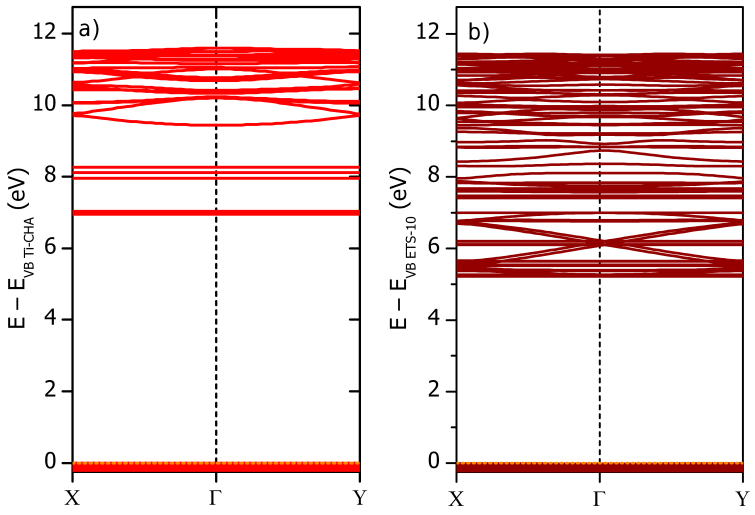

Figure 5.11 Bands structure of: a) Ti-CHA; and b) ETS-10. The dotted orange line in the band diagrams shows the position of the Fermi level.

According to the band structure, ETS-10 shows a narrower band gap, calculated to be 5.24 eV. Again the transition red-shift with respect to the perfect Ti sites of TS-1 was computed, giving a value of -1.72 eV: even if the agreement with the experimental datum (-1.42 eV) is somehow less good with respect to the small molecules adsorption case, however it is reasonable taking into account that two different models are compared. The key information from ETS-10 band gap is furthermore relevant in terms of comparison with defective sites: the periodic octahedral Ti chains give rise to an electronic transition characterized by relevantly lower energy, falling in the neighborhood

of the defects one. Thereby the correct structural model for defects could be represented by confined chains of Ti polyhedra, or maybe by kind of titania clusters. Reducing the dimensionality, the consequent quantum confinement will result in a lower red shift of electronic transitions, thus closely relating to the defective species experimentally observed. The construction of new defect models, based on the findings of this preliminary study, will represent the natural continuation of such research line: as the right structures will be obtained, the final crosscheck will be represented by the calculation of their vibrational properties, indeed more precise in confirming the goodness of the adopted models.

References

(1) Ricchiardi, G.; de Man, A.; Sauer, J. The Effect of Hydration on Structure and Location of Ti-Sites in Ti-Silicalite Catalysts. A Computational Study. *Phys. Chem. Chem. Phys.* **2000**, *2* (10), 2195–2204.

(2) Montejo-Valencia, B. D.; Salcedo-Pérez, J. L.; Curet-Arana, M. C. DFT Study of Closed and Open Sites of BEA, FAU, MFI, and BEC Zeolites Substituted with Tin and Titanium. *J. Phys. Chem. C* **2016**, *120* (4), 2176–2186.

(3) Dong, J.; Zhu, H.; Xiang, Y.; Wang, Y.; An, P.; Gong, Y.; Liang, Y.; Qiu, L.; Zheng, A.; Peng, X.; et al. Toward a Unified Identification of Ti Location in the MFI Framework of High-Ti-Loaded TS-1: Combined EXAFS, XANES, and DFT Study. *J. Phys. Chem. C* **2016**, *120* (36), 20114–20124.

(4) Camblor, M. A.; Corma, A.; Pérez-Pariente, J. Synthesis of Titanoaluminosilicates Isomorphous to Zeolite Beta, Active as Oxidation Catalysts. *Zeolites* **1993**, *13* (2), 82–87.

(5) Blasco, T.; Camblor, M. A.; Corma, A.; Perez-Pariente, J. The State of Ti

in Titanoaluminosilicates Isomorphous with Zeolite Beta. *J. Am. Chem. Soc.* **1993**, *115* (25), 11806–11813.

(6) Eilertsen, E. A.; Bordiga, S.; Lamberti, C.; Damin, A.; Bonino, F.; Arstad, B.; Svelle, S.; Olsbye, U.; Lillerud, K. P. Synthesis of Titanium Chabazite: A New Shape Selective Oxidation Catalyst with Small Pore Openings and Application in the Production of Methyl Formate from Methanol. *ChemCatChem* **2011**, *3* (12), 1869–1871.

(7) Eilertsen, E. A.; Giordanino, F.; Lamberti, C.; Bordiga, S.; Damin, A.; Bonino, F.; Olsbye, U.; Lillerud, K. P. Ti-STT: A New Zeotype Shape Selective Oxidation Catalyst. *Chem. Commun.* **2011**, *47* (43), 11867–11869.

(8) Dovesi, R.; Orlando, R.; Erba, A.; Zicovich-Wilson, C. M.; Civalleri, B.; Casassa, S.; Maschio, L.; Ferrabone, M.; De La Pierre, M.; D'Arco, P.; et al. CRYSTAL14 : A Program for the *Ab Initio* Investigation of Crystalline Solids. *Int. J. Quantum Chem.* **2014**, *114* (19), 1287–1317.

(9) Becke, A. D. A New Mixing of Hartree–Fock and Local Density-Functional Theories. *J. Chem. Phys.* **1993**, *98* (2), 1372.

(10) Lee, C.; Yang, W.; Parr, R. G. Development of the Colle-Salvetti Correlation-Energy Formula into a Functional of the Electron Density. *Phys. Rev. B* **1988**, *37* (2), 785–789.

(11) Grimme, S. Semiempirical GGA-Type Density Functional Constructed with a Long-Range Dispersion Correction. *J. Comput. Chem.* **2006**, *27* (15), 1787–1799.

(12) Díaz-Cabañas, M.-J.; Barrett, P. A. Synthesis and Structure of Pure SiO_2 Chabazite: the SiO_2 Polymorph with the Lowest Framework Density. *Chem. Commun.* **1998**, No. 17, 1881–1882.

(13) Román-Román, E. I.; Zicovich-Wilson, C. M. The Role of Long-Range van Der Waals Forces in the Relative Stability of SiO_2-Zeolites. *Chem. Phys. Lett.* **2015**, *619*, 109–114.

(14) Nada, R.; Nicholas, J. B.; McCarthy, M. I.; Hess, A. C. Basis Sets for Ab Initio Periodic Hartree-Fock Studies of Zeolite/adsorbate Interactions: He, Ne, and Ar in Silica Sodalite. *Int. J. Quantum Chem.* **1996**, *60*, 809–820.

(15) Schafer, A.; Huber, C.; Ahlrichs, R. Fully Optimized Contracted Gaussian Basis Sets of Triple Zeta Valence Quality for Atoms Li to Kr. *J. Chem. Phys.* **1994**, *100* (8), 5829-5835.

(16) Weigend, F.; Ahlrichs, R. Balanced Basis Sets of Split Valence, Triple Zeta Valence and Quadruple Zeta Valence Quality for H to Rn: Design and Assessment of Accuracy. *Phys. Chem. Chem. Phys.* **2005**, *7* (18), 3297–3305.

(17) Available at: http://www.crystal.unito.it/Basis_Sets/titanium.html#Ti_86-411%28d31%29G_darco_unpub.

(18) Lamberti, C.; Bordiga, S.; Zecchina, A.; Carati, A.; Fitch, N. N.; Artioli, G.; Petrini, G.; Salvalaggio, M.; Marra, G. L. L. Structural Characterization of Ti-Silicalite-1: A Synchrotron Radiation X-Ray Powder Diffraction Study. *J. Catal.* **1999**, *183* (2), 222–231.

(19) Bolis, V.; Bordiga, S.; Lamberti, C.; Zecchina, A.; Carati, A.; Rivetti, F.; Petrini, G.; Spanò, G. A Calorimetric , IR , XANES and EXAFS Study of the Adsorption of NH on Ti-Silicalite as a Function of the Sample Pre-Treatment. *Microporous Mesoporous Mater.* **1999**, *30*, 67–76.

(20) Bolis, V.; Bordiga, S.; Lamberti, C.; Zecchina, A.; Carati, A.; Rivetti, F.; Spanò, G.; Petrini, G. Heterogeneity of Framework Ti(IV) in Ti–Silicalite as Revealed by the Adsorption of NH_3. Combined Calorimetric and Spectroscopic Study. *Langmuir* **1999**, *15* (18), 5753–5764.

(21) Blasco, T.; Camblor, M.; Corma, A.; Esteve, P.; Guil, J. M.; Martı, A.; Valencia, S.; Martinez, A.; Perdigon-Melon, J. Direct Synthesis and Characterization of Hydrophobic Aluminum-Free Ti-Beta Zeolite. *J. Phys.*

Chem. B **1998**, *102* (1), 75–88.

(22) Zicovich-Wilson, C. M.; Dovesi, R.; Corma, A. Interaction of Ti-Zeolites with Water. A Periodic Ab Initio Study. *J. Phys. Chem. B* **1999**, *103* (6), 988–994.

(23) Damin, A.; Bordiga, S.; Zecchina, A.; Lamberti, C. Reactivity of Ti(IV) Sites in Ti-Zeolites: An Embedded Cluster Approach. *J. Chem. Phys.* **2002**, *117* (1), 226–237.

(24) Damin, A.; Bordiga, S.; Zecchina, A.; Doll, K.; Lamberti, C. Ti-Chabazite as a Model System of Ti(IV) in Ti-Zeolites: A Periodic Approach. *J. Chem. Phys.* **2003**, *118* (22), 10183–10194.

(25) Bordiga, S.; Bonino, F.; Damin, A.; Lamberti, C. Reactivity of Ti(IV) Species Hosted in TS-1 towards H_2O_2–H_2O Solutions Investigated by Ab Initio Cluster and Periodic Approaches Combined with Experimental XANES and EXAFS Data: A Review and New Highlights. *Phys. Chem. Chem. Phys.* **2007**, *9* (35), 4854–4878.

(26) Kerber, T.; Sierka, M.; Sauer, J. Application of Semiempirical Long-Range Dispersion Corrections to Periodic Systems in Density Functional Theory. *J. Comput. Chem.* **2008**, *29* (13), 2088–2097.

(27) Tosoni, S.; Sauer, J. Accurate Quantum Chemical Energies for the Interaction of Hydrocarbons with Oxide Surfaces: CH_4/MgO(001). *Phys. Chem. Chem. Phys.* **2010**, *12* (42), 14330–14340.

(28) Włodarczyk, R.; Sierka, M.; Kwapień, K.; Sauer, J.; Carrasco, E.; Aumer, A.; Gomes, J. F.; Sterrer, M.; Freund, H.-J. Structures of the Ordered Water Monolayer on MgO(001). *J. Phys. Chem. C* **2011**, *115* (14), 6764–6774.

(29) Rimola, A.; Costa, D.; Sodupe, M.; Lambert, J. F.; Ugliengo, P. Silica Surface Features and Their Role in the Adsorption of Biomolecules: Computational Modeling and Experiments. *Chem. Rev.* **2013**, *113* (6), 4216–4313.

(30) Kumar, N.; Kent, P. R. C.; Wesolowski, D. J.; Kubicki, J. D. Modeling Water Adsorption on Rutile (110) Using van Der Waals Density Functional and DFT+U Methods. *J. Phys. Chem. C* **2013**, *117* (45), 23638–23644.

(31) Piccini, G.; Alessio, M.; Sauer, J.; Zhi, Y.; Liu, Y.; Kolvenbach, R.; Jentys, A.; Lercher, J. A. Accurate Adsorption Thermodynamics of Small Alkanes in Zeolites. Ab Initio Theory and Experiment for H-Chabazite. *J. Phys. Chem. C* **2015**, *119* (11), 6128–6137.

(32) Fischer, M. Water Adsorption in SAPO-34: Elucidating the Role of Local Heterogeneities and Defects Using Dispersion-Corrected DFT Calculations. *Phys. Chem. Chem. Phys.* **2015**, *17* (38), 25260–25271.

(33) Delle Piane, M.; Corno, M.; Orlando, R.; Dovesi, R.; Ugliengo, P. Elucidating the Fundamental Forces in Protein Crystal Formation: The Case of Crambin. *Chem. Sci.* **2016**, *7* (2), 1496–1507.

(34) Fischer, M. Interaction of Water with (Silico)aluminophosphate Zeotypes: A Comparative Investigation Using Dispersion-Corrected DFT. *Phys. Chem. Chem. Phys.* **2016**, *18* (23), 15738–15750.

(35) Grimme, S. Accurate Description of van Der Waals Complexes by Density Functional Theory Including Empirical Corrections. *J. Comput. Chem.* **2004**, *25* (12), 1463–1473.

(36) Grimme, S.; Antony, J.; Ehrlich, S.; Krieg, H. A Consistent and Accurate Ab Initio Parametrization of Density Functional Dispersion Correction (DFT-D) for the 94 Elements H-Pu. *J. Chem. Phys.* **2010**, *132* (15), 154104 1-19.

(37) Kristyán, S.; Pulay, P. Can (Semi)local Density Functional Theory Account for the London Dispersion Forces? *Chem. Phys. Lett.* **1994**, *229* (3), 175–180.

(38) Hobza, P.; Sponer, J.; Reschel, T. Density-Functional Theory and Molecular Clusters. *J. Comput. Chem.* **1995**, *16* (11), 1315–1325.

(39) Allen, M. J.; Tozer, D. J. Helium Dimer Dispersion Forces and Correlation Potentials in Density Functional Theory. *J. Chem. Phys.* **2002**, *117* (24), 11113–11120.

(40) Dapprich, S.; Komáromi, I.; Byun, K. S.; Morokuma, K.; Frisch, M. J. A New ONIOM Implementation in Gaussian98. Part I. The Calculation of Energies, Gradients, Vibrational Frequencies and Electric Field Derivatives. *J. Mol. Struct. THEOCHEM* **1999**, *461–462*, 1–21.

(41) Wagner, J. P.; Schreiner, P. R. London Dispersion in Molecular Chemistry - Reconsidering Steric Effects. *Angew. Chemie - Int. Ed.* **2015**, *54* (42), 12274–12296.

(42) Frisch, M. J.; Trucks, G. W.; Schlegel, H. B.; Scuseria, G. E.; Robb, M. A.; Cheeseman, J. R.; Scalmani, G.; Barone, V.; Mennucci, B.; Petersson, G. A.; et al. Gaussian 09 Revision D.03. *Gaussian 09 Revis. D.03* **2009**.

(43) Valiev, M.; Bylaska, E. J.; Govind, N.; Kowalski, K.; Straatsma, T. P.; Van Dam, H. J. J.; Wang, D.; Nieplocha, J.; Apra, E.; Windus, T. L.; et al. NWChem: A Comprehensive and Scalable Open-Source Solution for Large Scale Molecular Simulations. *Comput. Phys. Commun.* **2010**, *181* (9), 1477–1489.

(44) Dunning Jr, T. H. Gaussian Basis Sets for Use in Correlated Molecular Calculations. I. The Atoms Boron through Neon and Hydrogen. *J. Chem. Phys.* **1989**, *90* (1989), 1007–1023.

(45) Krishnan, R.; Binkley, J. S.; Seeger, R.; Pople, J. A. Self-Consistent Molecular Orbital Methods. XX. A Basis Set for Correlated Wave Functions. *J. Chem. Phys.* **1980**, *72* (1), 650–654.

(46) Cover Image, Volume 37, Issue 30. *J. Comput. Chem.* **2016**, *37* (30), i–i.

(47) Bordiga, S.; Damin, A.; Bonino, F.; Zecchina, A.; Spanò, G.; Rivetti, F.; Bolis, V.; Prestipino, C.; Lamberti, C. Effect of Interaction with H_2O and

NH_3 on the Vibrational, Electronic, and Energetic Peculiarities of Ti(IV) Centers TS-1 Catalysts: A Spectroscopic and Computational Study. *J. Phys. Chem. B* **2002**, *106* (38), 9892–9905.

(48) Bonino, F.; Damin, A.; Bordiga, S.; Lamberti, C.; Zecchina, A. Interaction of CD_3CN and Pyridine with the Ti(IV) Centers of TS-1 Catalysts: A Spectroscopic and Computational Study. *Langmuir* **2003**, *19* (6), 2155–2161.

(49) Crocellà, V.; Morterra, C. On the Ambient Temperature Gas–Solid Interaction of Acetone with Some Silica-Supported d^0 Metal Oxides. *J. Phys. Chem. C* **2010**, *114* (44), 18972–18987.

(50) Crocellà, V.; Cerrato, G.; Morterra, C. On the Adsorption/reaction of Acetone on Pure and Sulfate-Modified Zirconias. *Phys. Chem. Chem. Phys.* **2013**, *15* (32), 13446.

(51) Okunev, A. G.; Paukshtis, E. A.; Aristov, Y. I. Acetone Adsorption on Hydroxylated Silica Gel: Correlation of Sorption Isotherms and IR Spectra. *React. Kinet. Catal. Lett.* **1998**, *65* (1), 161–167.

(52) Crocellà, V.; Cerrato, G.; Magnacca, G.; Morterra, C. Adsorption of Acetone on Nonporous and Mesoporous Silica. *J. Phys. Chem. C* **2009**, *113* (37), 16517–16529.

(53) Ricchiardi, G.; Damin, A.; Bordiga, S.; Lamberti, C.; Spano, G.; Rivetti, F.; Zecchina, A.; Spanò, G.; Rivetti, F.; Zecchina, A. Vibrational Structure of Titanium Silicate Catalysts. A Spectroscopic and Theoretical Study. *J. Am. Chem. Soc.* **2001**, *123* (46), 11409–11419.

(54) Geobaldo, F.; Bordiga, S.; Zecchina, A.; Giamello, E.; Leofanti, G.; Petrini, G. DRS UV-Vis and EPR Spectroscopy of Hydroperoxo and Superoxo Complexes in Titanium Silicalite. *Catal. Letters* **1992**, *16* (1–2), 109–115.

(55) Bonino, F.; Damin, A.; Ricchiardi, G.; Ricci, M.; Spanò, G.; D'Aloisio, R.; Zecchina, A.; Lamberti, C.; Prestipino, C.; Bordiga, S. Ti-Peroxo Species

in the TS-1/H_2O_2/H_2O System. *J. Phys. Chem. B* **2004**, *108* (11), 3573–3583.

(56) Muscat, J.; Wander, A.; Harrison, N. M. On the Prediction of Band Gaps from Hybrid Functional Theory. *Chem. Phys. Lett.* **2001**, *342* (3–4), 397–401.

(57) Nannarone, S. The BEAR Beamline at Elettra. In *AIP Conference Proceedings*; AIP, 2004; Vol. 705, pp 450–453.

(58) Tauc, J. Optical Properties and Electronic Structure of Amorphous Ge and Si. *Mater. Res. Bull.* **1968**, *3* (1), 37–46.

(59) Zuo, Y.; Wang, X.; Guo, X. Synthesis of Titanium Silicalite-1 with Small Crystal Size by Using Mother Liquor of Titanium Silicalite-1 as Seeds (II): Influence of Synthesis Conditions on Properties of Titanium Silicalite-1. *Microporous Mesoporous Mater.* **2012**, *162*, 105–114.

(60) Guo, Q.; Feng, Z.; Li, G.; Fan, F.; Li, C. Finding The "missing Components" during the Synthesis of TS-1 Zeolite by UV Resonance Raman Spectroscopy. *J. Phys. Chem. C* **2013**, *117* (6), 2844–2848.

(61) Zuo, Y.; Liu, M.; Zhang, T.; Hong, L.; Guo, X.; Song, C.; Chen, Y.; Zhu, P.; Jaye, C.; Fischer, D. Role of Pentahedrally Coordinated Titanium in Titanium Silicalite-1 in Propene Epoxidation. *Rsc Adv.* **2015**, *5* (23), 17897–17904.

(62) Notari, B.; Perego, G.; Taramasso, M. Preparation of Porous Crystalline Synthetic Material Comprised of Silicon and Titanium Oxides. *US4410501 A*, **1983**.

(63) Kuznicki, S. M. Large-Pored Crystalline Titanium Molecular Sieve Zeolites. *US 4853202 A*, **1989**.

(64) Anderson, M. W.; Terasaki, O.; Ohsuna, T.; Philippou, A.; MacKay, S. P.; Ferreira, A.; Rocha, J.; Lidin, S. Structure of the Microporous Titanosilicate ETS-10. *Nature* **1994**, *367* (6461), 347–351.

(65) Borello, E.; Lamberti, C.; Bordiga, S.; Zecchina, A.; Areán, C. O.

Quantum-Size Effects in the Titanosilicate Molecular Sieve. *Appl. Phys. Lett.* **1997**, *71* (16), 2319.

Conclusions

The present thesis stressed the complexity of the Raman approach toward zeolites characterization, strongly based on the availability of dedicated setups allowing their analysis. The application field of Raman was in fact rather limited concerning zeolites, since the overlap of several problems. Among these, fluorescence, time resolution and sample damaging induced by the excitation sources (*i.e.* lasers) are the most insidious and complex to face: these are in fact strongly interconnected each others, and the solution of one of them often results in a detrimental effect on the others.

A key point of this thesis work was the development (followed by a rigorous testing activity) of dedicated measurements setups, able to "mediate" among the listed drawbacks. Even if the obtained solution is a kind of best compromise, it represents a considerable step forward in the Raman characterization of zeolites, indeed opening to their study in complex experimental conditions such as *in situ* and *operando*.

Because of the previous limitations, Raman and UV-Raman spectroscopies of zeolites are still open research field for a mature class of materials, as testified by the various examples presented along the chapters of this thesis. The results on acid zeolites demonstrated as Raman can still say something new, *e.g.* on the bare ZSM-5, a catalyst deeply characterized for over 40 years. Furthermore, the study on MTH reaction is of absolute relevance, since a "new eye" can represent a helpful tool in elucidating the complexity of this catalytic process. The same consideration stands for Ti zeolites: despite their simple structure and univocal features, their understanding decreases as much as these start to deviate from their perfection. Defectivity in TS-1 is an open topic where few experimental evidences accounts for a zoo of possible species: the additional clues from

Raman (possibly coupled with sophisticated experimental designs) are a step forward toward the comprehension of this intriguing topic. In this regard, the coupling of Raman and simulation techniques can be the trump card in order to give a final statement on structure and properties of the defective Ti sites. Because of the rigorous preparatory work on models and computational methods, simulation progresses are still a little behind the experimental ones: however a robust, ready-to-use set of tools has been developed, thus opening to the achievement of new insights in the near future.

This thesis work indeed cannot be considered as the "final word" on the Raman characterization of zeolites, but just it "pierced the veil of Maya" toward the enrichment of the knowledge on a fundamental branch of catalysis.